Active Control of Rotating Stall in a Transonic Compressor Stage with Inlet Distortion

by

Zoltán S. Spakovszky

S.M., Mechanical Engineering, Swiss Federal Institute of Technology, ETH Zürich (1997)

Submitted to the Department of Aeronautics and Astronautics
in partial fulfillment of the requirements for the degree of

MASTER OF SCIENCE IN AERONAUTICS AND ASTRONAUTICS

at the

MASSACHUSETTS INSTITUTE OF TECHNOLOGY

February 1999

Author_____
Department of Aeronautics and Astronautics
January 15, 1999

Certified by_____
Professor James D. Paduano
C.R. Sodberg Associate Professor of Aeronautics and Astronautics
Thesis Supervisor

Accepted by_____
Professor Jaime Peraire
Chairman, Department Graduate Committee

Active Control of Rotating Stall in a Transonic Compressor Stage with Inlet Distortion

by

Zoltán S. Spakovszky

Submitted to the Department of Aeronautics and Astronautics
on January 15, 1999, in partial fulfillment of the
requirements for the degree of
Master of Science in Aeronautics and Astronautics

Abstract

Rotating stall has been stabilized in a single-stage transonic axial flow compressor with inlet distortion using active feedback control. The experiments were conducted at the NASA Lewis Research Center on a single-stage transonic core compressor. An annular array of 12 jet-injectors located upstream of the rotor tip was used for forced response testing and to extend the compressor stable operating range. Results for radial and circumferential inlet distortion are reported.

First, the effects of radial distortion on the compressor performance and the dynamic behavior were investigated. Control laws were designed using empirical transfer function estimates determined from forced response results. The transfer functions indicated that the compressor dynamics are *decoupled* with radial inlet distortion, as they are for the case of undistorted inlet flow. Single-input-single-output (SISO) control strategies were therefore used for the radial distortion controller designs.

A circumferential total pressure distortion of about one dynamic head and a 120° extent (DC(60) = 0.61) introduced *coupling* between the harmonics of circumferential pressure perturbations, requiring multi-variable (MIMO) identification and control design techniques. A careful analysis of the coupled pre-stall compressor dynamics revealed a strong first spatial harmonic, dominated by the well known incompressible Moore-Greitzer mode. Constant gain control and more sophisticated MIMO robust control strategies were used for stabilization with circumferential inlet distortion.

Steady axisymmetric injection of 4% of the compressor mass flow resulted in a reduction in stalling mass flow of 9.7% relative to the case with radial inlet distortion and no injection. Use of a robust H_∞ controller with unsteady non-axisymmetric injection achieved a further reduction in stalling mass flow of 7.5%, resulting in a total reduction of 17.2%.

Steady injection experiments with circumferential inlet distortion resulted in a 6.2% reduction of stalling mass flow. Constant gain feedback, using unsteady asymmetric injection, yielded a further range extension of 9%. Testing of MIMO robust controllers showed only 2% reduction in stalling mass flow. Instead of further tuning the complex MIMO controllers, the same robust H_∞ controller used for radial distortion was tested. This controller achieved a reduction in stalling mass flow of 10.2% relative to steady injection, yielding a total reduction in stalling mass flow of 16.4%.

Thesis Supervisor: Professor James D. Paduano
Title: C.R. Sodberg Associate Professor of Aeronautics and Astronautics

poroszlói Graefl Katalin emlékére

Acknowledgments

This research would have never happened without the help and the contributions of many different people.

I would like to thank Professor Paduano for his guidance, encouragement and insightful suggestions throughout this work.

I am also greatly indebted to Michelle Bright, Ken Suder and Tony Strazisar at the NASA Lewis Research Center for their support and interest, and for giving me the opportunity to do this research. The help of the technical staff of the W8 test facility, Dave Williams, Randy Brokopp, and Barry Piendl is also greatly acknowledged.

I also wish to thank Professor Greitzer and Ivor Day for their insightful comments and the interesting discussions. I would like to thank Harald Weigl for the introduction to the NASA rig and the very helpful comments. I also wish to thank Chris van Schalkwyk for sharing data and system identification results and John Chi for the helpful inputs.

I am also indebted to all the people at GTL for making every day an interesting one. Namely, Amit, Adam, Chris, Jon, Luc and Rory for all the good times we had together. I also would like to thank all the people I met in Cleveland for making my stays at NASA always fun: Dave and the two Steve's for the unforgettable week-end riding dirt bikes, and Dale and Judy for their hospitality and the golf lessons.

Finally I wish to thank Liz, my family and all my friends for their personal support and for keeping the spirits always high. Without their belief in me I would have never made it.

This work was funded by NASA under grant NAG3-1457 whose support is gratefully acknowledged.

Contents

List of Figures

List of Tables

Nomenclature

Roman

a	spatial Fourier coefficient
A	area
$\mathbf{A}$	state space matrix, actuator dynamics
$\mathbf{B}$	state space matrix
$\mathbf{C}$	state space matrix
$\mathbf{D}$	state space matrix
c_x	axial chord
c	command input signal
$\mathbf{e}$	error signal
G	SISO transfer function
$\mathbf{G}$	MIMO transfer function matrix
H	transfer function
j	$\sqrt{-1}$
k	gain
$\mathbf{K}$	MIMO control law
$\dot{m}$	mass flow
M	Mach number
n	harmonic number
p	pressure
$\mathbf{P}$	plant
$\bar{r}$	mean radius
$\mathbf{r}$	reference input
R	gas constant
s	Laplace variable
t	time
T	temperature

$\mathbf{T}$	transfer function
u	input signal
v	velocity
$\mathbf{v}$	eigenvector
$\mathbf{V}$	matrix of eigenvectors
$\mathbf{w}$	unknown disturbance
$\mathbf{W}$	weighting function
x	axial coordinate
y	output signal
z	Z-transform variable
$\mathbf{z}$	error signal

Greek

β	compound flow indicator, phase angle
γ	ratio of specific heats, coherence
λ	sum of rotor inertias, eigenvalue
Λ	matrix of eigenvalues
μ	sum of all blade row inertias
ν	spatial Fourier coefficient
$\dot{\mu}$	ratio of mass flows
σ	real part of the eigenvalue (growth rate)
ω	imaginary part of the eigenvalue (rotation rate), frequency
Ω	rotor frequency
ϕ	non-dimensional axial velocity (flow coefficient)
$\delta\phi$	flow coefficient perturbation
Φ	power spectrum
Ψ	non-dimensional pressure rise across the entire compressor
π	pressure ratio
ρ	density
τ	non-dimensional time
θ	tangential coordinate
ξ	blade row stagger angle
ζ	area ratio

Subscripts

c	corner
$corr$	corrected
dc	DC
i	index
j	index
in	inlet values
ex	exit value
I	imaginary
R	real
stall	stall point
o	standard day
orf	orifice
t	total
working	working point
x	axial component
θ	tangential component

Superscripts

$\imath$	imaginary
r	real
inj	injected
ss	static-to-static
ts	total-to-static
tot	total
sp	spoiled
usp	unspoiled
$*$	complex conjugate, choked
$\sim$	spatial Fourier coefficient

Operators

Re	real part
Im	imaginary part

Acronyms

ADC	Analog to Digital Converter
DAC	Digital to Analog Converter
DC(60)	Distortion descriptor
DFT	Discrete Fourier Transform
ETFE	Empirical Transfer Function Estimate
FORSE	Frequency Observable Range Subspace Estimation
IDFT	Inverse Discrete Fourier Transform
LHS	Left Hand Side
MIMO	Multi-Input-Multi-Output
RHS	Right Hand Side
SERC	Space Engineering Research Center
SFC	Spatial Fourier Coefficient
SISO	Single-Input-Single-Output
SM	Stall-Margin

Chapter 1

Introduction

Gas turbine engine performance is limited by compressor flow instabilities known as surge and rotating stall. Surge is basically a circumferentially uniform pulsation of mass flow through the machine, while rotating stall appears as a reduced flow region in part of the circumference, which travels around the compressor annulus at a fraction of rotor speed. These instabilities have been extensively studied by the compressor aerodynamics community. In 1989 Epstein et al. [10] proposed a new approach to the problem: active stabilization of rotating stall and surge with feedback control. Since then, many experimental and theoretical investigations using different sensing and actuation schemes have been carried out, mainly in incompressible and undistorted flow regimes. For example Paduano [25] used movable inlet guide vanes in a low-speed single and multi stage compressor with undistorted inlet flow and was first to demonstrate active control of rotating stall. Van Schalkwyk [30] also used variable guide vanes, in the MIT three stage low-speed compressor, and stabilized the compressor with severe circumferential inlet distortion.

More complex situations in transonic turbomachinery have also been investigated. The very first effort using steady blowing and bleeding devices to determine if tip boundary layer control was an effective means of increasing the unstalled mass flow range of a transonic single-stage compressor with and without inlet flow distortion was conducted by Koch [18]. Prior to the study described in this research, active stabilization of rotating stall in axial flow compressors was demonstrated, primarily under undistorted inlet flow conditions. The use of an annular array of injectors to extend the stable operating range of the same transonic compressor stage under undistorted inlet flow conditions was reported by Weigl [32] (also see [33]). Each injector was coupled to a high speed valve. The development and testing of the valve-injector system was described by Berndt [1]. The present work extends the use of steady and controlled injection for transonic compressor stability enhancement to cases which feature distorted inlet flows.

1.1 Stall Inception and Compressor Flow Modeling

For a better understanding of the coupled compressor dynamics a short overview of *undistorted* flow compressor modeling is given. The classic Moore-Greitzer formulation ([23], [24] and [21]) considers an incompressible two-dimensional flow field with an axisymmetric, spatially uniform (undistorted) inlet flow, and a linearized approach for the perturbations. The rotating stall dynamics for the nth mode are described by

$$\left(\frac{2}{|n|}+\mu\right)\frac{\partial\delta\phi}{\partial\tau}=\left(\frac{\partial\Psi^{\mathrm{ts}}}{\partial\phi}-jn\lambda\right)\delta\phi, \tag{1.1}$$

where Ψ^{ts} is the total-to-static pressure rise coefficient of the entire compressor and ϕ and $\delta\phi$ are the compressor face flow coefficient and its perturbation respectively. The inertia parameters are the fluidic inertia in the rotors λ, in the rotors plus stators μ, and in the inlet and exit ducts $\frac{2}{|n|}$, where

$$\lambda=\sum_{\text{rotors}}\frac{c_x/\bar{r}}{\cos^2\xi}\qquad\text{and}\qquad\mu=\lambda+\sum_{\text{stators}}\frac{c_x/\bar{r}}{\cos^2\xi}. \tag{1.2}$$

c_x, $\bar{r}$, and ξ are the axial chord, mean radius, and stagger angle respectively. Solving Equation (1.1) with a spatial Fourier decomposition for the flow coefficient perturbations

$$\delta\phi(\theta,t)=\sum_{n=-\infty}^{\infty}\delta\widetilde{\phi}_n(t)e^{jn\theta} \tag{1.3}$$

yields

$$\delta\phi(\theta,t)=\sum_{n=-\infty}^{\infty}a_n e^{(\sigma_n-jn\omega_n)t}e^{jn\theta}, \tag{1.4}$$

where θ and t are the angle around the annulus and the time respectively. The growth rate σ_n and rotation rate ω_n are given by substituting Equation (1.4) into Equation (1.1):

$$\sigma_n=\frac{\frac{\partial\Psi^{\mathrm{ts}}}{\partial\phi}}{\left(\frac{2}{|n|}+\mu\right)}\qquad\text{and}\qquad\omega_n=\frac{\lambda}{\left(\frac{2}{|n|}+\mu\right)}. \tag{1.5}$$

This solution describes spatial waves of sinusoidal shape (harmonics) that travel around the annulus at rotation rate ω_n, and grow or decay in time with growth rate σ_n. Compressor stability is determined by the growth rate of these modes. In this model, the axial velocity perturbations $\delta\phi(\theta)$ are axially uniform throughout the compressor. Furthermore, the flow field for the nth mode consists only of the nth spatial harmonic. That is, the harmonics are all *decoupled* (independent of one another).

In the presence of circumferentially nonuniform inlet flow the pressure rise Ψ^{ts}, and therefore the slope $\frac{\partial \Psi^{ts}}{\partial \phi}$, is no longer a constant but a strong function of θ. This nonlinear coupling between the steady inlet flow field and the compressor map strongly influences the linearized behavior of the flow field perturbations. The mode shapes are no longer purely sinusoidal but have contributions of other harmonics. In other words, distortion introduces *coupling* between the harmonics. Hynes and Greitzer [16] have extended the Moore-Greitzer model to describe incompressible dynamics with inlet distortion. The accuracy of this model has been verified experimentally by van Schalkwyk [31] on a low-speed three-stage compressor. Generally, for distorted inlet flow, the major change in the compressor pre-stall behavior is that the distortion introduces non-linearities which couple the compressor dynamics. However, when the distortion is circumferentially uniform (e.g. radial distortion) the harmonics can still be decoupled.

1.2 Research Questions

If the compressor flow field is compressible, as is the case for the NASA Stage 35 compressor, acoustic modes with axial structure are introduced. In this case, each compression system mode has both circumferential and axial structure. Modeling of this kind was conducted by Bonnaure [4], Hendricks [15], and Feulner [11]. To date, no control-theoretic compressible model exists which accounts for inlet distortion. Thus it is one of the goals of this research to investigate the effects of inlet distortion on high-speed compressor pre-stall behavior.

The other goals of this research are identification and stabilization of the NASA Lewis compression system with inlet distortion. The framework for pursuing the goals will be a multi-variable input-output characterization where measurements and actuation are expressed as complex spatial Fourier coefficients ([26]). This framework is consistent with the stability analysis of Hynes and Greitzer [16], except that analysis was homogeneous instead of forced, and the nonlinear steady-state condition was found numerically (here it is achieved experimentally). Coupling between harmonics due to circumferential distortion is indicated by nonzero off-diagonal elements of the compressor transfer function matrix. The consequence of this coupling is that the individual transfer functions of the compressor dynamics cannot be treated independently; thus controller design becomes a multi-input-multi-output (MIMO) problem. This increases the complexity of the controller and complicates system identification. One of the major issues of this research is this coupling effect in the case of compressible compressor dynamics. This issue is addressed in this work.

Another research question is associated with the stall control mechanism. Stall inception and control studies done by Camp and Day [7] and Day [9] indicate that instability of a long length scale eigenmode (also called modal wave) is not the cause of rotating stall in some low- and high-speed compressors; in some cases short length scale rotating disturbances called spikes can be the

source of instability. Depending on the stall inception pattern exhibited by the compressor, different control strategies were applied. The introduction of distortion to the compressor described in this research shows the interplay of spikes and long length scale stall precursors. The effects of steady and controlled air injection on the compressor pre-stall behavior is also discussed in this work.

Chapter 2

Experimental Setup

2.1 Test Compressor

All experiments described in this research were conducted at the NASA Lewis Research Center in the Single-Stage Axial Compressor Test Facility. The NASA Stage 35 test compressor, originally designed as an inlet stage of an eight-stage 20:1 pressure ratio core compressor ([27]), has a total pressure ratio of 1.82, a mass flow of 20.2 kg/s, a rotor tip speed of 455 m/s, and a rotation frequency of 286 Hz at design conditions. Rotor 35 consists of 36 blades with an aspect ratio of 1.19, a hub-to-tip radius ratio of 0.7, and a blade tip diameter of approximately 50 cm. The mean-line rotor chord length is 56 mm. Stator 35 has 46 blades with an aspect ratio of 1.26 and a chord length of 40 mm. Detailed performance descriptions are given by [28].

Atmospheric air is drawn into the test facility through an orifice plate and a plenum chamber upstream of the test section. Downstream of the compressor the flow is regulated with a sleeve-type throttle valve. The compressor is driven by a 2.2 MW DC drive motor. The compressor mass flow is controlled by adjusting the exit area of the throttle valve. After passing through the throttle valve, the air is exhausted to the atmosphere. All experiments were conducted at 85% corrected design speed because shaft whirl occurred at speeds above 85%, introducing a source of forcing not related to the aerodynamics of the compressor.

2.2 Steady and Unsteady Sensors

Both steady and unsteady measurements were made during the course of this research. To measure the steady state compressor performance and distortion magnitude, steady static pressure taps at various hub and casing locations were used, as well as steady total pressure and total temperature survey probes located up- and downstream of the compressor. The different locations are shown in

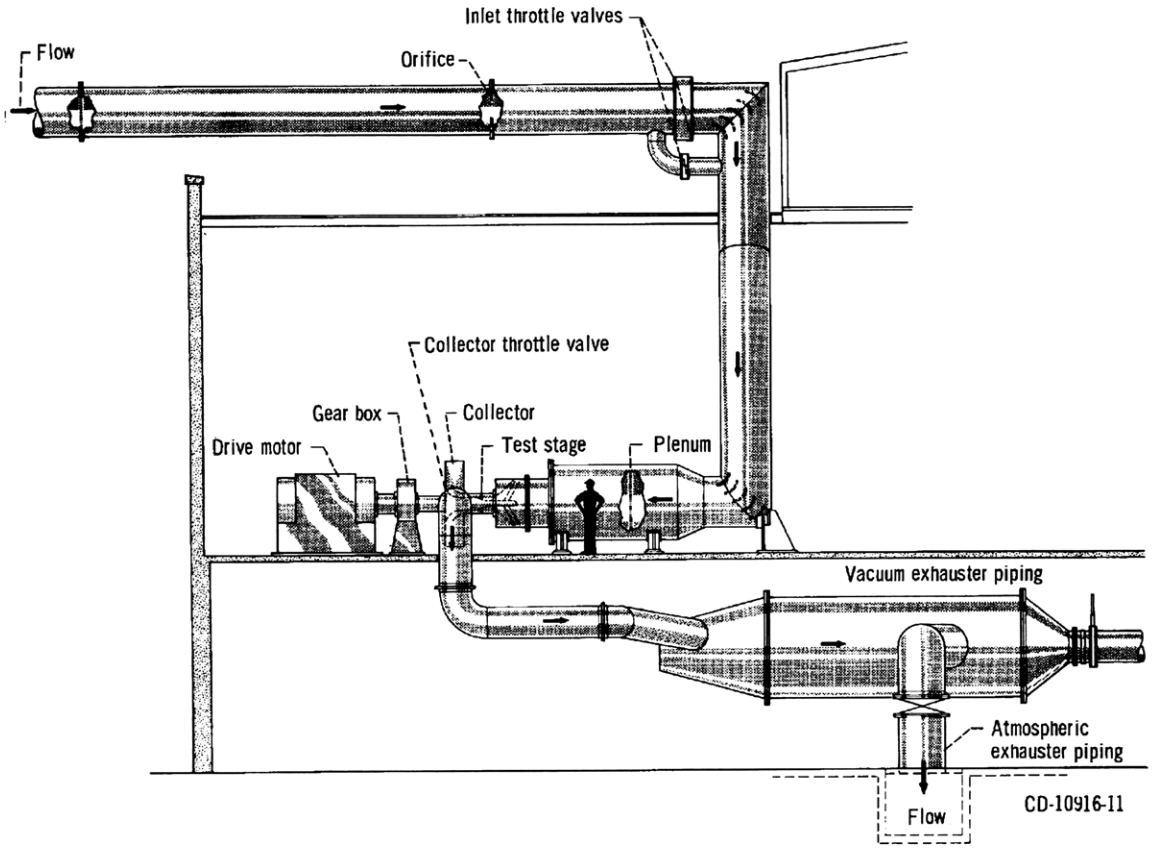

Figure 2-1: NASA high-speed axial compressor test facility (from [27]).

Figure 2-2 and the steady sensor information is given in Table 2.1. The amount of air flowing through the upstream plenum and inlet duct of the compressor is measured at the orifice (see Figure 2-1). The upstream plenum pressure and temperature, which are the total pressure and temperature of the test section inlet, are also recorded.

High bandwidth wall static pressure sensors at various axial stations measured the unsteady pressure perturbations. Five PSI differential pressure transducers, Kulite Semiconductor Products, are used as unsteady sensors. The sensors are mounted flush with the inner contour of the compressor casing and have a natural frequency of 100 kHz, which is well above the sampling frequency of 3 kHz and the actuator bandwidth of 400 Hz. The unsteady static pressure sensor configuration is summarized in Table 2.2.

2.3 Air Injection Actuation

High momentum air injection is used as actuation for system identification and control. The jet actuators were designed by Berndt [1] and developed by Moog Inc. and MIT. They consist of three main components as depicted in Figure 2-2: a linear displacement servo motor moves a sleeve type

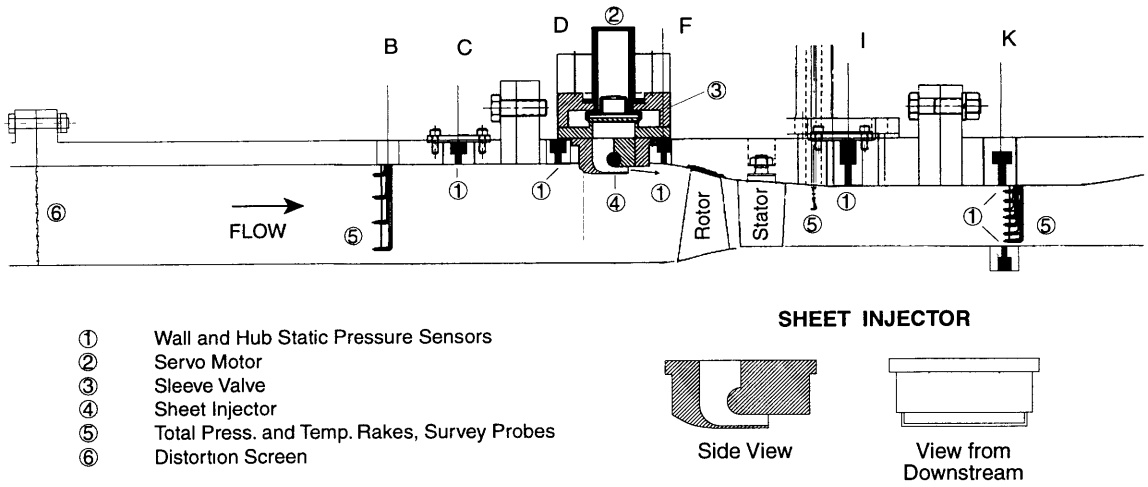

Figure 2-2: NASA Stage 35 actuation and instrumentation schematic with inlet distortion.

valve to modulate the mass flow through the actuator. The injector directs the flow from the valve toward the rotor.

Axial Station	No. of Sensors	Sensor Type	Axial Loc. [m]	Circumferential Angle [deg]
B	1	5-Element Total Press. Rake	-0.225	315
	1	5-Element Total Temp. Rake	-0.225	315
	4	Wall Static Press. Tap	-0.225	45, 135, 225, 315
K	2	7-Element Total Press. Rake	0.259	135, 315
	2	7-Element Total Temp. Rake	0.259	135, 315
	4	Wall Static Press. Tap	0.259	60, 150, 240, 330
	4	Hub Static Press. Tap	0.259	60, 150, 240, 330

Table 2.1: NASA Stage 35 steady flow field sensors.

The 12 circumferentially equally spaced jet actuators are placed 63 mm (1.1 rotor chord lengths) upstream of the rotor face mounted on the outer casing. The actuators are capable of delivering 5.8% of the design compressor mass flow when supplied with 100 PSI air and have a bandwidth of 400 Hz. Since rotor 35 is tip critical and an extensive study of two different types of injectors (a 3-hole injector and a sheet injector shown in Figure 2-2) conducted by Weigl [32] showed that the maximal reduction in stalling mass flow was obtained by the sheet injector, all experiments were done with this kind of injector. The sheet injectors affect the outer 7% of the rotor inlet span. A detailed description and the actuator design requirements are given in [2].

The sheet injectors were mounted at a yaw angle of -15^o (yawed 15^o from the axial direction so as to inject flow against the direction of rotor rotation) which was found by Weigl (for details see [33]) to give the best reduction in stalling mass flow and the highest pressure rise with 50% steady state blowing and no inlet distortion. Throughout this thesis, "50% blowing" refers to a 100 PSI supply pressure with a 50% valve opening. This corresponds to an injector exit total pressure of

Axial Station	No. of Sensors	Sensor Type	Axial Loc. [m]	Circumferential Angle [deg]
C	8	Wall Static Press. Kulite	-0.187	22.5, 67.5, 112.5, ... 292.5, 337.5
D	12	Wall Static Press. Kulite	-0.090	15, 45, 75 , ... 315, 345
F	8	Wall Static Press. Kulite	-0.022	15, 75, 105, 165 195, 255, 285, 345
K	8	Wall Static Press. Kulite	0.259	22.5, 67.5, 112.5, ... 292.5, 337.5

Table 2.2: NASA Stage 35 unsteady flow field sensors

16.7 PSI and an exit total temperature of 30.9^{o}C yielding a total corrected injector mass flow of 0.652 kg/s for 12 actuators.

2.4 Data Acquisition System

The following data acquisition system was used for this research. A more detailed description of the control computer setup is given in [33].

2.4.1 Hardware

The control computer used for the experiments is a 90 MHz Pentium PC with 64 inputs and 16 analogue output channels. The sample rate used for all experiments is 3 kHz. Data is acquired in a circular buffer of up to 45 seconds in length (limited only by available RAM). The inputs to the control computer are the high-response pressure transducer measurements (Kulite sensors), position sensor signals from the actuator motors, and steady state compressor performance measurements (static pressures at various hub and casing locations, mass flow, pressure rise, and throttle position). Unsteady pressure measurements immediately upstream of the rotor (axial station F in Figure 2-2) had the highest signal-to-noise ratio and were therefore used for system identification and control law testing. The outputs of the control computer are 12 independently commanded mass flow injection rates.

2.4.2 Software

The data acquisition and control program, coded in C/C++ by Weigl [33] and setup for single-input-single-output (SISO) control strategies, was extended to the multi-input-multi-output (MIMO) case with inlet distortion. A modular design separated the various functions for sensor calibration, transient stall measurements, system identification and feedback control. The system is capable implementing spatial Fourier calculations and linear control laws with up to 60 states at a sampling

rate of 3 kHz.

2.5 Inlet Distortion

To conduct experiments with compressor inlet distortion two different distortion screens were designed: a radial inlet distortion screen and a circumferential inlet distortion screen. Both distortion screens can be mounted on a carrier which is located at approximately 2.2 mean radii upstream of the rotor (see also Figure 2-2).

2.5.1 Radial Distortion Screen

A radial distortion screen, which consisted of a fine mesh, covered about 38% of the blade span in the tip region. Measurements show that the inlet flow with radial distortion is still circumferentially uniform but has a total pressure loss in the tip region. The measurement of the radial inlet distortion profile is depicted in Figure 2-3. Plotted are the radial distributions (measured about 1.1 mean radii

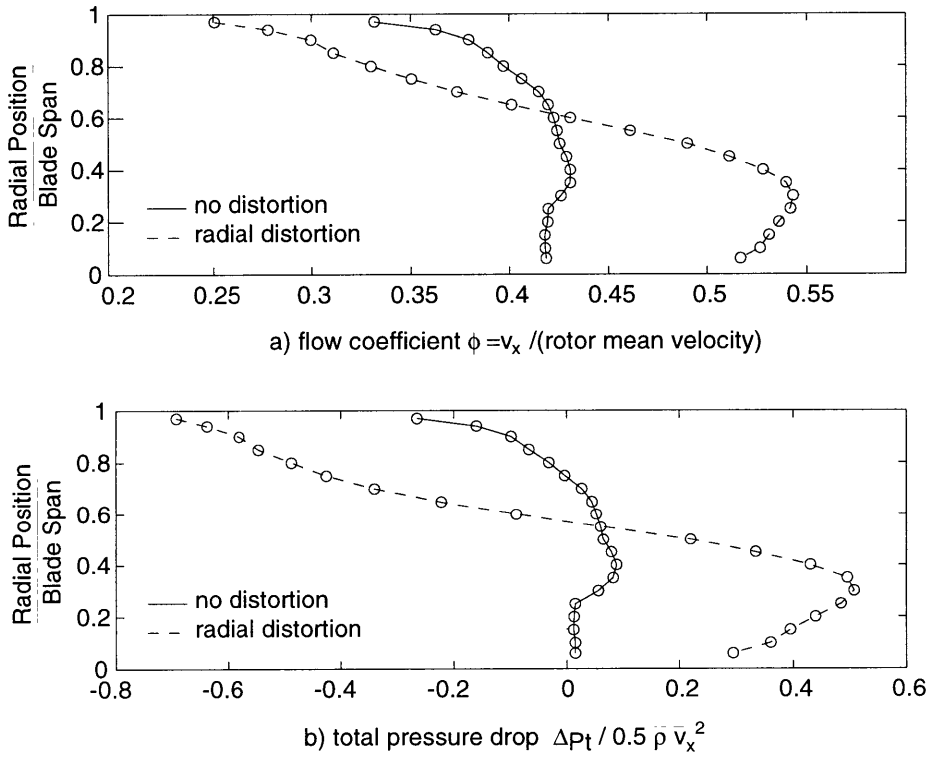

Figure 2-3: Measured radial distortion profile.

downstream of the distortion screen, axial station B) of the flow coefficient $\phi = v_x/(\text{mean wheel speed})$, and the total pressure drop $\Delta p_t = p_t - \bar{p}_t$ normalized by the mean dynamic head for the case with undistorted inlet flow and the case with radial distortion. $\bar{p}_t$ is the radial average of the

measured total pressure p_t. The undistorted inlet flow case refers to measurements with the coarse-mesh carrier screen in the flow path which interacts with the casing boundary layer and explains the considerable drop in flow coefficient and total pressure in the casing region.

2.5.2 Circumferential Distortion Screen

Circumferential inlet airflow distortion, typically caused by phenomena such as flow separation or non-axisymmetric intake duct geometry, was studied by installing a circumferential distortion screen. The screen is again mounted on the carrier and can be indexed through 350° around the annulus to allow more detailed mapping of steady state compressor performance. The extent of the screen was 120° and covered the full blade span. During steady-state mapping, identification and control tests, the distortion screen blocked the flow between 120° and 240° circumferentially. Circumferential total and static pressure and total temperature profiles were measured with probes positioned between the distortion screen and the rotor. The steady pressure and temperature probes were geometrically fixed and the screen was rotated in five degree increments to obtain the profiles. The total pressure drop generated by the distortion screen was about one dynamic head, that is

$$\frac{\Delta p_t}{\frac{1}{2}\bar{\rho}\bar{v}_x^2} \approx 1. \tag{2.1}$$

The measured total pressure drop distribution upstream of the compressor is plotted in Figure 2-4. The blocked flow region is marked with the dotted vertical lines.

The distortion magnitude can also be described by a parameter commonly used in engine intake aerodynamics called the DC(60) descriptor ([34]). The DC(60) descriptor is defined by

$$\mathrm{DC}(60) = \frac{\bar{p}_\mathrm{t}|_{360°} - \bar{p}_\mathrm{t}|_{\text{worst } 60°}}{\frac{1}{2}\rho\bar{v}_x^2}. \tag{2.2}$$

In the ideal case where the static pressure is uniform, DC(60)=1 corresponds to zero-velocity flow within the 60° sector, giving very poor inlet aerodynamics. The distortion screen designed for Stage 35 with 1 dynamic head distortion magnitude corresponds to DC(60)=0.61, representing poor inlet conditions, as shown in the velocity profile in Figure 2-5.

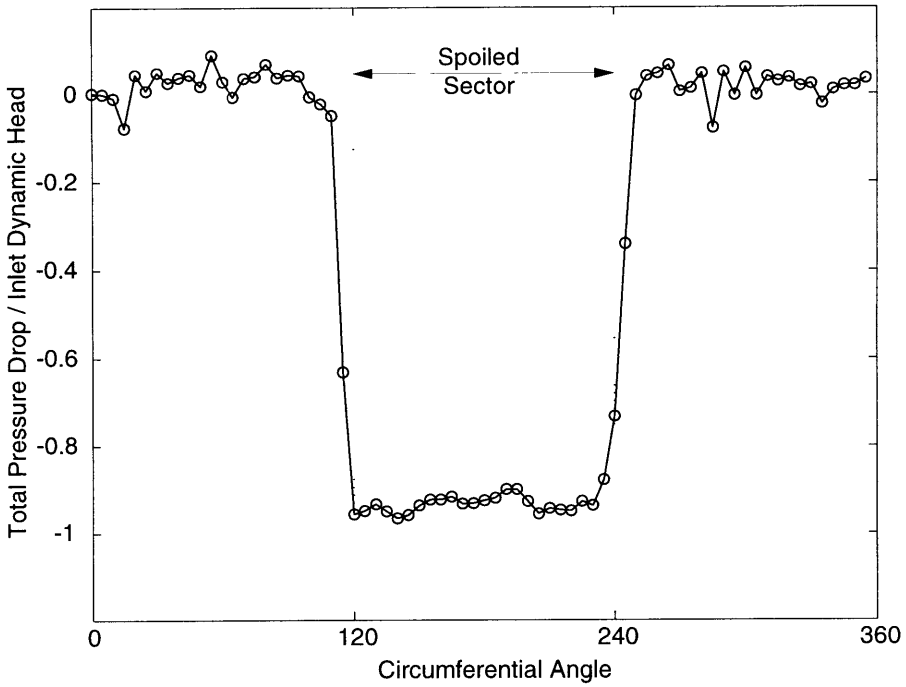

Figure 2-4: Measured 1 dynamic head distortion at $\dot{m}_{corr}^{tot} = 16.5$ kg/s.

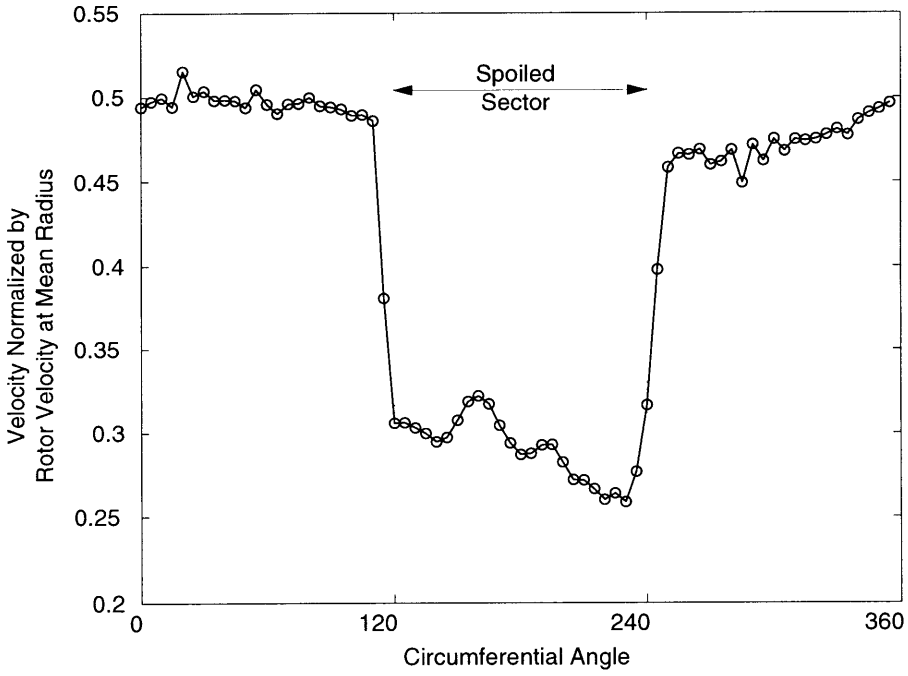

Figure 2-5: Measured velocity profile for 1 dynamic head distortion at $\dot{m}_{corr}^{tot} = 16.5$ kg/s.

Chapter 3

Steady-State Experiments

In this chapter the steady state compressor performance with and without inlet distortion is discussed. The effect of steady axisymmetric air injection on compressor pressure rise and stalling mass flow with inlet distortion is also described. All speed lines are constructed from the measured total inlet pressure upstream of the actuators, the exit static pressure (average of hub and casing wall static pressures downstream of the stage), and the total corrected mass flow through the compressor. The total corrected mass flow is the sum of the inlet flow rate (measured by an orifice far upstream of the compressor and corrected by the total pressure and temperature at the same location) and the injector flow rate (determined by a separate venturi meter and corrected by the total pressure and temperature in the injector). In the case of inlet distortion the compressor flow field is nonuniform and the inlet mass flow must be corrected differently. The detailed correction procedure is given in Appendix A.

3.1 Radial Inlet Distortion

First, the nominal speed line at 85% corrected design speed (no distortion and no blowing) was measured. The radial distortion screen was then mounted on the carrier and the speed line was measured without injection. The measurements of the nominal total-to-static speed line (solid) and the total-to-static speed line with radial distortion and no blowing (dashed) are shown in Figure 3-1. The slopes of the total-to-static pressure ratios are crucial for the determination of compressor stability [1]. The peak pressure ratio drops and the compressor stalls at higher mass flows when radial distortion is introduced to the compressor. In the next experiment the compressor speed line at 85% corrected design speed is measured with 50% steady state blowing. Steady blowing at a valve opening of 50% is of interest because actively controlled blowing is commanded about a mean

[1] For high-speed machines the slope of the total-to-static pressure ratio is analogous to the total-to-static pressure rise coefficient which is a relevant parameter for rotating stall in low-speed compressors (see [33] page 55 for details).

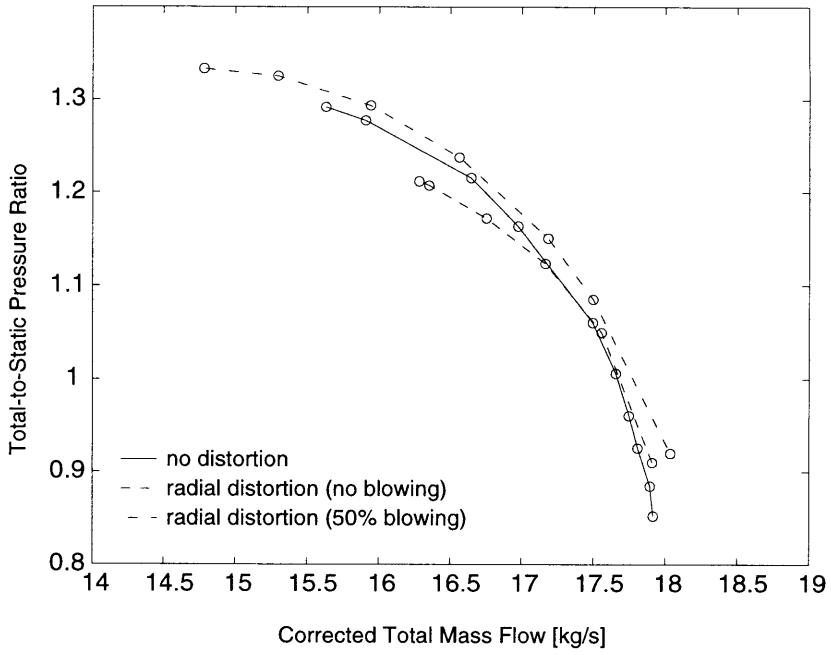

Figure 3-1: Speed lines for no distortion and radial inlet distortion.

valve position of 50% open. Steady blowing at 50% open is therefore taken as the baseline condition from which the impact of active blowing is assessed. The measured total-to-static speed line with radial distortion and 50% steady state blowing is also plotted in Figure 3-1 (dash-dotted curve). The experiment shows that steady state injection can recover the lost performance due to radial inlet distortion and even produces a significant reduction in stalling mass flow of 9.7% relative to the case with inlet distortion and no injection.

3.2 Circumferential Inlet Distortion

The radial inlet distortion screen was then replaced by the circumferential inlet distortion screen. Again the effect of distortion on the compressor pressure ratio was measured. The speed lines are constructed as mentioned earlier: total corrected mass flow is the sum of an upstream orifice mass flow and the injected mass flow (for details see Appendix A), the upstream total pressure is the mass average of total pressure probes between the distortion screen and the actuators, and the downstream pressure is from mass averaged hub and casing static pressure measurements. Figure 3-2 depicts the nominal (no distortion and no blowing) total-to-static speed line at 85% corrected design speed (solid) and the speed line with circumferential inlet distortion and no blowing (dashed).

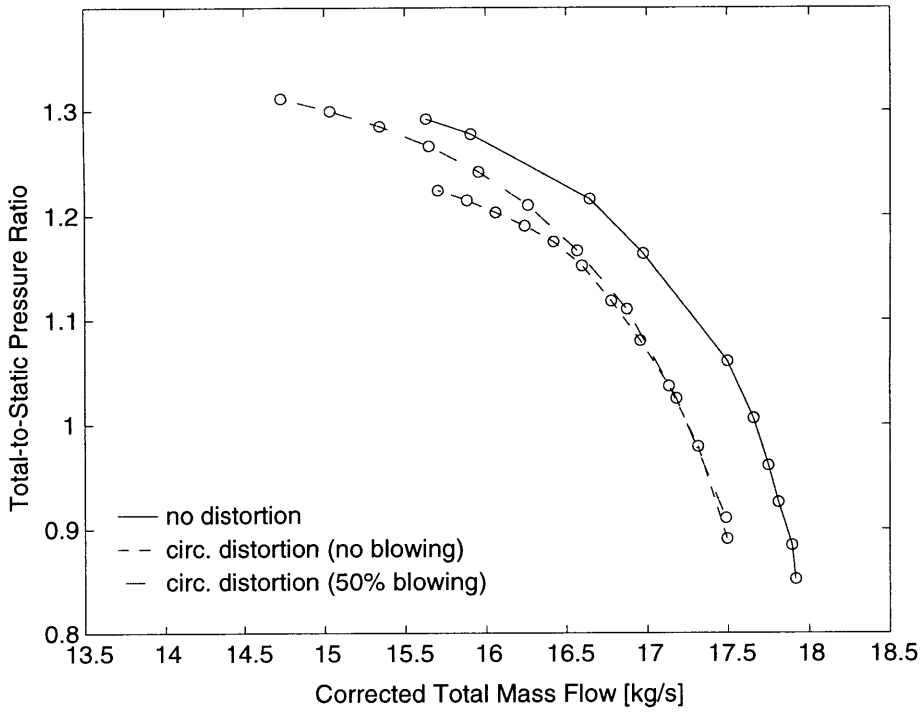

Figure 3-2: Speed lines for undistorted inlet (solid), circumferential distortion no blowing (dash), and with 50% steady blowing (dash-dot).

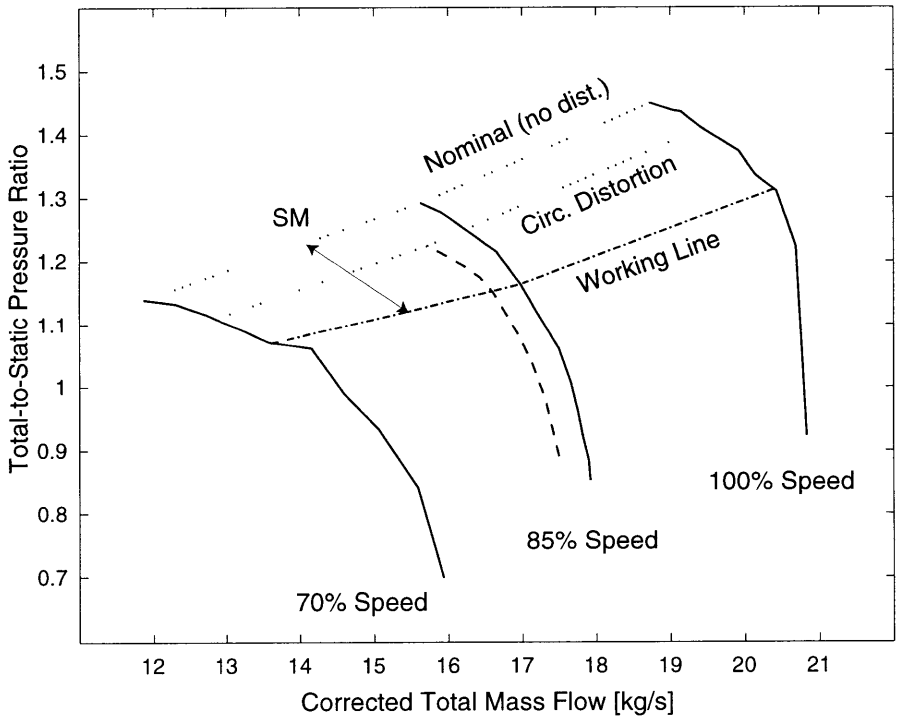

Figure 3-3: Reduction of stall-margin due to circumferential inlet distortion.

One can see that the circumferential distortion resulted in a peak pressure ratio drop but the compressor stalls at about the same corrected mass flow. Also note that the compressor chokes at a higher mass flow with no distortion than with circumferential inlet distortion. However, examination of the entire compressor map reveals that the stall line is shifted to higher corrected mass flows with circumferential inlet distortion. Thus the stall-margin (defined in Equation (3.1)) is significantly reduced with inlet distortion as shown in Figure 3-3.

The effect of steady blowing (steady valve opening of 50%, injected corrected mass flow of 0.65 kg/sec) on the pressure ratio was measured next. With steady blowing the peak pressure ratio can be recovered and even a considerable range extension of 6.2% in stalling mass flow can be obtained. Although the pressure ratio of the compressor is recovered by blowing, there is no change in the inlet distortion, because the distortion screen is upstream of the compressor, and there is strong evidence for considerable non-uniformity in the compressor face flow field, as we will see in the system identification results discussed in Section 5.4.

3.3 Summary of Steady-State Experimental Results

The steady-state experimental results with inlet distortion, both radial and circumferential, are summarized in Table 3.1. Steady-state injection has a strong effect on the pressure ratio of the compressor and yields comparable reductions in stalling mass flow for the two inlet distortion types. The stall-margin is also computed and included in Table 3.1 using the stall-margin definition by Cumpsty [8]

$$\mathrm{SM} = 1 - \frac{\pi_{\mathrm{working}}}{\pi_{\mathrm{stall}}} \cdot \frac{\dot{m}_{\mathrm{stall}}}{\dot{m}_{\mathrm{working}}} \,. \tag{3.1}$$

To be consistent with Figure 3-3 the total-to-static pressure ratio is used for π. The working pressure ratio π_{working} and working mass flow $\dot{m}_{\mathrm{working}}$ are 1.16 and 17 kg/s for no distortion and radial inlet distortion; the working operating point values for circumferential inlet distortion are 1.15 and 16.6 kg/s. Although the choice of the compressor working line (as depicted in Figure 3-3) is somewhat arbitrary, the goal is not to quantify the absolute value of the stall-margin; the focus is to demonstrate the changes in stall-margin due to the effects of inlet distortion, steady and controlled injection.

Configuration	$\dot{m}_{stall}$ [kg/s]	% Decrease $\dot{m}_{stall}$	Stall-margin [%]
Undistorted Inlet Flow			
No Blowing	15.6	—	17.2
Radial Inlet Distortion			
No Blowing	16.3	—	8.1
50% Blowing	14.7	9.7	24.1
Circumferential Inlet Distortion			
No Blowing	15.7	—	10.9
50% Blowing	14.7	6.2	22.2

Table 3.1: Steady-state experimental results with inlet distortion

3.4 Compressor Flow Behavior with Inlet Distortion

The measured flow field and compressor performance with circumferential inlet distortion reveals two interesting results. These are discussed next.

3.4.1 Compressor Choke - Compound Compressible Flow Analysis

As shown in Figure 3-2 the choke side of the total-to-static speed lines with undistorted inlet flow and circumferential inlet distortion do not align. The nonuniform flow field induced by the strong circumferential inlet distortion seems to alter the choking behavior of the compressor. To analyze this behavior a compound compressible flow analysis is conducted ([13],[3]).

Consider the compressor gas path as a variable area duct with a choking device (a nozzle). The flow through the duct is divided into a finite number of stream tubes N. The stream tubes can have different areas $A_i(x)$ and Mach numbers $M_i(x)$. The fluid static pressure $p(x)$ is regarded as an independent variable because it only varies *along* the duct while other properties (total pressure, Mach number etc.) change *across* the duct (from stream tube to stream tube). Using 1-dimensional theory for a single flow, continuity can be written in logarithmic differential form as

$$\frac{d\rho}{\rho} + \frac{dv}{v} + \frac{dA}{A} = 0\,. \tag{3.2}$$

The momentum equation yields in differential form

$$v^2 \frac{dv}{v} = -\frac{dp}{\rho} \,. \tag{3.3}$$

Assuming isentropic flow

$$\frac{1}{\gamma}\frac{dp}{p} = \frac{d\rho}{\rho} \,, \tag{3.4}$$

Equation (3.2) and Equation (3.3) can be combined to yield

$$\frac{dA}{A} = -\frac{1}{\gamma}\frac{dp}{p}\left(1 - \frac{1}{M^2}\right) \,. \tag{3.5}$$

This idea can be used now for each stream. Noticing that $\sum \frac{dA_i}{dx} = \frac{dA}{dx}$ and defining the *compound flow indicator* β as

$$\beta = \sum_{i=1}^{N} \frac{A_i}{\gamma_i}\left(\frac{1}{M_i^2} - 1\right) \,, \tag{3.6}$$

we can write

$$\frac{d}{dx}\log p = \frac{1}{\beta}\frac{dA}{dx} \,. \tag{3.7}$$

In principle Equation (3.7) can be integrated to find $p(x)$ along the duct since the compound flow indicator β is only a function of static pressure: for any given value of p at the inlet plane where A_i is known, $\dot{m}_i$ is determined by conservation of mass

$$\dot{m}_i = \frac{A_i\, p_{ti}}{\sqrt{T_{ti}}}\left(\frac{p_{ti}}{p}\right)^{-1/\gamma_i}\left\{\frac{2\,\gamma_i}{R_i\,(\gamma_i - 1)}\left[1 - \left(\frac{p_{ti}}{p}\right)^{\frac{1-\gamma_i}{\gamma_i}}\right]\right\}^{1/2} \,. \tag{3.8}$$

Thus the local $A_i(x)$ anywhere else are functions only of local $p(x)$ and known quantities. The local Mach number $M_i(x)$ can also be expressed in terms of the local pressure $p(x)$ and the total pressure in the stream p_{ti}

$$M_i(x)^2 = \frac{2}{\gamma_i - 1}\left[\left(\frac{p_{ti}}{p(x)}\right)^{\frac{\gamma_i - 1}{\gamma_i}} - 1\right] \,. \tag{3.9}$$

Therefore the local value of β is only a function of local pressure $p(x)$, known quantities and inlet total pressure p_{ti}.

Examination of inlet and back pressure effects on the flow in a convergent-divergent duct shows that if the inlet static pressure p is high enough, then the values of M_i will be small enough to

yield $\beta > 0$ everywhere. Thus changes in p are of the same sign as changes in A, both with a minimum at the throat, and the flow is *compound subsonic*. Now if the inlet static pressure is low enough, β reaches zero at the throat and Equation (3.7) is indeterminate ($\frac{dA}{dx} = 0$ at the throat). A careful analysis shows that if the back pressure is low enough, β switches sign as passing through the throat: the flow is *compound subsonic* ($\beta > 0$) in the convergent region, *compound sonic* ($\beta = 0$) at the throat and *compound supersonic* ($\beta < 0$) in the divergent region. Thus if the back pressure is smaller than that critical value, the inlet pressure and flow rate are not affected. This is *compound choking* resulting in a *compound shock wave* for very low back pressures. In summary the following conclusions can be made for a compound compressible flow:

- Flow choking does not occur at a Mach number of 1.
- The Mach number of an individual stream is not necessarily 1 at the throat.
- Compound choking is determined by the compound flow indicator β, that is if $\beta = 0$.
- Not every stream will have $M_i > 1$.
- Compound flow regimes are analogous to subsonic and supersonic flow regimes in single stream flow, i.e. one obtains the single stream results by setting $N = 1$.

The derived equations will now be used to analyze the two-stream compound compressible flow with circumferential inlet distortion. The choking device is somewhere in the compressor gas path since the throttle downstream of the compressor stage is unchoked over the entire compressor mass flow range. The flow through the compressor is divided into two streams: 2/3 of the total flow area has the total pressure $p_{t1} = p_t$, whereas the total pressure in the other 1/3 of the total flow area is reduced by one dynamic head due to the circumferential distortion screen ($p_{t2} = p_t - \Delta p_t$). Using the choking condition for compound compressible flow ($\beta = 0$) and assuming identical γ for the two streams, the necessary pressure ratio $(p_t/p)^*$ for compound choking can be found in function of the total pressure drop $\Delta p_t/p^*$ by solving

$$\frac{2/3}{\left(\frac{2}{\gamma-1}\right)\left[\left(\frac{p_t}{p}\right)^{*\,\frac{\gamma-1}{\gamma}} - 1\right]} + \frac{1/3}{\left(\frac{2}{\gamma-1}\right)\left[\left(\left(\frac{p_t}{p}\right)^{*} - \frac{\Delta p_t}{p^*}\right)^{\frac{\gamma-1}{\gamma}} - 1\right]} = 1\,. \tag{3.10}$$

The numerical solution of Equation (3.10) is plotted in Figure 3-4. Note that if the total pressure drop $\Delta p_t = 0$ (undistorted flow), the choking pressure ratio is 1.89 which can also be obtained from $(p_t/p)^* = (\frac{\gamma+1}{2})^{\gamma/\gamma-1}$. Using Equation (3.8) and the choking pressure ratio for each stream, the

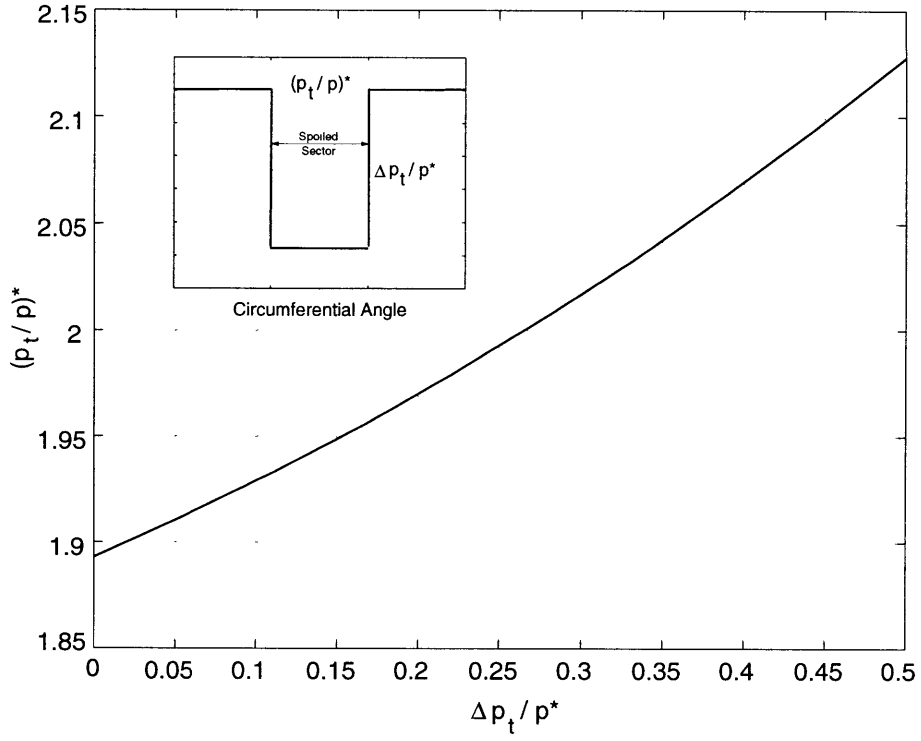

Figure 3-4: Choking pressure ratio $(p_t/p)^*$ for circumferential inlet distortion $(\Delta p_t/p^*)$.

total corrected choking mass flow can be computed as

$$\left(\frac{\dot{m}\sqrt{T_t}}{A\,p_t}\right)^* = \frac{2}{3}\left(\frac{p_t^*}{p^*}\right)^{\frac{-1}{\gamma}}\left\{\frac{2\,\gamma}{R\,(\gamma-1)}\left[1-\left(\frac{p_t^*}{p^*}\right)^{\frac{1-\gamma}{\gamma}}\right]\right\}^{1/2}$$
$$+\frac{1}{3}\left(1-\frac{\Delta p_t}{p_t^*}\right)\left[\left(\frac{p_t}{p}\right)^* - \frac{\Delta p_t}{p^*}\right]^{\frac{-1}{\gamma}}\left\{\frac{2\,\gamma}{R\,(\gamma-1)}\left[1-\left[\left(\frac{p_t}{p}\right)^* - \frac{\Delta p_t}{p^*}\right]^{\frac{1-\gamma}{\gamma}}\right]\right\}^{1/2} . \quad (3.11)$$

In other words, the choking corrected mass flow with circumferential inlet distortion normalized by the choking corrected mass flow for undistorted inlet flow can be written as a function of the total pressure drop only

$$\dot{\mu}^* = \frac{\left(\frac{\dot{m}\sqrt{T_t}}{A\,p_t}\right)^*}{\left(\frac{\dot{m}\sqrt{T_t}}{A\,p_t}\right)^*_{\Delta p_t=0}} = f\left(\frac{\Delta p_t}{p^*}\right) , \quad (3.12)$$

since $(p_t/p)^*$ is a function of $\Delta p_t/p^*$ (Equation (3.10)). The total pressure drop $\Delta p_t/p^*$ was estimated[2] to be about 0.15 with circumferential inlet distortion, yielding $\dot{\mu}^* = 0.973$. The choking

[2]It was assumed that the compressor chokes in the rotor and p^* was approximated by a static pressure measurement at station F (Figure 2-2). The total pressure drop Δp_t was assumed to be one dynamic head at choking.

mass flow of the measured speed lines with circumferential inlet distortion in Figure 3-2 is about 0.978 times the nominal choking mass flow without distortion which matches very well with the computation.

The compound compressible flow analysis and the measurements show that if the total pressure distortion is strong enough, the choking side of the compressor speed line is shifted to lower mass flows.

3.4.2 Compression System Component Coupling with Inlet Distortion

In addition to upstream flow field measurements with circumferential inlet distortion, four circumferentially distributed wall static pressure taps at the hub and casing (station K), and a total pressure and total temperature rake provided data on the flow field downstream of the compressor. Figure 3-5 shows the total and static pressure profiles at the inlet, approximately 1.1 mean radii upstream of the rotor inlet, and the static pressure profile at the compressor exit. The pressures have been normalized by the inlet total pressure of the unspoiled sector.

The inlet static pressure shown in Figure 3-5 is approximately uniform around the annulus, while the exit static pressure is circumferentially nonuniform with an increased pressure rise in the range $120° \leq \theta \leq 240°$. This contradicts the basic Hynes-Greitzer theory ([16]) which assumes that the flow angle from the stator vanes is uniform and that the downstream duct has constant area. In a two-dimensional (incompressible) flow field these assumptions imply uniform exit static pressure and nonuniform inlet static pressure. This discrepancy between the theory and measurements can be explained by considering the compressor *plus* downstream diffuser, and using a parallel compressor type argument as follows (see [22]): In the spoiled sector the diffuser is operating with low inlet total pressure and thus low velocity, producing a lower pressure rise than the diffuser in the unspoiled sector. Since the static pressure at the diffuser exit must be uniform, the static pressure at the compressor exit must be higher in the spoiled sector than in the unspoiled sector.

This coupling of the downstream diffuser with NASA Stage 35 was also verified by Gong [12]. Gong developed a 3-dimensional, non-linear compressor model using a body force approach. The flow field computation of NASA Stage 35 with circumferential inlet distortion is shown in Figures 3-5 and 3-6 as solid lines. The pressure distribution at the inlet and at the exit of the compressor as well as the velocity distribution upstream of the compressor match the measurements very well.

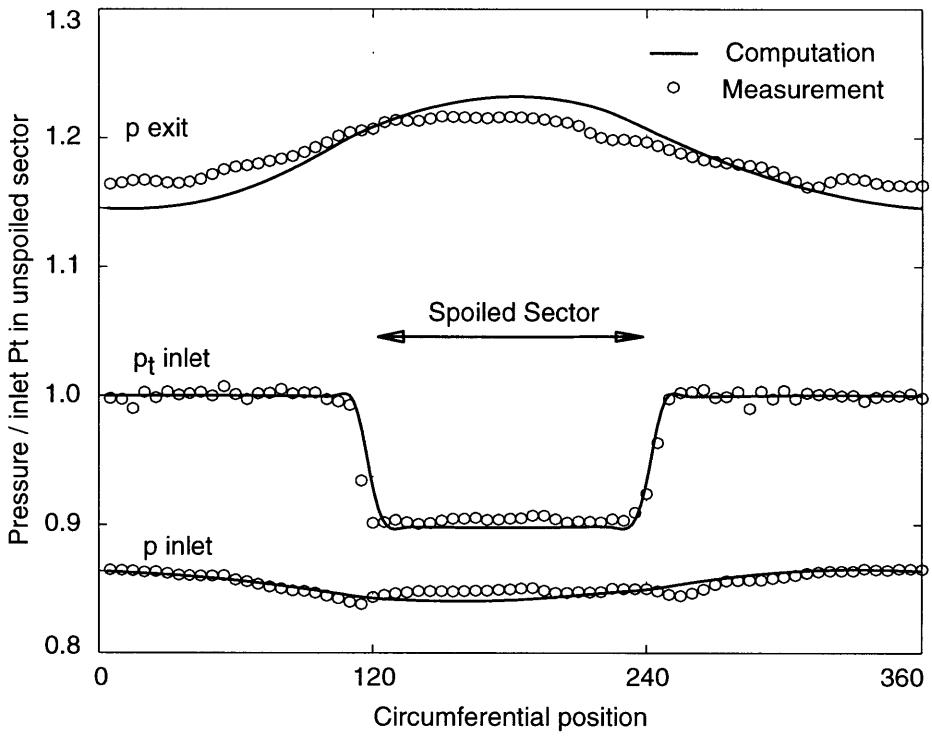

Figure 3-5: Computed ([12]) and measured total and static pressure at the compressor inlet and static pressure at the compressor exit for 1 dynamic head distortion at $\dot{m}_{corr}^{tot} = 16.5$ kg/s without blowing.

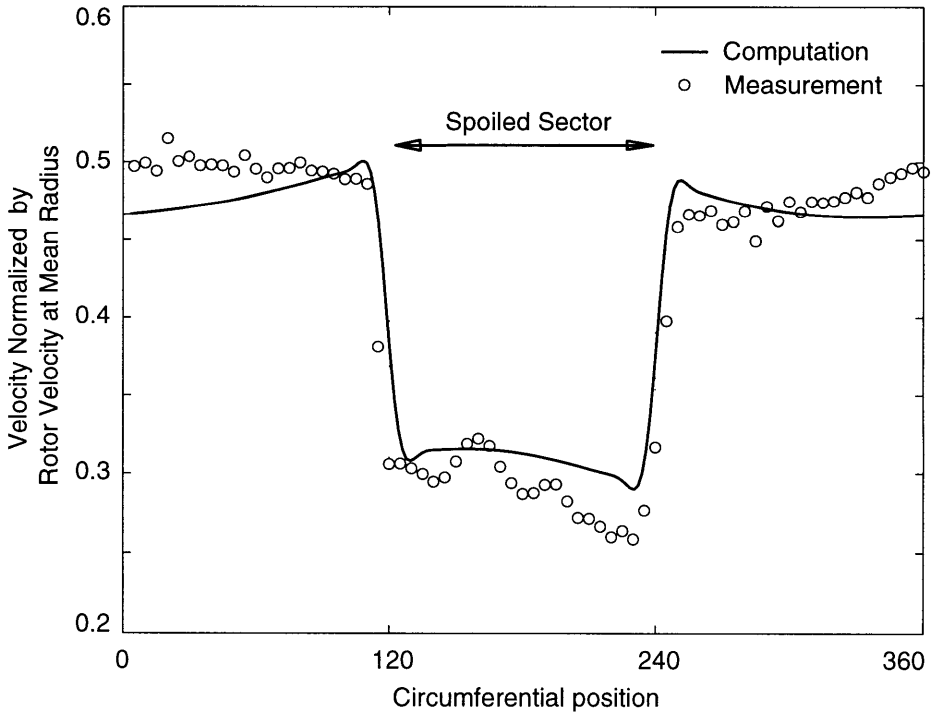

Figure 3-6: Computed ([12]) and measured axial velocity at the compressor inlet for 1 dynamic head distortion at $\dot{m}_{corr}^{tot} = 16.5$ kg/s without blowing.

Chapter 4

Unsteady Compressor Behavior with Distortion

In this chapter, we will show that the dynamic behavior of a compressor stage can be strongly influenced by the total pressure profile at the inlet to the stage. Changes in this inlet total pressure profile can be influenced by radial distortion, which decreases total pressure at the tip, or by injection, which increases total pressure in the tip region. The effect of this on the stall inception pattern is discussed in this chapter.

4.1 Stall Patterns in Stage 35 with Inlet Distortion

Previous stall inception studies and experimental work by Camp and Day [7] have lead to the identification of two common flow breakdown processes in low-speed axial flow compressors. According to Camp and Day, stall can be triggered by short length scale disturbances known as spikes, or by longer length scale disturbances known as waves.

A spike may be described as an embryonic stall cell that is created by the local stalling of a particular blade row. Spikes usually start in low velocity troughs and travel quickly around the annulus between 60% and 80% of rotor speed. The fewer blade passages a stall cell occupies, the faster the spike will tend to rotate ([7]). Once a spike is formed, it quickly increases in size, loses rotational speed and turns into a rotating stall cell. Long length scale waves have been discussed in Section 1.1. Camp and Day [7] describe the nature and the appearance of these two pre-stall flow phenomena in several low-speed compressor configurations and explain the mechanism for each case with a simple model. According to Camp and Day [7] spikes occur when the critical incidence at the rotor tip is reached before the slope of the total-to-static pressure rise characteristic changes from negative to positive ($\frac{\partial \Psi^{ts}}{\partial \phi} \leq 0$), and waves are observed when the peak of the total-to-static pressure

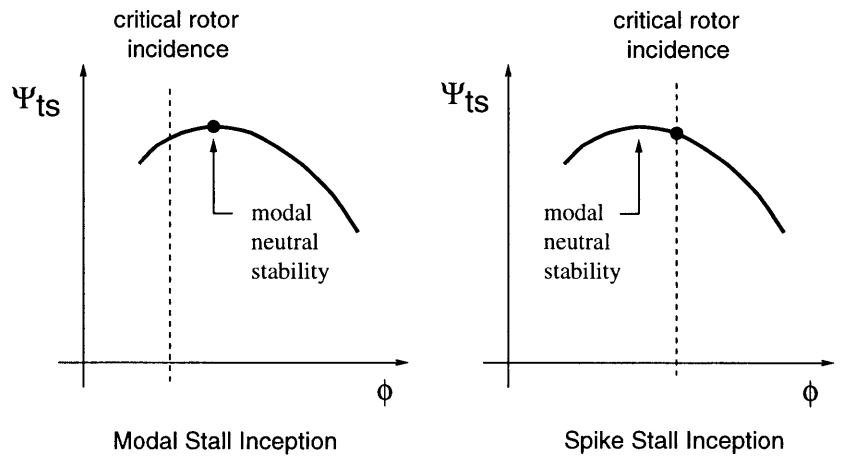

Figure 4-1: Stall inception model according to Camp and Day [7].

rise characteristic (neutral stability, $\frac{\partial \Psi^{ts}}{\partial \phi} = 0$) is reached before critical incidence is exceeded. An illustration is given in Figure 4-1. This has been shown experimentally in a multi-stage low-speed axial compressor, where the effects of stage matching and blade row incidence angles were investigated using variable geometry features of the test compressor. The same stall inception behavior has been observed in a low-speed single-stage axial compressor, where the tip incidence was changed by artificially skewing the flow towards the casing or the hub ([7]).

Figure 3-1 indicates that with radial inlet distortion and no blowing, the current compressor stalls with $\frac{\partial \Psi^{ts}}{\partial \phi} \leq 0$. However with steady blowing the compressor stalls with $\frac{\partial \Psi^{ts}}{\partial \phi} = 0$. According to the Camp and Day model we would therefore expect to find that the path to instability with no blowing is via spikes while the path to instability with blowing is via longer wave length disturbances. The present test results therefore afford us an opportunity to investigate the validity of the Camp and Day model in a transonic compressor.

The first experiment shown in Figure 4-2 is an open loop stall experiment without any injection. Plotted are the eight circumferentially distributed Kulite static pressure traces upstream of the rotor (station F) during the event. The pressure perturbations have been scaled by their mean standard deviations. One can see that there is a spike emerging from the pressure traces several rotor revolutions before stall and traveling very fast (about 74% of rotor speed) around the annulus. Its size is growing quickly while its speed is slowing down and within a few revolutions the spike forms a stall cell with an initial rotation rate of approximately 50% of rotor speed. The fully developed rotating stall cell then travels at a rotation rate of about 40% of rotor speed. The stall inception mechanism in Stage 35 with radial inlet distortion and no blowing is clearly determined by spikes.

In a second experiment the jet-injectors were turned on to a level of 50% steady blowing and the compressor was again throttled into stall. Figure 4-3 depicts the pressure traces during this event.

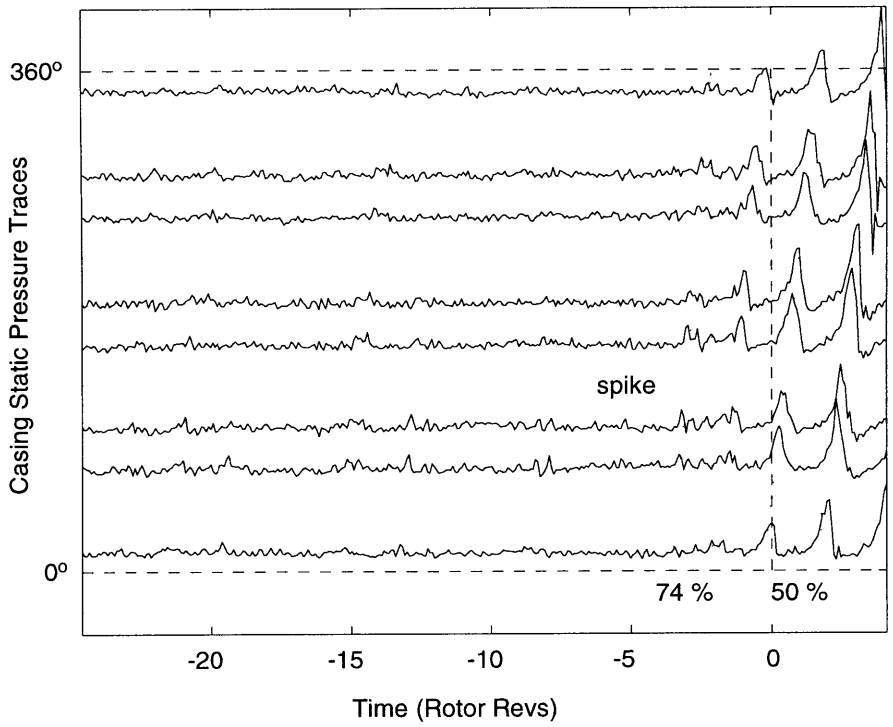

Figure 4-2: Radial inlet distortion and no blowing: spike speed is 74%, initial stall cell speed about 50% of rotor speed (position of trace indicates circumferential location).

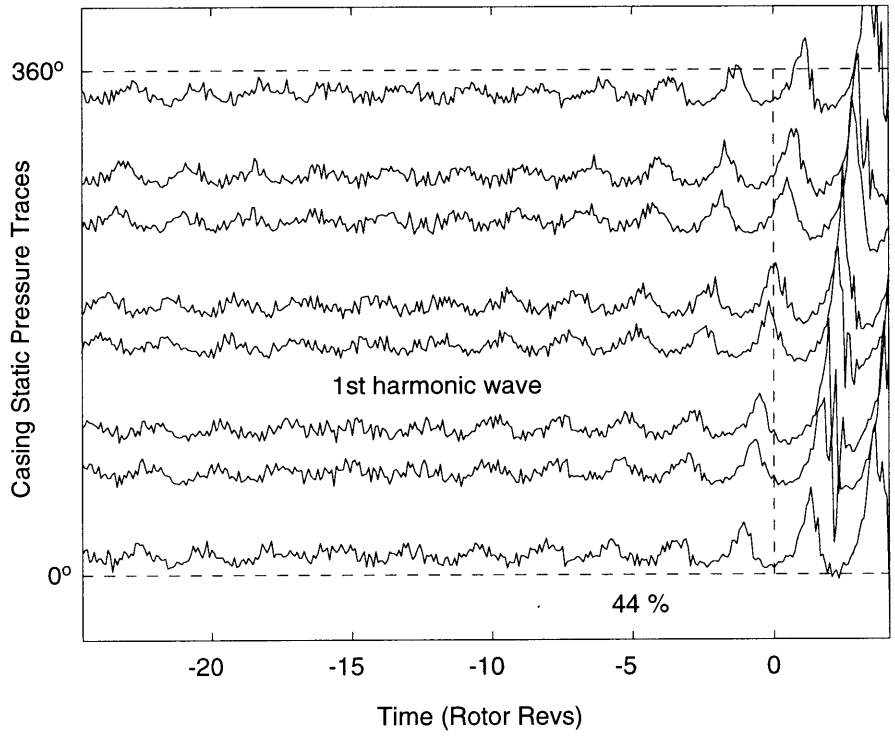

Figure 4-3: Radial inlet distortion and 50% steady blowing: dominant first harmonic modal pre-stall behavior.

The pressure traces reveal a very dominant first harmonic wave traveling around the annulus at about 44% of rotor speed long before the compressor stalls. The amplitude grows as neutral stability is reached and the modal oscillations turn into a stall cell. Note that the wave speed does not change significantly during the transient into stall.

We conjecture that the stall inception mechanism depends on the level of blowing. This link can be explained as follows. The radial distortion screen upstream of the rotor leads to a total pressure loss in the tip region and skews the flow towards the hub region as shown in Figure 2-3. The axial velocity at the casing drops, which causes the incidence and turning in this region to increase. The blades subsequently experience higher loading in the tip region. Critical incidence is therefore exceeded at the blade tip before "system" neutral stability is reached and spikes appear in the pre-stall flow field. When the injectors are turned on, a high momentum jet is blown into the rotor tip region. The increase in tip incidence caused by the distortion screen is reduced due to the higher axial velocities with blowing. This suggests that with blowing, the total-to-static characteristic changes in such a way that neutral stability is reached before the critical incidence occurs; therefore waves develop instead of spikes. This verifies the above described simple model formulated by Camp and Day [7] for a single-stage transonic axial compressor.

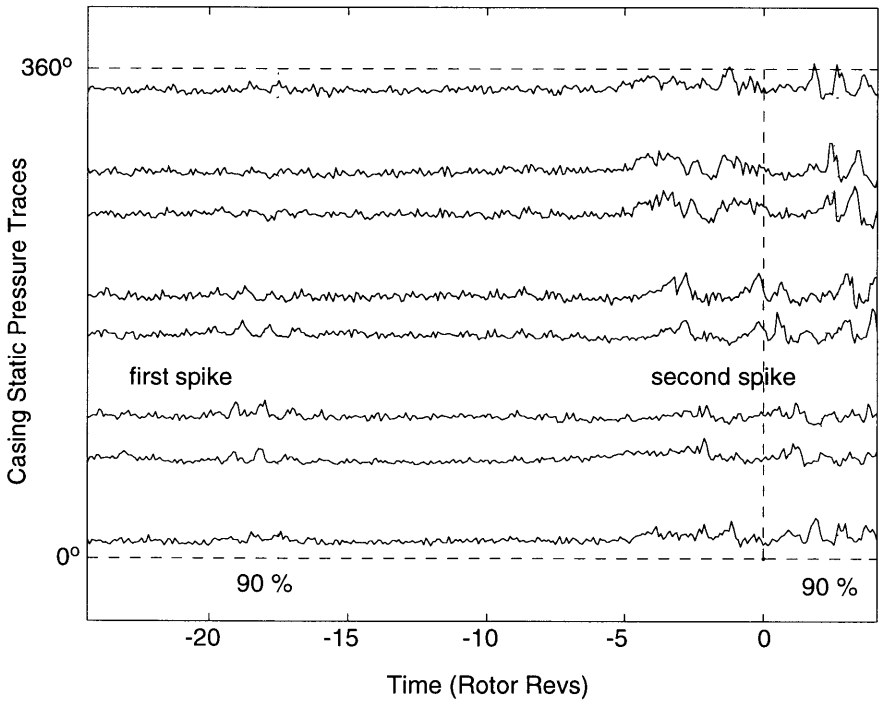

Figure 4-4: Radial inlet distortion and first harmonic robust control law· spike speed is about 90% of rotor speed.

Another interesting result with radial inlet distortion is the pre-stall flow field with active control. A detailed description of the control law design and active control experiments will be given later and only the effect on the stall pattern shall be discussed here. Because the controller was designed to stabilize the rotating stall mode, that is, dampen the long length scale waves, one would expect to see spikes. Pressure traces taken during an active control experiment are shown in Figure 4-4. A spike traveling at approximately 90% of rotor speed emerges about 18 rotor revolutions prior to stall. However, this spike dies out and the spike activity restarts a few revolutions later. The spike does not show a continuous growth. Note that at this time the pressure traces are no longer circumferentially uniform.

The detection of spikes and modes using a correlation integral method was reported by Bright [5], [6]. This algorithm was applied to the data sets discussed above and also to data obtained with circumferential inlet distortion. The detection algorithm yields results consistent with the observations from the pressure traces. In the case of circumferential inlet distortion and no blowing spikes are seen prior to stall as depicted in Figure 4-5. Then these spikes seem to run into a peak of a mode forming and disappear. The machine then stalls due primarily to modal instabilities. When the jet-injectors are turned on to a level of 50% steady blowing, the pressure traces do not indicate spikes and reveal a dominant first harmonic wave before the compressor stalls (see Figure 4-6). This is in very good agreement with results obtained from the correlation integral. For a more detailed description of the detection algorithm and these results see [5].

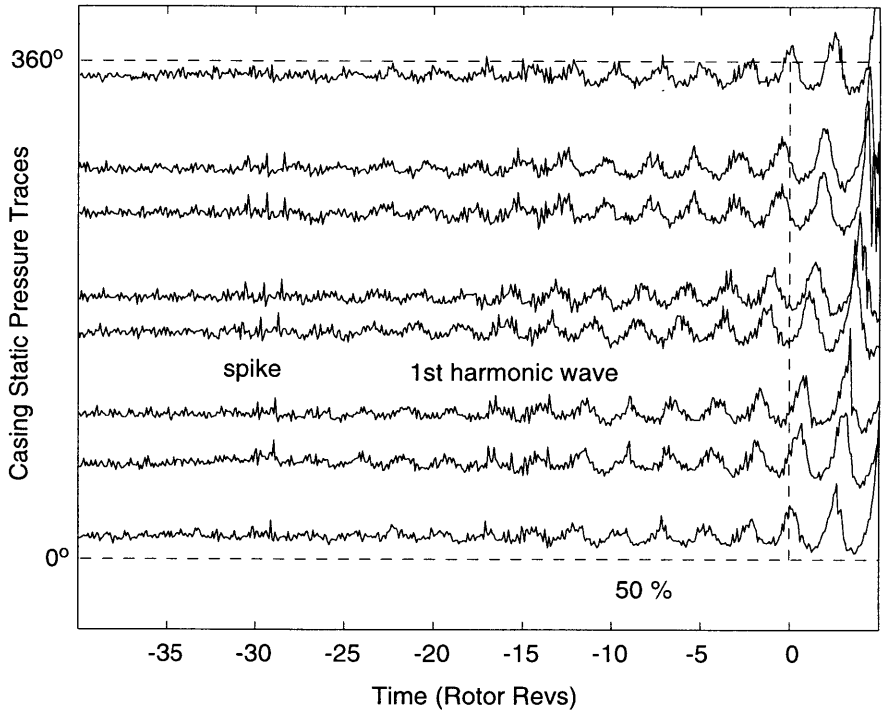

Figure 4-5: Circumferential inlet distortion and no blowing: initial spike and then modal pre-stall behavior.

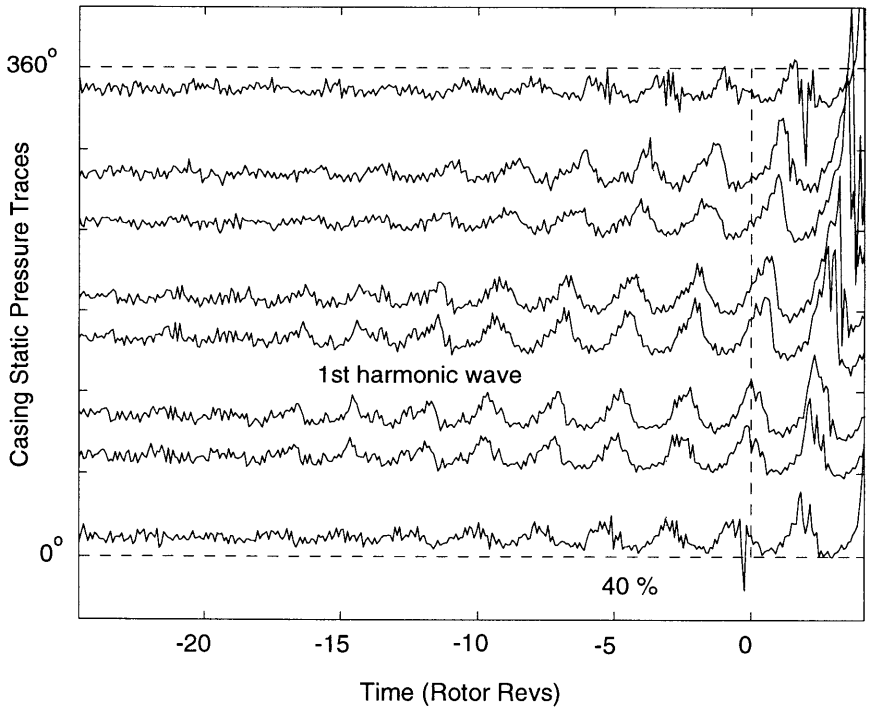

Figure 4-6: Circumferential inlet distortion and 50% steady blowing. dominant first harmonic modal pre-stall behavior.

Chapter 5

Compression System Identification

An important issue and the basis for empirical control law design is a full understanding of the compression system dynamics. Forced response experiments have been conducted to measure compression system transfer functions. Using sinusoidal frequency sweeps on each spatial harmonic, the dominant eigenmodes of the system, their circumferential structure, and the degree of coupling between harmonics that exists in the input-output dynamics are identified. The latter is important for control law design; it is also of interest to determine the degree of coupling between harmonics in *compressible* pre-stall modes. The MIMO system identification framework and results for radial and circumferential inlet distortion are presented in this chapter.

5.1 General Input-Output Compressor Dynamics with Inlet Distortion

All compressor input and output quantities will be defined in terms of spatial Fourier coefficients or SFCs ([26]) denoted by overhead tilde (e.g. $\widetilde{y}_n$ is the nth spatial Fourier coefficient of signal y). If the output vector $\widetilde{\mathbf{y}}$ is defined as the vector of SFCs of the pressure perturbations measured immediately upstream of the compressor rotor (station F) and the input vector $\widetilde{\mathbf{u}}$ contains the corresponding SFCs of the injection signal, the transfer function matrix of the compressor can be written, for example for the first three spatial harmonics as follows

$$\begin{bmatrix} \widetilde{y}_0(s) \\ \widetilde{y}_1(s) \\ \widetilde{y}_2(s) \end{bmatrix} = \begin{bmatrix} G_{00}(s) & G_{01}(s) & G_{02}(s) \\ G_{10}(s) & G_{11}(s) & G_{12}(s) \\ G_{20}(s) & G_{21}(s) & G_{22}(s) \end{bmatrix} \begin{bmatrix} \widetilde{u}_0(s) \\ \widetilde{u}_1(s) \\ \widetilde{u}_2(s) \end{bmatrix}, \tag{5.1}$$

or, in short form

$$\widetilde{\mathbf{y}}(s) = \mathbf{G}(s)\widetilde{\mathbf{u}}(s). \tag{5.2}$$

Note that $\widetilde{y}_i(s)$ and $\widetilde{u}_j(s)$ are *complex* spatial Fourier coefficients (phasors).

For undistorted and circumferentially uniform inlet flow the off-diagonal elements of $\mathbf{G}(s)$ are zero ($G_{ij}(s) = 0$ for all $i \neq j$) because the harmonics are decoupled as discussed in Section 1.1. Therefore, the compressor dynamics for uniform inlet flow can be treated on a harmonic by harmonic basis, and single-input-single-output (SISO) control laws can be designed independently for each harmonic. This was done by Weigl [32] for the compressor being studied in this thesis. We will show that, with radial inlet distortion, the shape of the transfer functions and the trend of decoupled pre-stall behavior are similar to the results reported in [32].

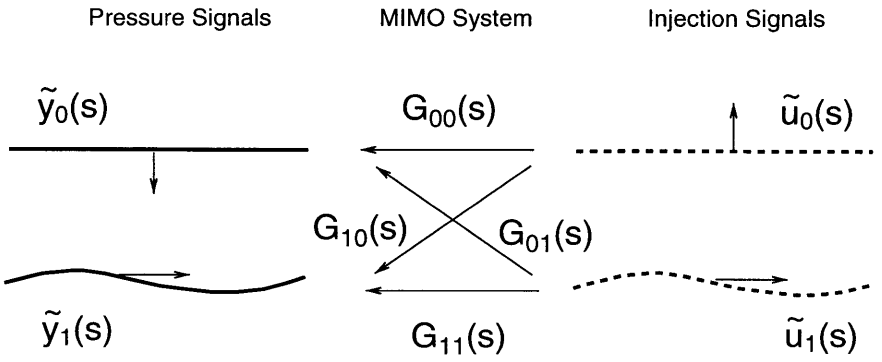

Figure 5-1: Dynamic coupling of a 2 by 2 MIMO system.

If circumferentially nonuniform inlet distortion is present, the harmonics are no longer decoupled and the off-diagonal elements of $\mathbf{G}(s)$ are non-zero ($G_{ij}(s) \neq 0$ for all $i \neq j$). The strength of the coupling between the harmonics can be determined by the magnitudes of these off-diagonal transfer functions. The consequence of this coupling is that the harmonics can not be treated independently as SISO systems. The control problem becomes multi-input-multi-output (MIMO), increasing the complexity of system identification and control law design. This dynamic coupling is illustrated in Figure 5-1 for example for the zeroth and first spatial harmonics; this is a 2 by 2 MIMO system. Injection of a zeroth harmonic pressure pattern has a direct effect (zeroth harmonic pressure signal response) and a coupled effect (first harmonic pressure signal response). The same effect can also be observed in this case for the injection of a first harmonic pressure pattern.

5.2 MIMO System Identification Framework

This section outlines the system identification framework that was used to obtain the MIMO compressor transfer functions. The different steps are discussed in detail and apply for both radial and

circumferential inlet distortion.

5.2.1 MIMO Empirical Transfer Function Estimates

Non-parametric frequency domain characterization of input-output systems, called Empirical Transfer Function Estimate (ETFE), is performed by commanding a "frequency sweep" of a sinusoidal injection pattern over a certain frequency range, and by measuring the corresponding response. Sweeping in frequency is equivalent to rotating the input wave at increasing speed. For example, the first harmonic to first harmonic transfer function $G_{11}(s)$ can be identified by injecting a first harmonic sinusoid $\widetilde{u}_1(s)$ and measuring the compressor response, that is the first harmonic SFC of the pressure perturbations $\widetilde{y}_1(s)$. This is sketched in Figure 5-2.

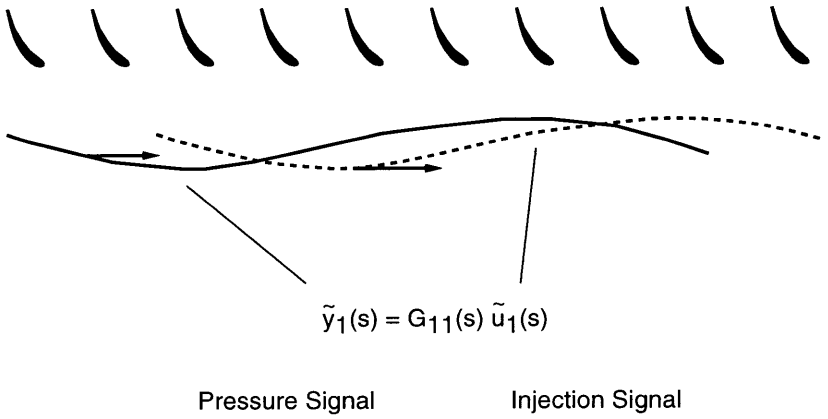

Figure 5-2: Identification of first harmonic to first harmonic compressor transfer function.

The elements of the compressor transfer functions in Equation (5.1) denoted $G_{ij}(j\omega)$, can be computed from the measured signals $u(t)$ and $y(t)$ as follows (for details see [20])

$$G_{ij}(j\omega) = \frac{\Phi_{\widetilde{y}_i \widetilde{u}_j}(j\omega)}{\Phi_{\widetilde{u}_j \widetilde{u}_j}(j\omega)}, \tag{5.3}$$

where $\Phi_{xx}(j\omega)$ is the power spectrum of signal $x(t)$ and $\Phi_{zx}(j\omega)$ the cross spectrum between $x(t)$ and $z(t)$. Note that the spectra are computed for the SFCs of the measured signals.

To determine the accuracy of the transfer function estimate, the coherence between the actuator command input $c(t)$ and plant output $y(t)$ can be computed at each frequency where $u(t)$ and $c(t)$ are coupled through additional actuator dynamics (see Figure 6-1). The coherence $\gamma^2_{\widetilde{y}_i \widetilde{c}_j}(j\omega)$ is then computed as follows:

$$\gamma^2_{\widetilde{y}_i \widetilde{c}_j}(j\omega) = \frac{|\Phi_{\widetilde{y}_i \widetilde{c}_j}(j\omega)|^2}{\Phi_{\widetilde{c}_j \widetilde{c}_j}(j\omega)\Phi_{\widetilde{y}_i \widetilde{y}_i}(j\omega)}. \tag{5.4}$$

The value of $\gamma^2_{\underset{y_i c_j}{\sim}}(j\omega)$ can vary from zero to one and indicates the correlation between the command input and the response of the compressor to this forcing. Low values of coherence reflect that noise or other external forcing sources (e.g. a whirling shaft, rotor noise) are present, and that the input and output signals are not strongly correlated.

5.2.2 MIMO Compressor Transfer Function Identification

The empirical design of control laws requires a parameterized model of the compression system dynamics. FORSE (Frequency Observable Range Subspace Estimation), a state-space system identification program developed at the Space Engineering Research Center at MIT ([17]), was used to identify a model from the measured transfer functions (ETFE's). FORSE allows state-space representations $[\mathbf{A}, \mathbf{B}, \mathbf{C}, \mathbf{D}]$ of measured MIMO transfer function systems. Since FORSE can only be used for transfer function systems with real inputs and outputs, the MIMO system $\mathbf{G}(j\omega)$ defined in Equation (5.2) (which has complex inputs and outputs) must be transformed to a transfer function system with real inputs and outputs. The complex to real transformation is derived in Appendix B.

The compressor dynamics with real inputs and outputs can then be written for example for the MIMO system containing the zeroth, first and second harmonics as

$$\begin{bmatrix} \widetilde{y}_0 \\ \widetilde{y}_1^R \\ \widetilde{y}_1^I \\ \widetilde{y}_2^R \\ \widetilde{y}_2^I \end{bmatrix} = \begin{bmatrix} G_{00}(j\omega) & G^r_{01}(j\omega) & -G^i_{01}(j\omega) & G^r_{02}(j\omega) & -G^i_{02}(j\omega) \\ G^r_{10}(j\omega) & G^r_{11}(j\omega) & -G^i_{11}(j\omega) & G^r_{12}(j\omega) & -G^i_{12}(j\omega) \\ G^i_{10}(j\omega) & G^i_{11}(j\omega) & G^r_{11}(j\omega) & G^i_{12}(j\omega) & G^r_{12}(j\omega) \\ G^r_{20}(j\omega) & G^r_{21}(j\omega) & -G^i_{21}(j\omega) & G^r_{22}(j\omega) & -G^i_{22}(j\omega) \\ G^i_{20}(j\omega) & G^i_{21}(j\omega) & G^r_{21}(j\omega) & G^i_{22}(j\omega) & G^r_{22}(j\omega) \end{bmatrix} \begin{bmatrix} \widetilde{u}_0 \\ \widetilde{u}_1^R \\ \widetilde{u}_1^I \\ \widetilde{u}_2^R \\ \widetilde{u}_2^I \end{bmatrix}, \tag{5.5}$$

where G^r_{ij} and G^i_{ij} are determined by the transformation formulae given in Equations (B.13) and (B.14). Note that the zeroth harmonic transfer function $G_{00}(j\omega)$ is already in real form since the surge-like pressure perturbations are one-dimensional and non-rotating. The original 3 by 3 system defined in Equation (5.1) turns into a 5 by 5 system with real inputs and outputs.

This MIMO system matrix, containing the measured transfer functions (ETFE's) and the corresponding frequency vector ω, form the input quantities to FORSE. The algorithm then searches for *one common* set of poles and zeros for *all* specified transfer functions in Equation (5.5) (in this case 25 transfer functions) by minimizing a certain cost function (for details see [17]). The output is a state-space representation $[\mathbf{A}, \mathbf{B}, \mathbf{C}, \mathbf{D}]$ of the MIMO compression system. The number of common poles, which can be specified in the identification process, determines the overall system order and therefore the dimension of $\mathbf{A}$. The complex conjugate eigenvalue and eigenvector pairs of $\mathbf{A}$ represent the traveling modal perturbation waves of the compression system (remember that the system order was doubled due to the transfer function transformation). The real and imaginary parts of

the eigenvalues of **A** are the growth and the rotational rates of the pre-stall modal waves. Using the corresponding eigenvectors, the mode shapes of the pre-stall waves can be reconstructed.

This system identification frame work is used to identify the compressor dynamics with radial and circumferential inlet distortion.

5.3 Open Loop Compressor Dynamics with Radial Inlet Distortion

Measurements of the zeroth, first and second harmonic transfer functions revealed that the off-diagonal elements $G_{ij}(j\omega)$ for $i \neq j$ have low magnitudes and that the diagonal elements $G_{ij}(j\omega)$ for $i = j$ exhibit roughly the same shape and trends as obtained by Weigl [32] for undistorted inlet flow.

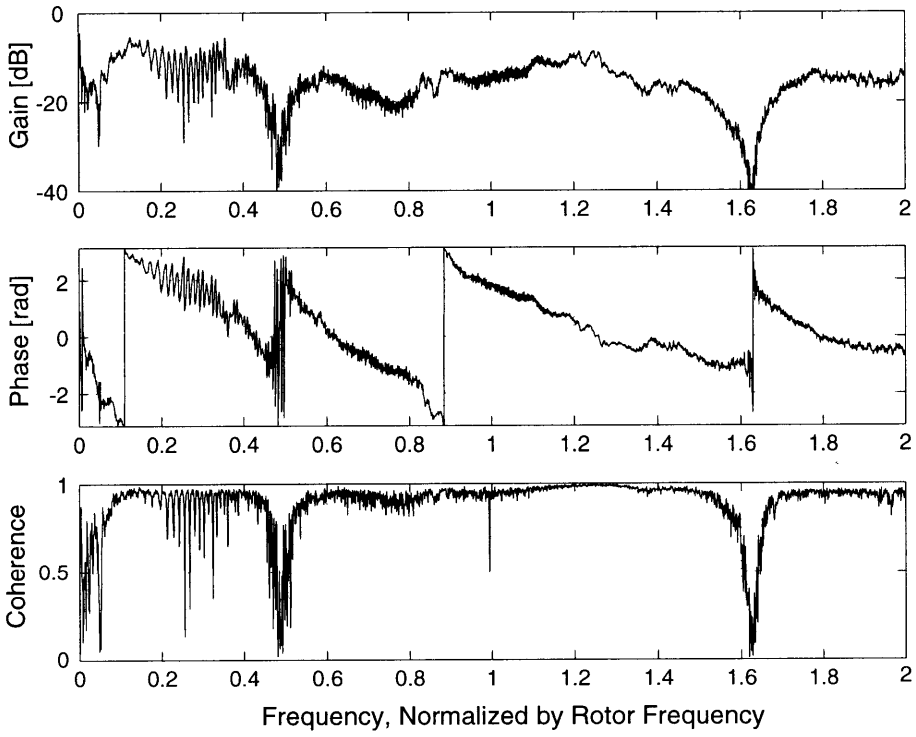

Figure 5-3: Measured 0th harmonic transfer function (ETFE) $G_{00}(j\omega)$ at a corrected total mass flow of 15.6 kg/s

This indicates that, with circumferentially uniform radial inlet distortion, the harmonics are *decoupled.* The measured zeroth and first spatial harmonic transfer functions (ETFE's) are shown in Figures 5-3 and 5-4. The compressor was operated close to stall at a corrected total mass flow of

15.6 kg/s. Plotted are the gain, the phase and the coherence. Notice that multiple lightly damped modes are visible in the transfer functions.

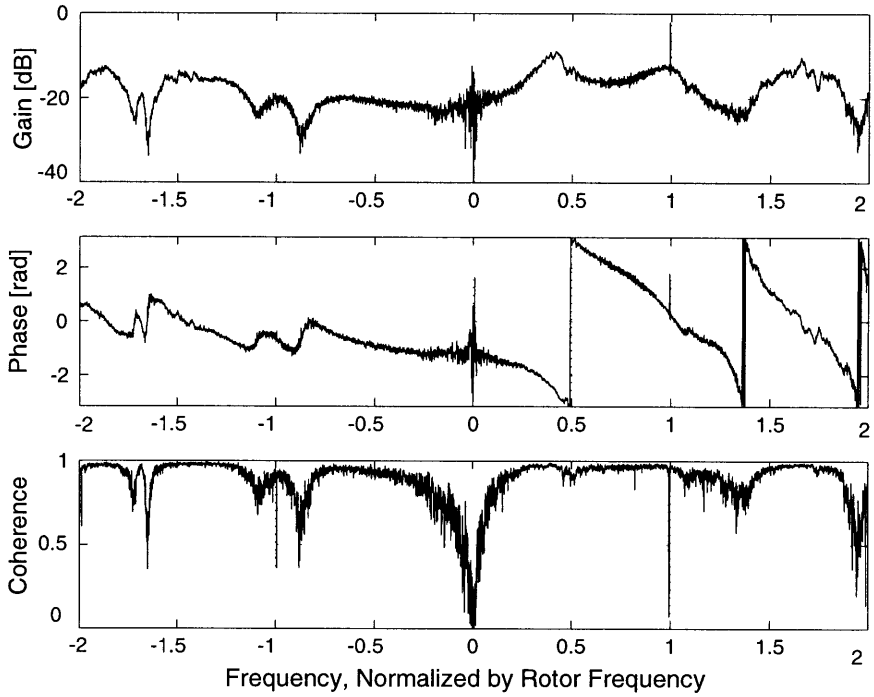

Figure 5-4: Measured 1st harmonic transfer function (ETFE) $G_{11}(j\omega)$ at a corrected total mass flow of 15.6 kg/s.

Open loop stall ramps have also been conducted. The jet-injectors were operated at a 50% steady blowing level while the throttle was closed slowly until the compressor stalled. Pre- and post-stall pressure measurements were taken with eight Kulites located between the jet-injectors and the rotor face (station F). The Kulite pressure signals were decomposed into the first three spatial Fourier harmonics. For each harmonic the evolution of the power spectrum was then computed. Figure 5-5, 5-6 and Figure 5-7 show the evolution of the power density spectrum for the first spatial Fourier harmonic during a stall experiment.

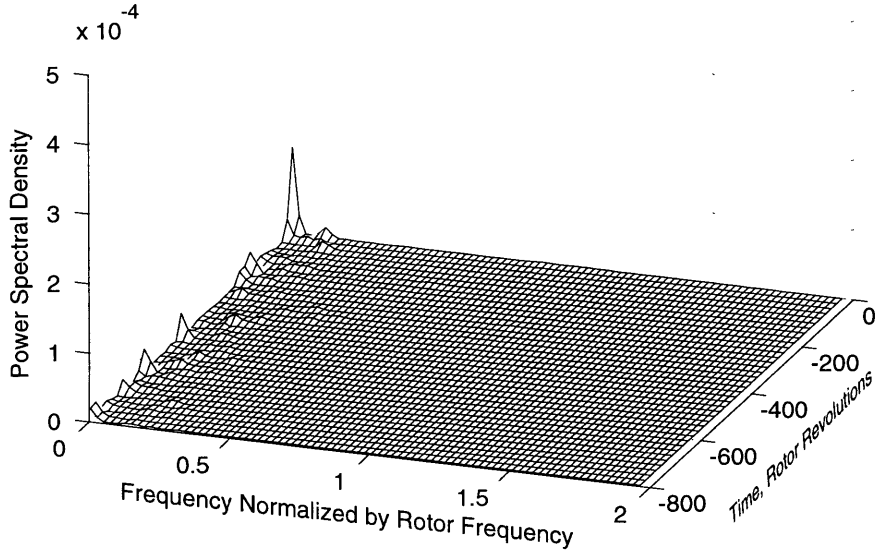

Figure 5-5: Spectrogram of the 0th spatial harmonic pressure perturbations during a stall ramp with radial inlet distortion and 50% steady injection.

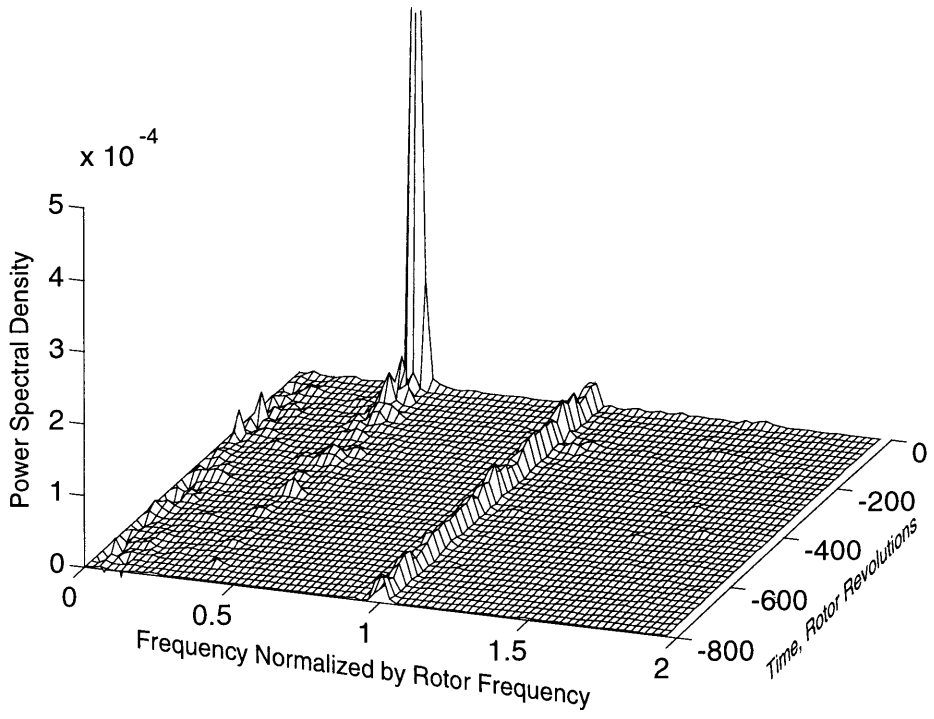

Figure 5-6: Spectrogram of the 1st spatial harmonic pressure perturbations during a stall ramp with radial inlet distortion and 50% steady injection.

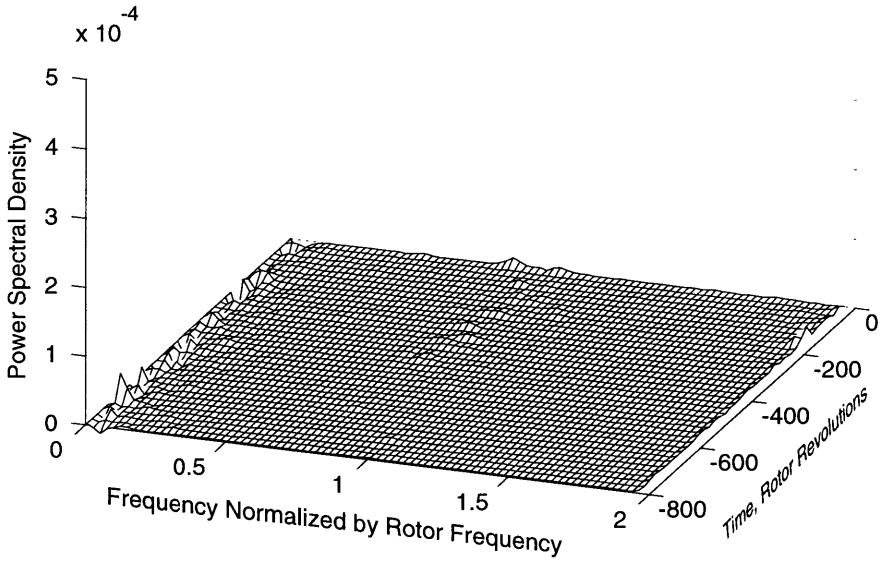

Figure 5-7: Spectrogram of the 2nd spatial harmonic pressure perturbations during a stall ramp with radial inlet distortion and 50% steady injection.

The time axis is in rotor revolutions and the frequency axis is normalized by rotor frequency. One can see that the first harmonic is dominant in the pre-stall dynamics so we will concentrate on it. There are two modes visible in the power density spectrum, traveling at 0.4 and 1 times rotor frequency. To gain further insight about these modes, the first harmonic transfer function $G_{11}(j\omega)$ was measured at different mass flows (15.9 kg/s and 15.6 kg/s) and identified with FORSE. The system order was fixed at 14 (thus 7 pre-stall modes are considered) to reduce the complexity of the compressor model. The identified transfer functions are plotted as dashed lines in Figures 5-8 and 5-9. The compressible modes are denoted by $[n, m]$, where n is inferred from the circumferential harmonic that is largest in mode (here it is the first harmonic $n = 1$), and m indicates the postulated axial mode number. Higher values of m indicate higher frequency and the sign reflects the direction of rotation. Mode $[1, 0]$ is traveling around the annulus at approximately 40% of rotor speed and can be associated with the classical incompressible Moore-Greitzer mode. Mode $[1, 1]$, the first compressible mode, is also visible and travels approximately at the rotor frequency. In Figures 5-8 and 5-9 we see that the magnitude of mode $[1, 0]$ increased significantly when the mass flow was reduced. This indicates that the damping of the mode decreased with the decrease in mass flow. It is mode $[1, 0]$ that loses stability as is clear from Figure 5-6.

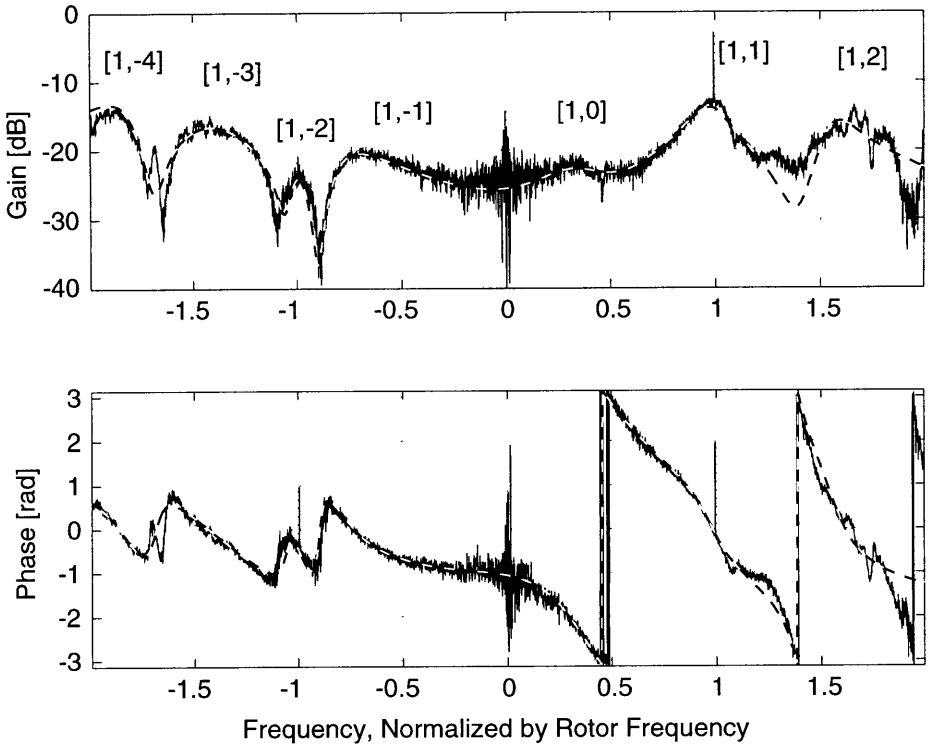

Figure 5-8: Measured (solid) and identified (dashed) 1st harmonic transfer function $G_{11}(j\omega)$ at a corrected total mass flow of 15.9 kg/s.

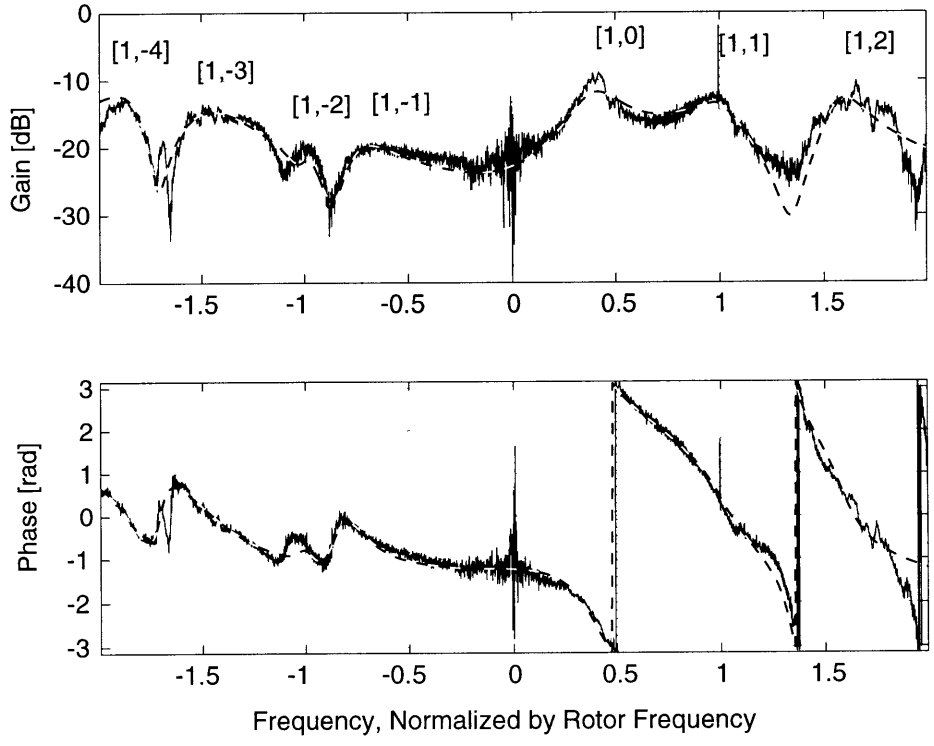

Figure 5-9: Measured (solid) and identified (dashed) 1st harmonic transfer function $G_{11}(j\omega)$ at a corrected total mass flow of 15 6 kg/s.

In summary, the compressible stall dynamics with radial inlet distortion are still *decoupled.* The compressor pre-stall dynamics are dominated by a Moore-Greitzer like mode with strong first harmonic content. Thus SISO control design strategies will be considered for radial inlet distortion.

5.4 Open Loop Compressor Dynamics with Circumferential Inlet Distortion

Similar experiments were conducted with the circumferential inlet distortion screen as follows: first pre- and post-stall Kulite pressure measurements were taken during stall ramps. Again the evolution of the power spectral density of the zeroth, first and second spatial harmonics were computed and are shown in Figure 5-10, 5-11 and Figure 5-12. The results reveal that the mode rotating at 0.4 times rotor frequency, which is strongest in the first harmonic, resonates strongly as the stall point is approached (Figure 5-11). This mode can be related to the incompressible Moore-Greitzer mode, and has also been observed with radial inlet distortion. We note that, even right up to stall, there is relatively little activity at 1 and 1.6 times rotor frequency.

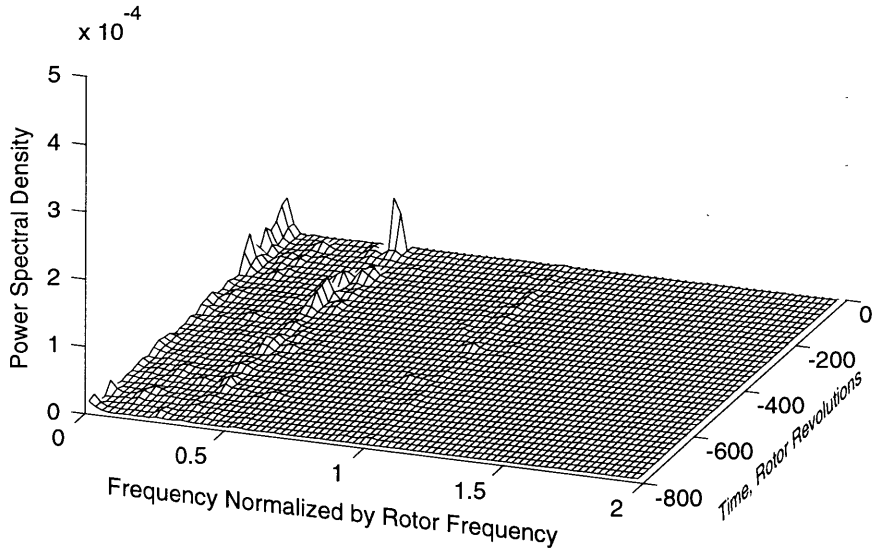

Figure 5-10: Spectrogram of the 0th spatial harmonic pressure perturbations during a stall ramp with circumferential inlet distortion and 50% steady injection.

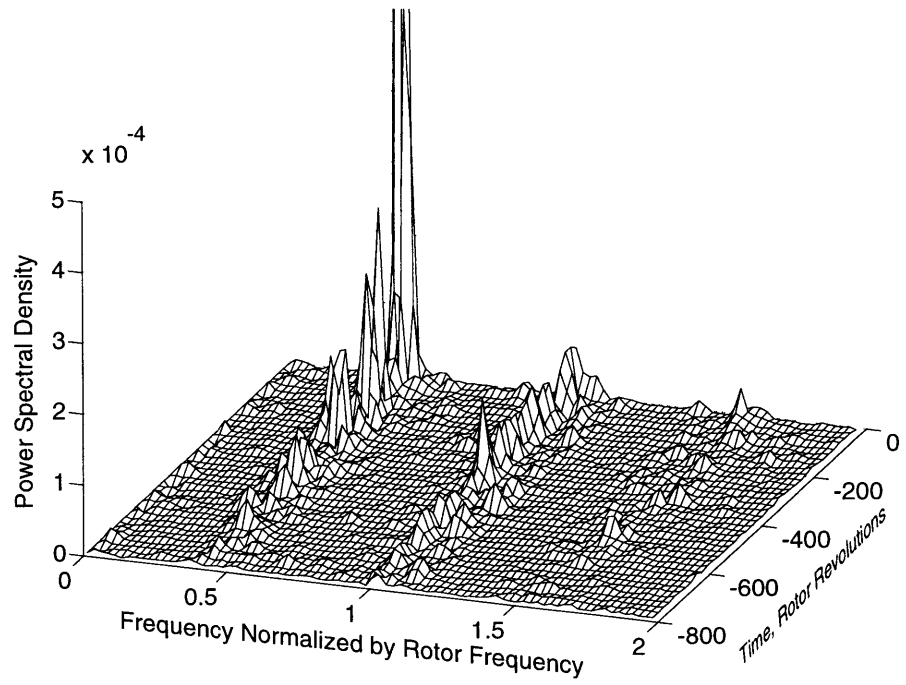

Figure 5-11: Spectrogram of the 1st spatial harmonic pressure perturbations during a stall ramp with circumferential inlet distortion and 50% steady injection.

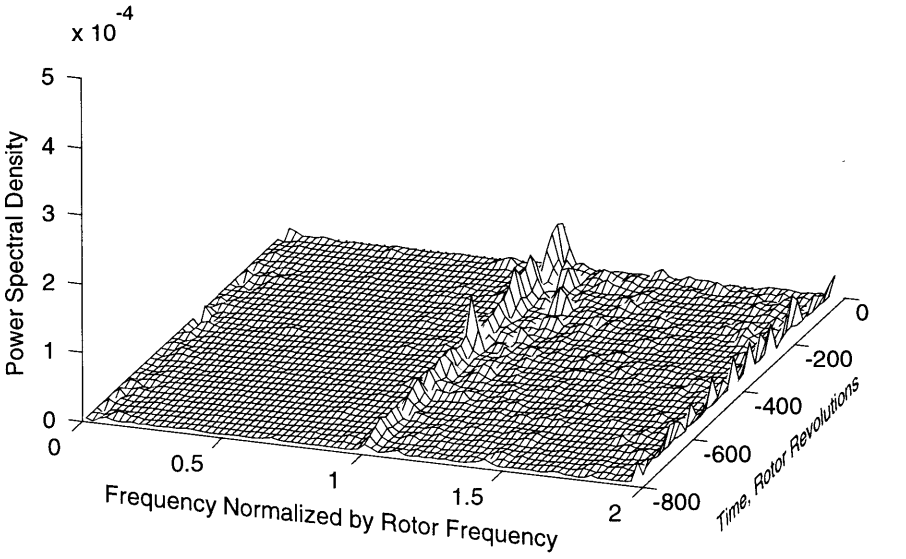

Figure 5-12: Spectrogram of the 2nd spatial harmonic pressure perturbations during a stall ramp with circumferential inlet distortion and 50% steady injection.

However, examination of the power spectra of the zeroth and second spatial harmonic pressure perturbations show that there is some modal activity at 0.4 times rotor frequency in the zeroth harmonic (Figure 5-10) and at 1 times rotor frequency in the second harmonic (Figure 5-12). This has *not* been observed with radial distortion and is the first indication of dynamic coupling effects between the pre-stall modes.

Using the frequency sweep ETFE method described in Section 5.2.1, the transfer function matrix (Equation (5.1)) was measured. The off-diagonal elements, $G_{ij}(j\omega)$ for $i \neq j$, were found to have magnitudes of about 0.1 to 1.0 times the diagonal elements, indicating strong coupling between some harmonics. A subset of the transfer functions is shown in Figure 5-13. The magnitudes of the off-diagonal transfer functions $G_{01}(j\omega)$, $G_{21}(j\omega)$, $G_{10}(j\omega)$ and $G_{20}(j\omega)$ are of the same order as the diagonal transfer functions $G_{00}(j\omega)$ and $G_{11}(j\omega)$. To find the eigenvalues, and for control law design, state-space models were identified (using FORSE) based on the measured MIMO transfer function system. The transfer functions of the identified state space model $[\mathbf{A}, \mathbf{B}, \mathbf{C}, \mathbf{D}]$ are plotted as dashed lines in Figure 5-13. The peaks in the transfer functions indicate that there are several lightly damped modes in the pressure perturbations. Due to compressibility, several modes with similar circumferential structure can exist, each having different axial structure. Therefore we denote the modes by $[n, m]$, where n is inferred from the circumferential harmonic that is largest in the mode, and m indicates the postulated axial mode number (higher values of m indicate higher frequency, usually associated with more axial mode structure, as in acoustics)[1]. Mode number assignment requires careful data reduction and analysis and is described in Section 5.4.1 in further detail.

[1]The mode names used here are primarily for conveying the physical effects involved, and do not effect controller design at all; controllers are based only upon the input-output model.

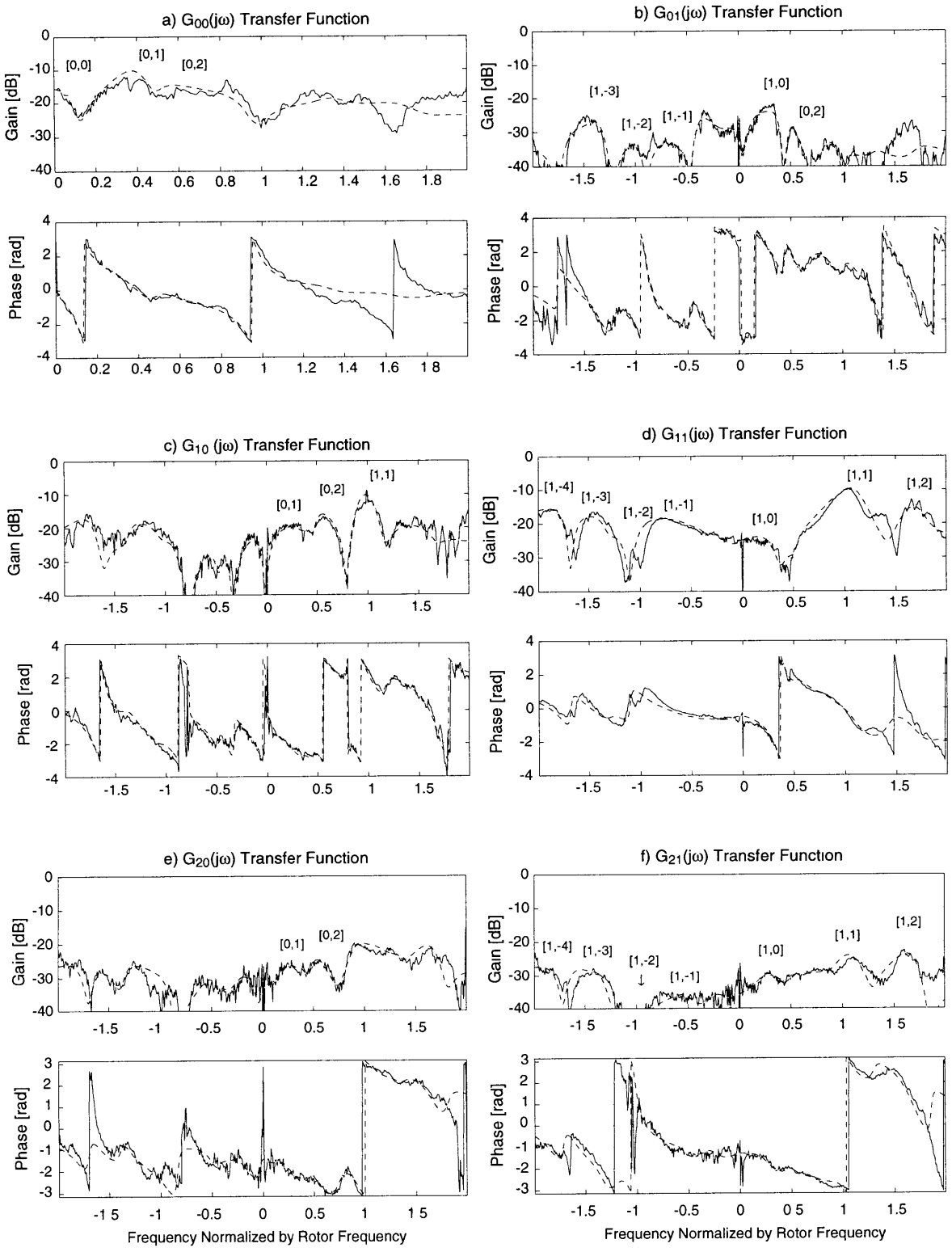

Figure 5-13: MIMO transfer functions $G_{00}(j\omega)$, $G_{01}(j\omega)$, $G_{10}(j\omega)$, $G_{11}(j\omega)$, $G_{20}(j\omega)$ and $G_{21}(j\omega)$ with circumferential inlet distortion at $\dot{m}_{corr}$ = 16.0 kg/s and 85% corrected design speed. —— = measured, – – = identified model.

To study the relative stability and sensitivity to mass flow of the various compressor modes, system identification was conducted at various mass flows. By comparing all of the transfer functions at all the tested mass flows, it was found that the [1,0] mode is primarily responsible for system stability. To summarize this conclusion, Figure 5-14 shows the magnitude and phase of G_{11} measured at four different mass flows. The evolution of the $[1,0]$ mode is particularly noticeable in this figure. As the mass flow is decreased, the magnitude of the peak at 0.4 times rotor frequency

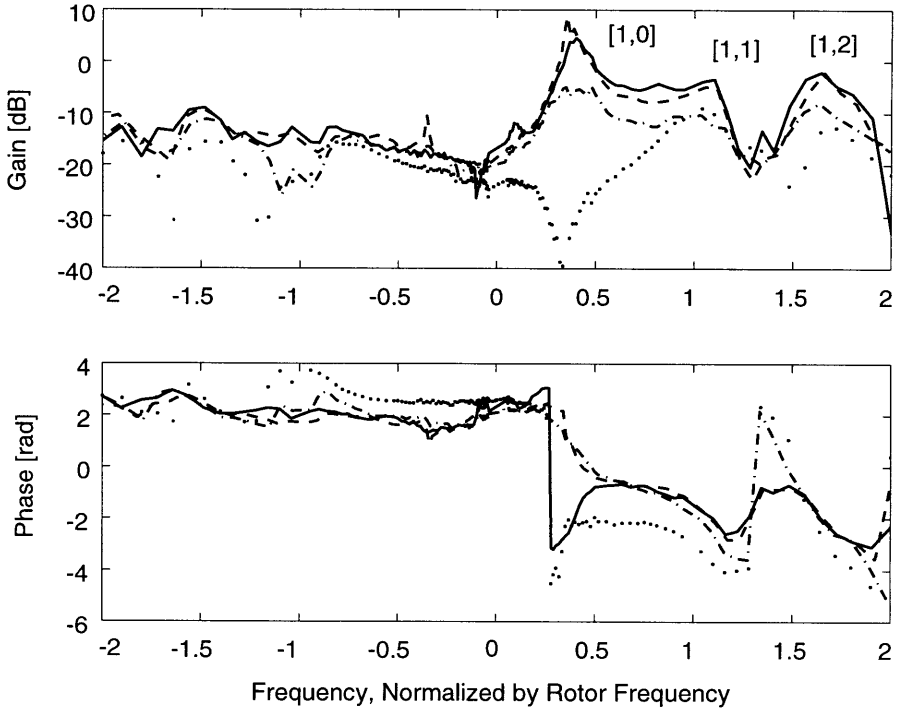

Figure 5-14: Measured $G_{11}(j\omega)$ at 16.0 kg/s (dotted), 15.0 kg/s (dash-dot), 14.7 kg/s (dash) and 14.0 kg/s (solid) total corrected mass flow.

increases, indicating a lightly damped mode. At the lowest mass flow tested this mode is actually unstable (note: the unstable compressor dynamics can only be measured in a closed loop experiment with active control). This can be determined by looking at the corresponding phase plot: for a corrected total mass flow of 14.0 kg/s (solid line), the phase increases in the range $0.3 \leq \omega_r \leq 0.6$, indicating that the pole associated with this mode is unstable. For the corrected total mass flows of 15.0 kg/s (dash-dot) and 14.7 kg/s (dash) the respective phases decrease in the same frequency range, indicating that at these mass flows the mode is stable. Note that for the corrected total mass flow of 16.0 kg/s (dotted) the phase also increases in this frequency range. However, at this high mass flow the mode is stable. The increase in the phase is a result of a zero at 0.35 times rotor frequency which is clearly visible as a deep valley in the magnitude of the transfer function. Note that the compressible modes in Figure 5-14 (labeled $[1,1]$ and $[1,2]$) do not change significantly with

mass flow. These eigenmodes cause peaks in the transfer function which change only slightly as the mass flow is decreased, indicating that their degree of stability is not greatly affected by the decrease in mass flow. Similar conclusions were drawn about other pre-stall modes by looking at the relevant transfer functions and studying eigenvalue migration with mass flow.

5.4.1 Dynamic Coupling Effects with Circumferential Inlet Distortion

Currently no control theoretic, *compressible* model for rotating stall with distorted flow exists to guide the analysis, so one is forced to reconstruct modes directly from the identified model. This is a nontrivial task and the procedure that was used to assign mode numbers is discussed here in detail.

First, to visualize the spatial structure of the modes, the mode shapes are reconstructed using the eigenstructure of the identified state-space model. Remember that each complex conjugate pair of eigenvalues λ_j and λ_{j+1} of $\mathbf{A}$ and their corresponding eigenvectors $\mathbf{v}_j$ and $\mathbf{v}_{j+1}$ represent the ith mode and mode shape of the compression system. The solution to the homogeneous system is therefore

$$\mathbf{x}(t) = \mathbf{V}e^{\Lambda t}\mathbf{z}_o \qquad \text{where} \qquad \mathbf{z}_o = \mathbf{V}^{-1}\mathbf{x}(0) \tag{5.6}$$

are the initial amplitudes of each mode shape and $\mathbf{V}$ is the matrix of eigenvectors $\Lambda = \mathbf{V}^{-1}\mathbf{A}\mathbf{V}$. If we choose the initial state so that only the ith mode is excited, the contribution of this ith eigenmode to the system output can be written as

$$\begin{bmatrix} y_0(t) \\ y_{1R}(t) \\ y_{1I}(t) \\ \vdots \\ y_{nR}(t) \\ y_{nI}(t) \end{bmatrix}_i = \mathbf{C}\left(\mathbf{v}_j e^{\lambda_j t} + \mathbf{v}_{j+1}e^{\lambda_{j+1}t}\right), \tag{5.7}$$

where $y_{nR}(t)$ and $y_{nI}(t)$ denote the real and imaginary parts of the nth spatial Fourier coefficient. Thus, the nth complex spatial Fourier coefficient is

$$\nu_n^{(i)}(t) = y_{nR}(t) + jy_{nI}(t) \tag{5.8}$$

and the mode shape of the ith mode can then be constructed using

$$\delta p(\theta, t)_i = \mathrm{Re}\left\{\sum_{n=0}^{\infty} \nu_n^{(i)}(t)e^{jn\theta}\right\}. \tag{5.9}$$

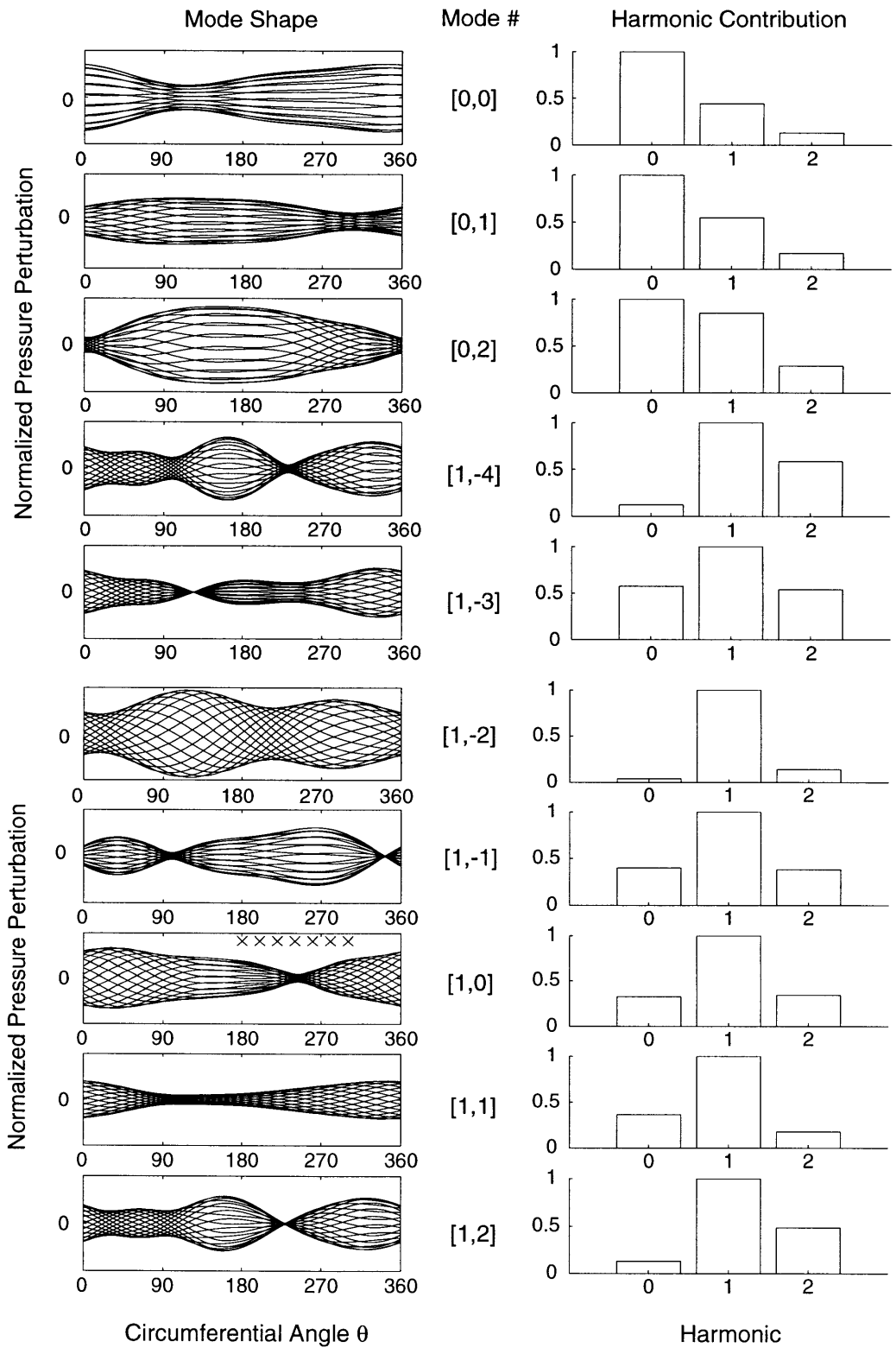

Figure 5-15: Left. mode shapes for the primary modes of the identified dynamics. Right: amplitude of the harmonic contribution to each mode.

Figure 5-15 shows some of the reconstructed mode shapes, plotted in several positions as the eigenmode travels around the annulus. The harmonic content is also plotted, indicating which harmonic dominates and the degree of coupling between harmonics. Vertical scales are arbitrary, since only the mode shape is shown. For these experiments the distortion screen ranged from 180° to 300° — this is marked with ×'s in Figure 5-15. Next, the number n is assigned based on the harmonic which contributes most to the mode shape. The first two modes in Figure 5-15 have strong 0th harmonics, indicating that overall compression system parameters (such as duct lengths and plenum size) will have a strong influence on their stability. The second two modes have strong 1st harmonics, and it will be shown that stabilization of these modes can be achieved by controlling the first harmonic of the flow perturbations. Finally, the "acoustic" mode number m is assigned by looking at various factors. Higher frequencies are considered to be more acoustically coupled, and are given larger values of m. Note that the mode shape, and therefore the harmonic content of each mode, is a function of time. Figure 5-15 thus portrays the modes at several specific instants in time. Eigenvalues obtained without distortion [33] are compared to those found here, to judge how distortion has altered their frequency, stability, and harmonic content; this also helps to assign the mode numbers. In addition, low speed modeling ([30]) is employed to help associate mode numbers with the peaks when strong coupling is present. The results are summarized in Figure 5-16, which shows the identified poles and assigned mode numbers.

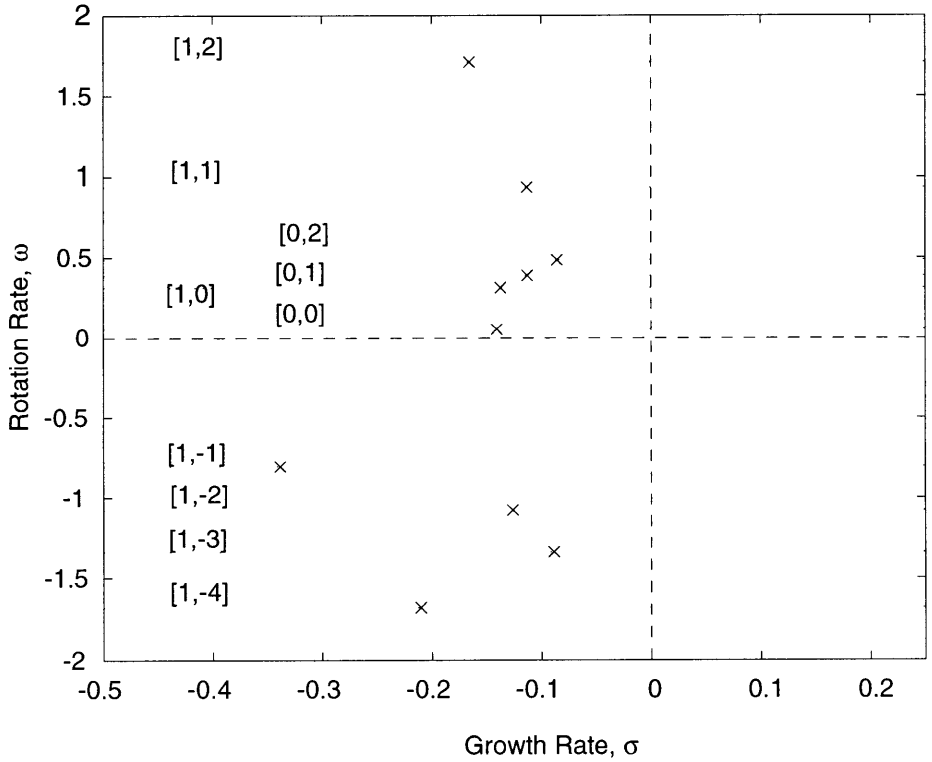

Figure 5-16: Identified poles of the multi-variable transfer function system at $\dot{m}_{corr}^{tot} = 16.0$ kg/s

Several statements can be made based on Figure 5-15. First, note that the mode shape of mode $[1,0]$ has a minimum at approximately 250°, which is about in the middle of the distorted region. This behavior is predicted by the low-speed model and has been observed in a low-speed compressor by Van Schalkwyk [31]. Furthermore, the Fourier decompositions of the mode shapes, shown in the right hand graphs of Figure 5-15, indicate that several harmonics are present in each mode; this is also predicted by incompressible theory. The compressible modes $[0,1]$ and $[1,1]$, on the other hand, represent an effect which has not yet been modeled: it appears that these higher frequency, compressible dynamics are also coupled, to an extent very similar to the incompressible dynamics, by inlet distortion. Finally, note that the richness of the dynamics displayed in Figure 5-13 and Figure 5-15 makes the control problem more complex, but this complexity is mitigated by the fact that some of the high frequency modes are relatively well damped, and do not tend to go unstable as mass flow is reduced.

In summary, in the presence of circumferential distortion, the stability of the compression system is determined by the $[1,0]$ mode. This behavior is analogous to that observed in low-speed compressors. Unlike radial distortion, there is strong *coupling* between the harmonics, that is, each mode contains several harmonics. This coupling is considered during design and testing of controllers to stabilize the compression system, discussed in the next two chapters.

Chapter 6

Control Law Design

This chapter discusses the design of active control laws. Two major control strategies for active rotating stall control are described in detail: a simple constant gain control strategy and a more sophisticated robust control strategy. For both control laws the closed loop system depicted in Figure 6-1 is considered.

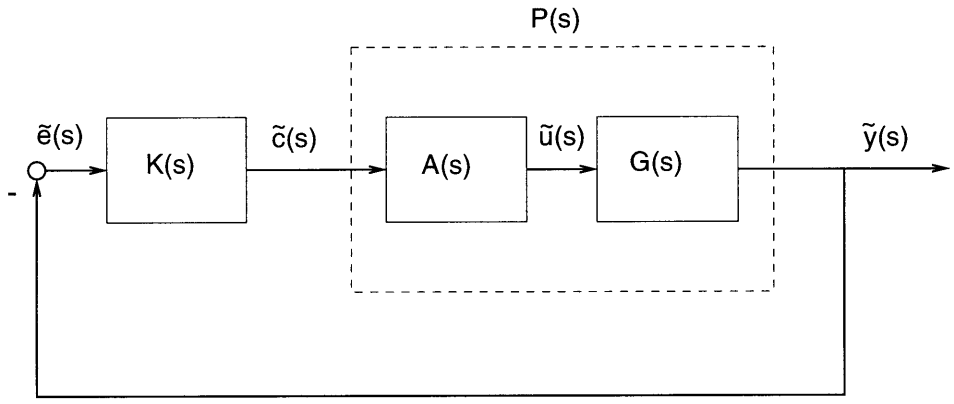

Figure 6-1: Closed loop control system.

The inputs to the MIMO feedback controller $\mathbf{K}(s)$ are the computed SFCs $\widetilde{y}_i(s)$ (output of the compressor transfer function in Equation (5.1)) of the measured pressure perturbations. The controller outputs are the actuator commands $\widetilde{c}_i(s)$, which are modified by the actuator dynamics of the jet-injectors $\mathbf{A}(s)$ to give the actual injection pattern, represented by $\widetilde{u}_j(s)$. These are the inputs to the compressor transfer function system $\mathbf{G}(s)$ (see Equation (5.1)). The actuator dynamics $\mathbf{A}(s)$ and the compressor transfer function system $\mathbf{G}(s)$ form the plant $\mathbf{P}(s)$ which will be considered in the control law design process. Note that the feedback control system is a *regulator* system since the error signal is composed only of the measured flow field perturbations. The purpose of the regulator is to drive the pressure perturbations to zero, even if the plant is unstable.

The control law is implemented with the control computer as illustrated in Figure 6-2. The measured static pressure signals $e(t)$ (eight sensors at station F) are converted from analog to a digital (ADC) and conditioned with a first order Butterworth high pass filter (corner frequency 0.1 Hz). This signal conditioning is used since flow perturbations are required for feedback control. The filtered pressure perturbations are then decomposed into spatial harmonics $\widetilde{e}_i(z)$ via a Discrete Fourier Transform (DFT). The spatial harmonic signals are the inputs to the multi-input-multi-output digital control law $\mathbf{K}(z)$. The actuator commands for the twelve actuators $c(t)$ are then computed with the Inverse Discrete Fourier Transform (IDFT) of the spatial harmonic control commands $\widetilde{c}_i(z)$. The actuator commands are finally converted through a digital-to-analog converter (DAC) and outputted to the servo-motors.

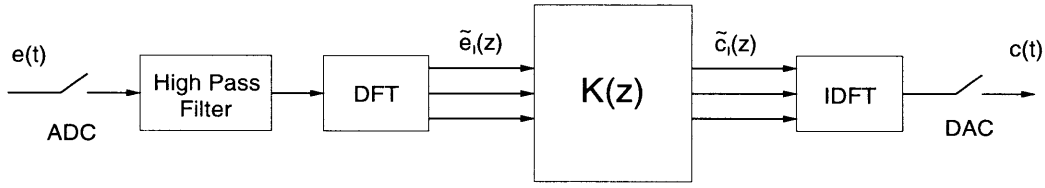

Figure 6-2: MIMO spatial harmonic control of NASA Stage 35.

6.1 Constant Gain Control

Constant gain control has been used successfully by several researchers to stabilize rotating stall in low-speed compressors. Paduano [26] developed the experimental design procedure on a single-stage compressor, and Haynes [14] applied it to a three-stage compressor. The same approach was used by Van Schalkwyk [31] to stabilize a three-stage compressor with circumferential distortion of the inlet total pressure.

The idea behind constant gain control is as follows. The circumferential pressure perturbation $\delta p(\theta)$ is measured and decomposed in a Fourier series analogous to Equation (1.3). The nth harmonic is then spatially rotated by an experimentally optimized angle β_n and multiplied by a constant gain k_n to form the nth harmonic of the control signal. For example, for a sensed first harmonic perturbation $\widetilde{y}_1 = \delta\widetilde{p}_1$ the constant gain control law is

$$\widetilde{u}_1 = -k_1 e^{\jmath\beta_1}\delta\widetilde{p}_1 \tag{6.1}$$

where $\widetilde{u}_1$ is the corresponding first harmonic SFC of the injection wave. Finally, the individual actuator commands are reconstructed based on the Fourier coefficients. Note that this simple constant

gain control law could also account for coupling between harmonics if cross-feed gains and phase angles are included. However, for all experiments presented in this research, the cross-feed channels were set to zero. Hence considering the first three harmonics only, the controller matrix $\mathbf{K}(z)$ is of the following form:

$$\mathbf{K}(z) = \begin{bmatrix} k_0 & 0 & 0 & 0 & 0 \\ 0 & k_1 \cdot \cos(\beta_1) & -k_1 \cdot \sin(\beta_1) & 0 & 0 \\ 0 & k_1 \cdot \sin(\beta_1) & k_1 \cdot \cos(\beta_1) & 0 & 0 \\ 0 & 0 & 0 & k_2 \cdot \cos(\beta_2) & -k_2 \cdot \sin(\beta_2) \\ 0 & 0 & 0 & k_2 \cdot \sin(\beta_2) & k_2 \cdot \cos(\beta_2) \end{bmatrix}, \tag{6.2}$$

which is in real form consistent with Equation (5.5). The constant gains k_i and phase angles β_i are found and optimized experimentally. Thus this control strategy does not require a compressor model nor the knowledge of the dynamics and is very simple to implement. The major drawback is that each spatial harmonic control law has two degrees of freedom only (gain and phase for each spatial harmonic). This limitation is detrimental in machines where compressible modes are important, as will be discussed in the next chapter.

6.2 Robust H_∞ Control

A sophisticated, model-based dynamic controller, the H_∞ robust control law, was successfully used by Weigl [33] on the same compressor with undistorted inlet conditions. This approach is in general not limited to SISO systems, but can be used for MIMO control problems as well. The reader is referred to Kwakernaak [19], Smith [29], and Weigl [33] for a detailed overview of the topics discussed below.

Robust H_∞ control is a linear, time invariant control strategy that allows unknown disturbances, unmodeled dynamics and uncertainties in the plant dynamics. These uncertainties are lumped into a perturbation structure $\Delta(s)$ and are included in the design process. The standard H_∞ problem is shown in Figure 6-3. The plant inputs are the unknown disturbances $\mathbf{w}(s)$ and the control commands $\mathbf{c}(s)$. The outputs are error signals $\mathbf{z}(s)$ (which should be kept small) and the measured pressure perturbations $\mathbf{y}(s)$. The closed loop disturbance-to-error transfer function $\mathbf{T}_{zw}(s)$ is of primary interest. The goal of this robust design procedure is to keep the error signals small given the disturbances which drive the plant. Thus the standard H_∞ control problem is to find a controller $\mathbf{K}(s)$ such that the ∞-norm of the closed loop disturbance-to-error transfer function is less than one:

$$\|\mathbf{T}_{zw}(j\omega)\|_\infty < 1 \,, \tag{6.3}$$

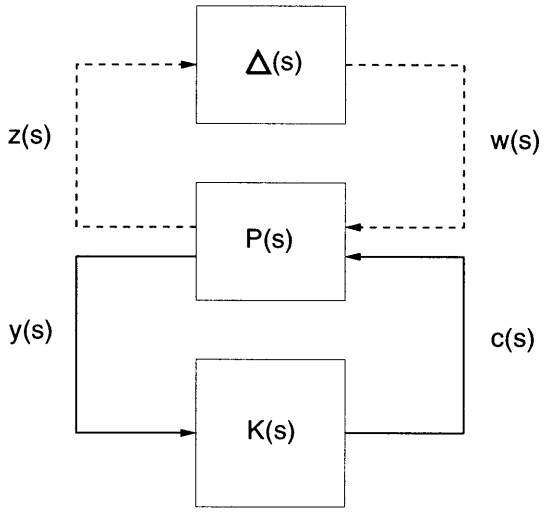

Figure 6-3: Robust control problem.

given that the perturbation dynamics $\Delta(j\omega)$ are stable and that the error and disturbance signals have been scaled so that

$$\|\Delta(j\omega)\|_\infty < 1 \,. \tag{6.4}$$

The ∞-norm of a matrix is the maximum of the largest singular value over the frequency range. In this context, the singular values of a MIMO transfer function matrix can be associated with the gain information of a SISO transfer function. The small gain theorem proves that finding such a solution will ensure a stable closed loop system. In order to satisfy Equation (6.3) and to shape sensitivity and controller transfer functions, the nominal plant is augmented with weighting functions. The optimal H_∞ controller is then found by solving an observer and a controller Algebraic Riccati equation ([19]).

Depending on the model problem, different weighting schemes are used. The basic concept of the control design strategy for rotating stall control is a *mixed sensitivity* H_∞ problem modified with *eigenvalue perturbations*, since the task here is not to solve a tracking problem but to stabilize the compressor. For a common mixed sensitivity problem the weighting functions are the sensitivity shaping function $\mathbf{W}_e(j\omega)$, weighting the error signal $\mathbf{e} = \mathbf{w} - \mathbf{y}$, the controller shaping function $\mathbf{W}_u(j\omega)$, shaping control gain and bandwidth, and the closed loop shaping function $\mathbf{W}_y(j\omega)$. The closed loop transfer function from the reference input ($\mathbf{r} = \mathbf{w}$) to the measured output ($\mathbf{y}$) is also known as the complimentary sensitivity transfer function. The inverse of the weighting functions are the desired sensitivity bounds, the desired controller transfer function limits and the desired closed loop transfer function limits in order to satisfy Equation (6.3).

The Stage 35 control law design process includes choosing the weightings $\mathbf{W}_u(j\omega)$ and $\mathbf{W}_y(j\omega)$,

where the inverse of the weighting functions are chosen to be of the form

$$\mathbf{W}(s)^{-} = k_{\mathrm{dc}} \frac{s + \omega_c}{s \cdot k_{\mathrm{dc}} + \omega_c} \,. \tag{6.5}$$

The design parameters for each of the weightings are the DCgain k_{dc} and the corner frequency ω_c. The sensitivity weighting is replaced by the recently developed eigenvalue perturbation weighting to account for uncertainty in the pre-stall mode locations. Smith [29] developed this technique to allow the designer to center circular uncertainty regions around the plant eigenvalues in the H_∞ control design process using standard Gerŝgorin arguments (the eigenvalues of a matrix are located within the union of circles which are determined by the sum of certain elements of the matrix). The design parameters for the eigenvalue perturbation weighting are the number of perturbed eigenvalues and the radius of the circular bounds. In closed loop, the resulting controller will stabilize the plant as long as the eigenvalues stay within the boundaries of the uncertainty circles. See Weigl [33] for a more detailed description of the application of Smith's technique to rotating stall control.

This H_∞ control design technique is applied to the compression system plant $\mathbf{P}(s)$ and can be used for SISO and MIMO systems. The next sections outline the H_∞ control law design for radial and circumferential inlet distortion.

6.2.1 SISO H_∞ Controller for Radial Inlet Distortion

As discussed in Section 5.3, a first harmonic SISO controller will be considered for radial inlet distortion. Using the identified model shown in Figure 5-9 a robust, linear, dynamic H_∞ controller was designed to stabilize the $[1, m]$ modes. Such a control law can only be designed using a model of the unstable compressor dynamics. Since, on one hand, a theoretical model is not yet accurate enough ([32]) and, on the other hand, it is difficult to measure the unstable dynamics of the compressor, an estimated unstable identified model was used. The estimated unstable model was obtained by extrapolating (from Figures 5-8 and 5-9) the pole migration of the $[1, 0]$ mode to mass flows where the mode becomes unstable. It was assumed that the other modes do not significantly change in growth rate during a throttle ramp; this assumption is consistent with the results in Figures 5-8 and 5-9. Based on these estimated unstable dynamics, an H_∞ controller was designed with five eigenvalue perturbation circles as shown in Figure 6-4. Note that the eigenvalues of $\mathbf{A}$ are the poles of the compression system and that 14 states have been used to represent 7 oscillatory poles of $G_{11}(j\omega)$ which are plotted as x's in Figure 6-4. System order was kept low to limit the complexity of the design process as well as of the resulting control law. Also note that mode $[1, 0]$ is assumed to be unstable for the control law design. The circles (the scales in Figure 6-4 make them appear to be ellipses) represent uncertainty in the eigenvalue location. Also, note that the big circle around mode $[1, 0]$ covers positive (unstable) as well as negative (stable) eigenvalue locations to ensure that

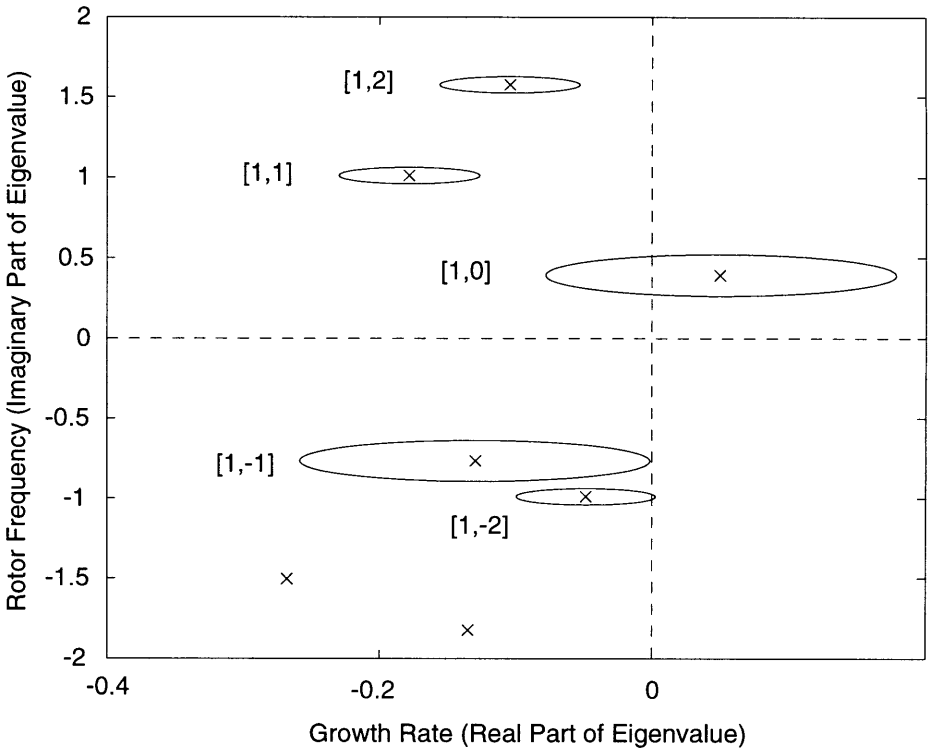

Figure 6-4: Eigenvalue perturbations for SISO design model for 1st harmonic robust control with radial inlet distortion.

the controller does not destabilize the compressor at higher mass flows where mode $[1,0]$ is stable.

6.2.2 MIMO H_∞ Controller for Circumferential Inlet Distortion

Since circumferential inlet distortion introduces dynamic coupling between the pre-stall modes, all circumferential harmonics have to be included in the control law design. Based on the open loop results discussed in Section 5.4, MIMO robust H_∞ controllers were designed. Two MIMO controllers are presented here.

The first MIMO controller was designed based on a fitted 0th and 1st harmonic transfer function system. 26 states were used to represent 13 pre-stall modes with 0th and 1st harmonic content (this transfer function system is not presented). The first two modes, mode $[0,0]$ and mode $[1,0]$, were extrapolated to lower mass flows close to neutral stability. In order to obtain a stable solution and due to the high number of plant states, three eigenvalue perturbation circles of moderate size have been considered for the surge-like $[0,0]$ mode, for the rotating stall-like $[1,0]$ mode, and for the first compressible mode $[1,1]$. In the experiment, both the 0th and 1st harmonic pressure perturbations are fed back to the controller and an unsteady injection pattern is commanded based on the MIMO control law. Figure 6-5 shows the MIMO design model for 0th and 1st harmonic robust control with circumferential inlet distortion.

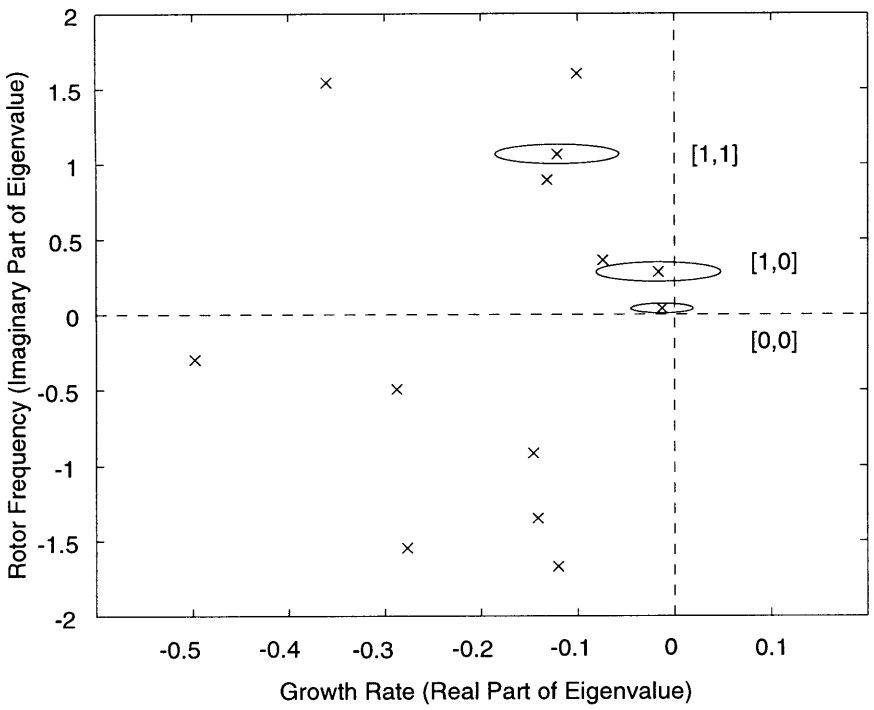

Figure 6-5: Eigenvalue perturbations for MIMO design model for 0th and 1st harmonic robust control with circumferential inlet distortion.

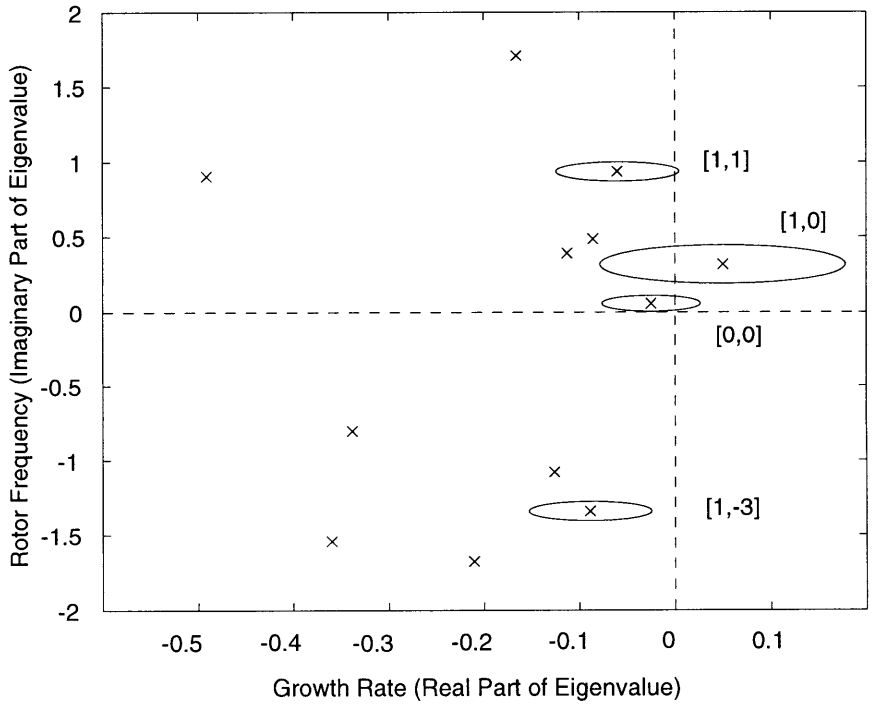

Figure 6-6: Eigenvalue perturbations for MIMO design model for 0th, 1st and 2nd harmonic robust control with circumferential inlet distortion.

The second MIMO controller was designed using the identified compressor transfer function system including the 0th, 1st and 2nd spatial harmonics as discussed in Section 5.4. A total of 12 pre-stall modes (also shown in Figure 5-16) were represented using 24 states. Since the rotating stall-like $[1, 0]$ mode determines stability, this mode is migrated to an unstable mass flow. In addition, the surge-like mode $[0, 0]$ and the first compressible mode $[1, 1]$ are also extrapolated to lower mass flows but are still on the stable side. Four eigenvalue perturbation circles are considered in the controller design as shown in Figure 6-6. The controller resulting from H_∞ design procedures applied to this model will command an injection wave based on the measured 0th, 1st and 2nd harmonic pressure perturbations.

Chapter 7

Closed Loop Experiments

The control laws, designed as described in Chapter 6, were implemented on the control computer and tested in the NASA Lewis compressor. The experimental results for radial and circumferential inlet distortion are presented in this chapter.

7.1 Closed Loop Results with Radial Inlet Distortion

Both constant gain control laws and the SISO H_∞ robust controller discussed in Section 6.2.1 have been tested with radial inlet distortion. The following two sections discuss the test results.

7.1.1 Constant Gain Control

Several stall ramps with different constant gain control schemes were conducted. However, as expected from previous results of constant gain experiments conducted in [32], none of the constant gain controllers reduced the stalling mass flow. The lack of improvement can be explained as follows. At the operating point (85% corrected rotor speed) the compressor dynamics are compressible. As shown in Figures 5-8 and 5-9, there are several lightly damped compressible modes. Suppose we apply a first harmonic constant gain controller and tune it so that it stabilizes the $[1, 0]$ mode. Then the other lightly damped modes (like mode $[1, 1]$ and $[1, 2]$) may be destabilized because the constant gain controller has a frequency independent phase shift. In situations like these constant gain is not effective and a frequency dependent control law must be used. For more detail see [33].

7.1.2 Robust H_∞ Control

The model-based SISO H_∞ controller (see Section 6.2.1) was tested next.

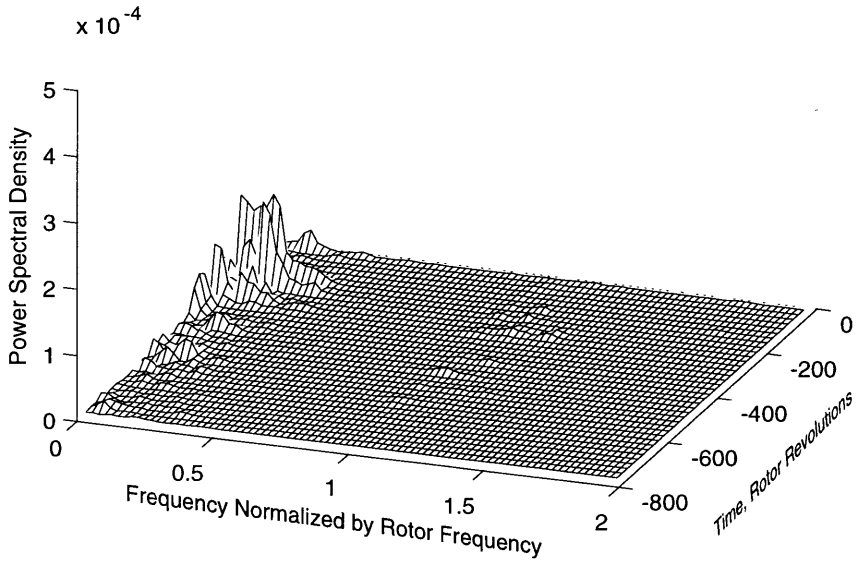

Figure 7-1: Spectrogram of the 0th harmonic during a stall ramp with radial inlet distortion and H_∞ control.

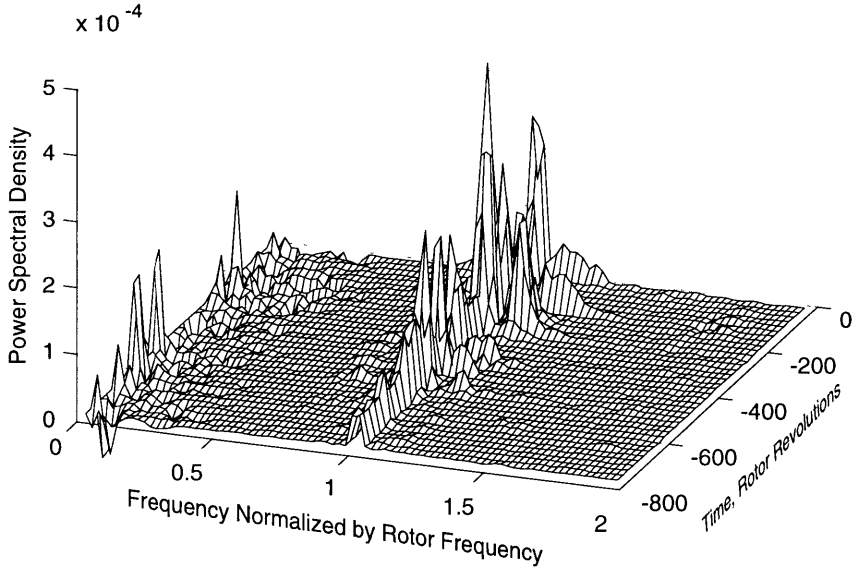

Figure 7-2: Spectrogram of the 1st harmonic during a stall ramp with radial inlet distortion and H_∞ control.

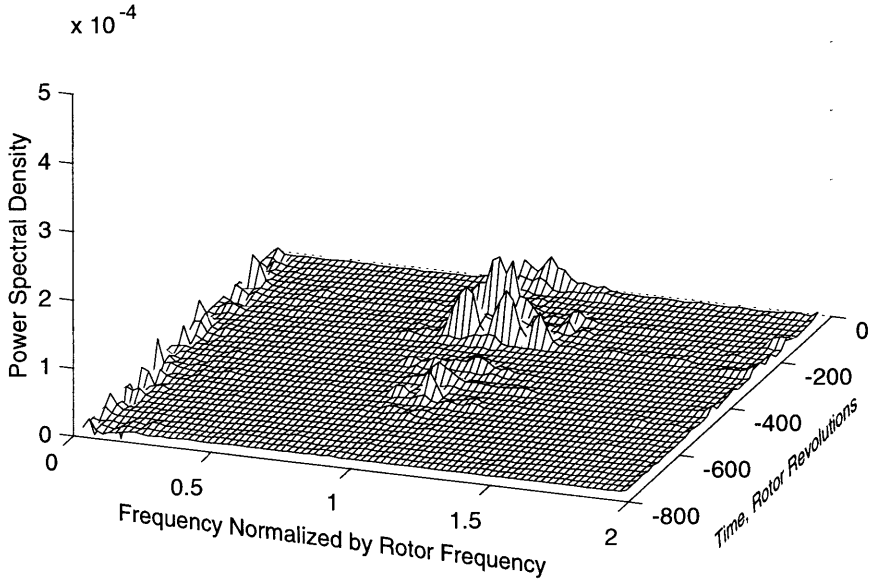

Figure 7-3: Spectrogram of the 2nd harmonic during a stall ramp with radial inlet distortion and H_∞ control.

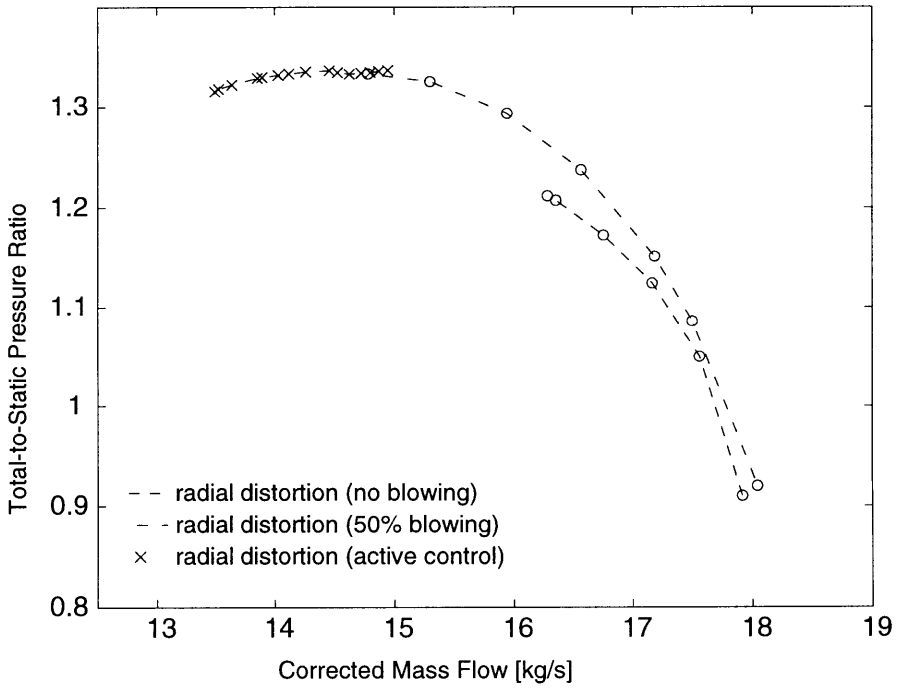

Figure 7-4: Speed lines with radial distortion. 50% steady blowing and first harmonic active control.

Figures 7-1, 7-2 and 7-3 show the spectrogram of the zeroth, first and second harmonic pressure perturbations for a stall ramp with this controller. Mode $[1,0]$, which was driving the compressor into stall without control (see Figure 5-6), is completely damped out (the magnitude of the power density spectrum in Figure 7-2 is small at frequencies near 0.4 times rotor frequency). It is now mode $[1,1]$ that is growing and going unstable at this lower mass flow. The spectrograms of the zeroth and second harmonic perturbations show little modal activity when the compressor stalled, indicating that the other modes were all well damped.

These results justify the choice of concentrating on a first harmonic controller. Additional zeroth and second harmonic controllers did not result in further reduction of the stalling mass flow. Adding a zeroth harmonic H_∞ controller has no effect since the $[1,1]$ mode determines the compressor stability (see Figure 7-2). The only way to operate beyond these mass flows is to increase the uncertainty circle around mode $[1,1]$ in the control law design. However, the eigenvalue perturbations shown in Figure 6-4 represent the case with the largest uncertainty that could be obtained within the H_∞ design constraints ([19]).

Active control results are summarized in Figure 7-4. With 50% steady blowing the stalling mass flow could be reduced by 9.7%. Applying the first harmonic robust SISO H_∞ controller allowed a further reduction in stalling mass flow of 7.5% relative to steady blowing, resulting in a total stalling mass flow reduction of 17.2%. Experiments by Weigl [32] at 100% corrected speed without inlet distortion achieved a reduction in stalling mass flow of 4.3% with 50% steady blowing alone, and about 7.8% using steady blowing plus zeroth, first and second harmonic active robust control.

7.2 Closed Loop Results with Circumferential Inlet Distortion

In this section active control of rotating stall with circumferential inlet distortion is discussed. Two different types of controllers were tested: constant gain control, and dynamic, model based robust H_∞ control.

7.2.1 Constant Gain Control

Weigl [32] showed that constant gain controllers are not effective in high-speed compressors with uniform inlet flow. A similar result was obtained with radial inlet distortion as discussed in Section 7.1.1. However, as will be shown momentarily, constant gain control was very effective on this machine in the presence of circumferential inlet distortion.

A first harmonic constant gain control law was found to be effective at stabilizing the circumferential inlet distortion case investigated here. When the gain and phase were set to $k_1 = 1$ and

$\beta_1 = \pi$ respectively, the stalling mass flow was reduced by 6.8% relative to steady blowing. The total-to-static speed lines are plotted in Figure 7-5 for undistorted inlet flow (solid), circumferential distortion without blowing (dash), and with 50% steady blowing (dash-dot). The stall point with the first harmonic constant gain control law is marked with a + in this figure.

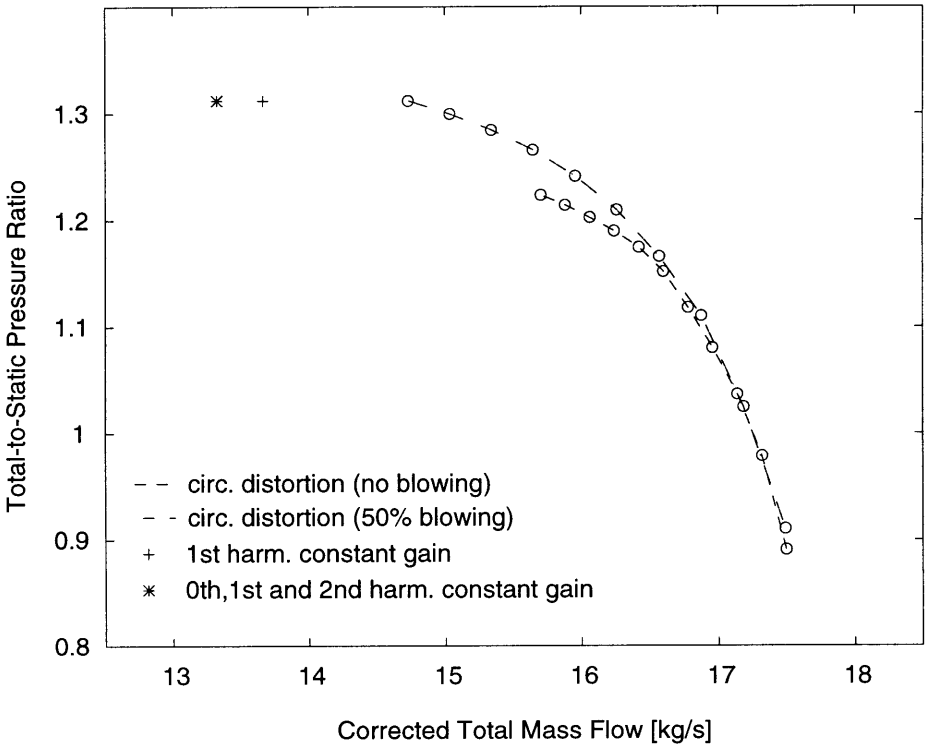

Figure 7-5: Speed lines for circumferential inlet distortion without blowing (dash), and with 50% steady blowing (dash-dot). Stall points with control are: 1st harmonic constant gain control (+), 0th-1st-2nd harmonic constant gain control (∗).

Spectrograms of the zeroth, first and second harmonics of the pressure perturbations, immediately prior to the control-on stall point, are shown in Figures 7-6, 7-7 and 7-8 respectively. The $[1,0]$ mode appears to be relatively well damped during the first 1000 revolutions in Figure 7-7, while the $[1,1]$ mode and the $[2,0]$ mode (Figure 7-8) are resonating strongly during the entire pre-stall period. Comparing Figure 7-7 to Figure 7-8 and inferring from the mode shape analysis, discussed in Section 5.4.1, that mode $[1,1]$ has only little second harmonic content (see Figure 5-15) indicates that the $[2,0]$ mode goes unstable first. Also note that modes $[0,0]$, $[1,0]$ and $[1,1]$ show zeroth harmonic content as depicted in Figure 7-6. In fact, adding a second harmonic constant gain feedback with $k_2 = 1$ and $\beta_2 = \pi$ damped out the second harmonic mode and achieved a further range extension of 2.2% in stalling mass flow relative to the first harmonic constant gain control case. The measured mass flow and pressure ratio is marked with a $*$ in Figure 7-5. A zeroth harmonic feedback, with gain $k_0 = 1$, is also in operation during this run.

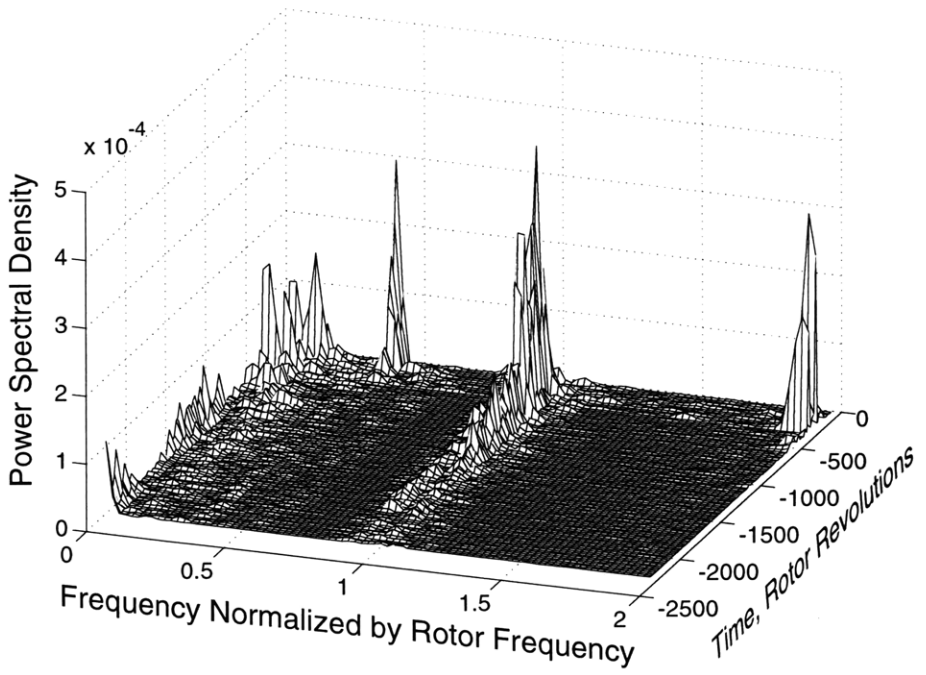

Figure 7-6: Spectrogram of the 0th harmonic pressure perturbations with circumferential inlet distortion and first harmonic constant gain control.

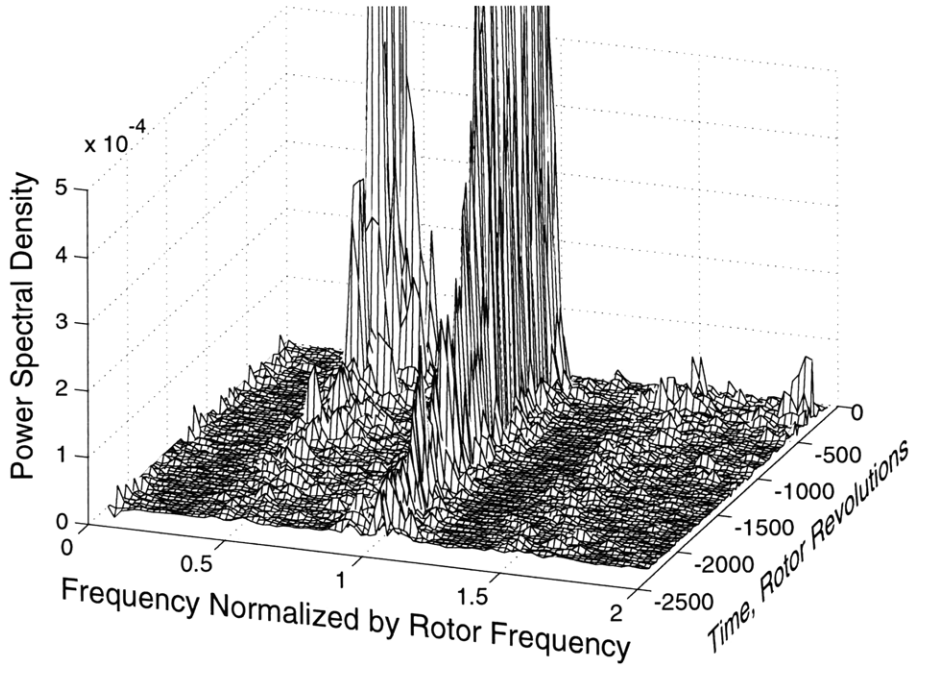

Figure 7-7: Spectrogram of the 1st harmonic pressure perturbations with circumferential inlet distortion and first harmonic constant gain control.

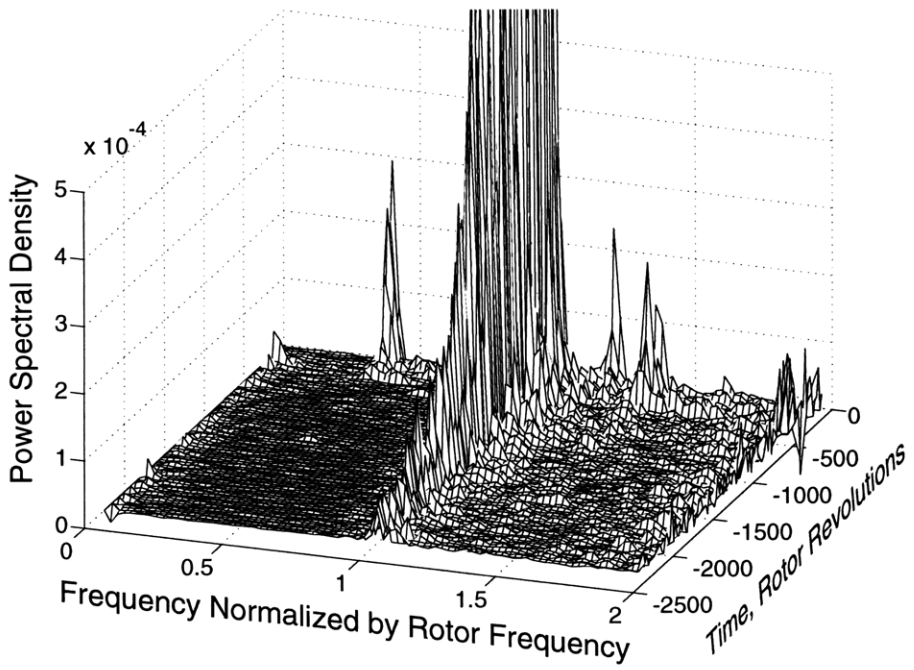

Figure 7-8: Spectrogram of the 2nd harmonic pressure perturbations with circumferential inlet distortion and first harmonic constant gain control.

These results clearly show that constant gain control is effective in the presence of circumferential inlet distortion. Since a compressible, distorted flow, control theoretic model does not exist, it is difficult to explain these phenomena. The system identification experiments indicate that a single mode with dominant first harmonic and incompressible features determines the stability, suggesting the applicability of a constant gain control strategy. This was also qualitatively and quantitatively verified using incompressible modeling methods ([30]). However, the measurements in Figure 5-13 show that there are *compressible* modes that have significant magnitudes in the coupled (off-diagonal) transfer functions (e.g. the $[1,1]$ mode has the same magnitude in $G_{11}(j\omega)$ as in $G_{10}(j\omega)$). Such coupling is typically detrimental to any control law which does not explicitly take it into account. Even without this coupling, the $[1,1]$ mode in this compressor has invariably been destabilized by constant gain control without circumferential distortion (see results by Weigl [33] and results with radial inlet distortion Section 7.1.1). Apparently the effect of circumferential inlet distortion in this machine is such that the constant gain control law, tuned for mode $[1,0]$ stabilization, does not destabilize the other lightly damped modes. It is not clear whether this fortuitous effect will exist in other compressors with circumferential inlet distortion.

7.2.2 Robust H_∞ Control

In this section the performance improvement obtained using robust H_∞ control is investigated. First the MIMO H_∞ controller based on the 0th and 1st harmonic model (Section 6.2.2) was tested in a closed loop stall experiment. As one can see from Figure 6-5, the controller design is conservative and this controller yielded a 2% reduction in stalling mass flow. The result is plotted in Figure 7-9, marked with a •. One explanation for this poor performance may be that the perturbation circles

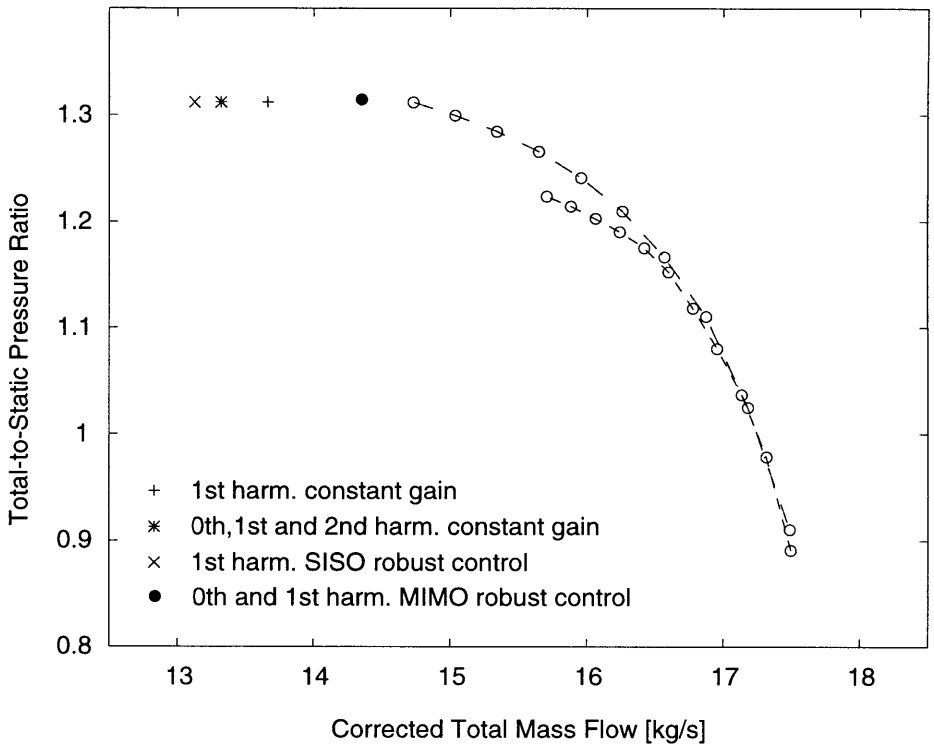

Figure 7-9: Speed lines for, circumferential inlet distortion without blowing (dash), and with 50% steady blowing (dash-dot). Stall points with control are. 1st harmonic constant gain control (+), 0th-1st-2nd harmonic constant gain control (∗), 1st harmonic SISO H_∞ control (×) and 0th-1st harmonic MIMO H_∞ control (•).

are small compared to the design with radial inlet distortion. The spectrograms of the zeroth, fist and second harmonic pressure perturbations show that mode $[0, 0]$, strongest in the zeroth harmonic (Figure 7-10), and mode $[1, 1]$, visible in the zeroth and first harmonic (see Figures 7-10 and 7-11), are damped up to 1000 rotor revolutions before stall (note that the stall point at 0 rotor revolutions is not the same as for the open loop spectrograms shown in Section 5.4). Then modes $[0, 0]$ and $[1, 0]$ seem to exceed the perturbation circles and start to resonate almost simultaneously. It is clear from these results that this MIMO controller needs further tuning. However time did not permit this approach to be pursued. Therefore an alternative method, described below, was investigated.

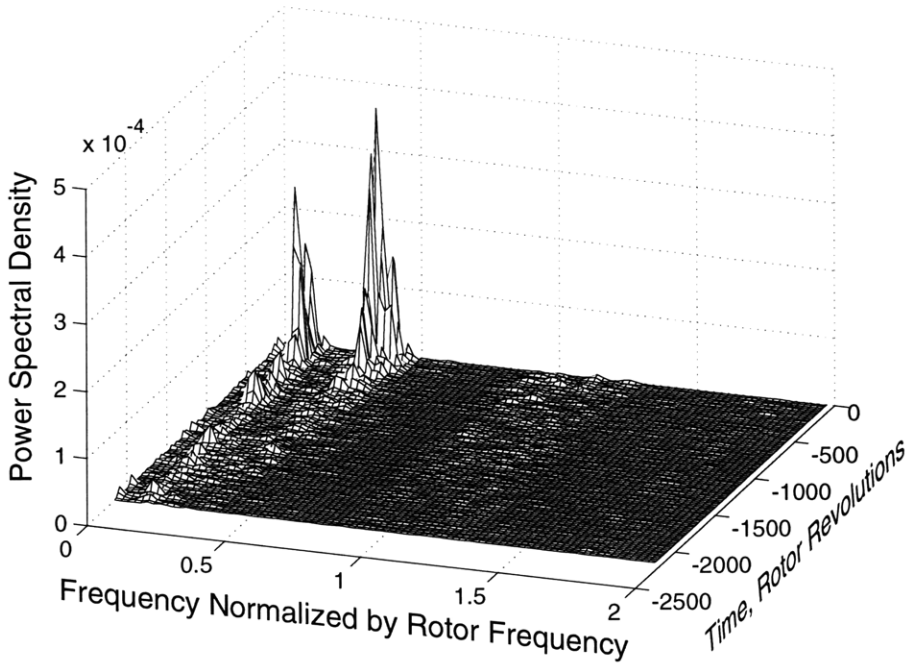

Figure 7-10: Spectrogram of the 0th harmonic pressure perturbations with circumferential inlet distortion and 0th-1st harmonic MIMO robust control.

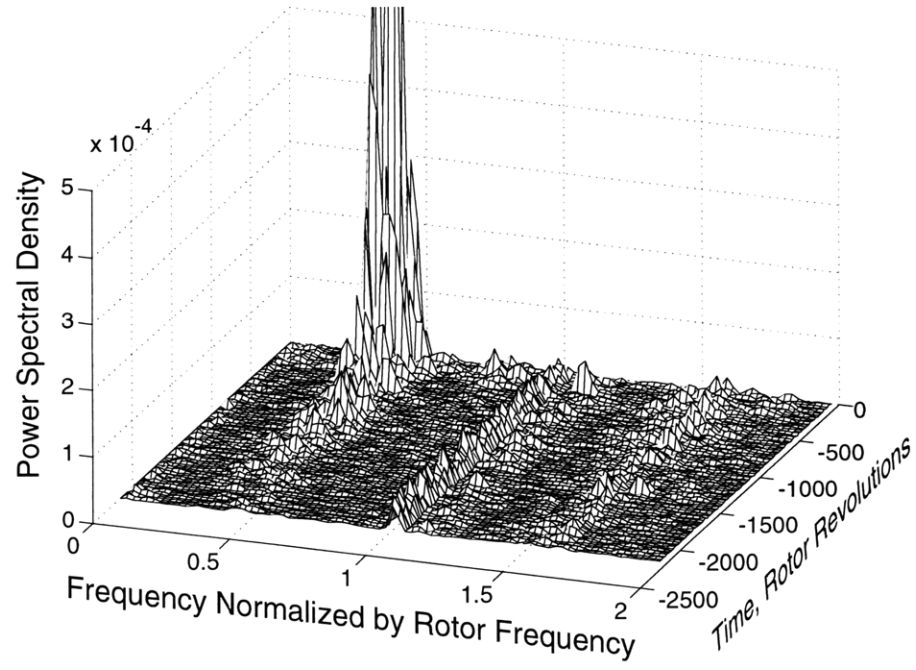

Figure 7-11: Spectrogram of the 1st harmonic pressure perturbations with circumferential inlet distortion and 0th-1st harmonic MIMO robust control.

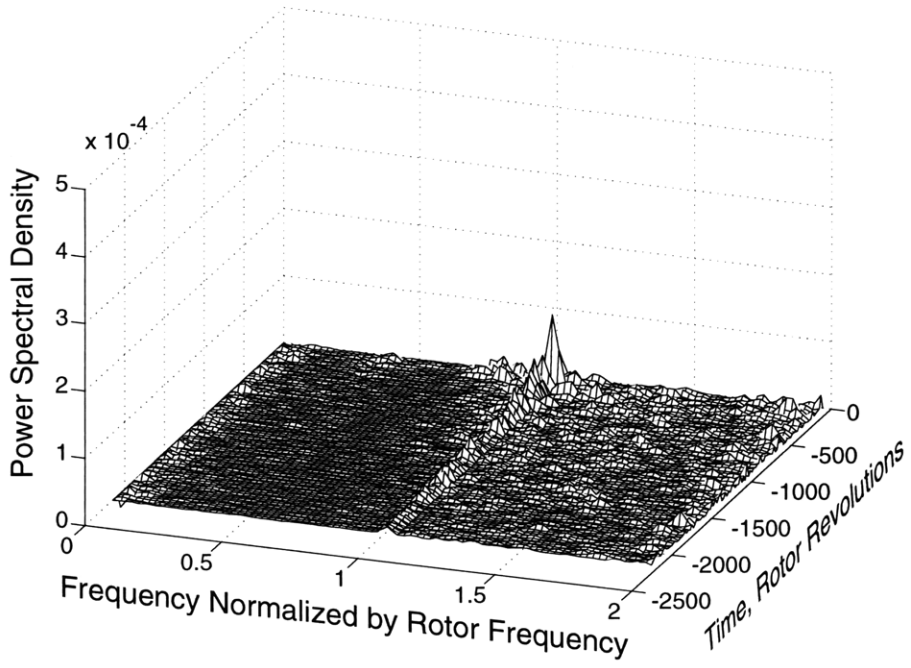

Figure 7-12: Spectrogram of the 2nd harmonic pressure perturbations with circumferential inlet distortion and 0th-1st harmonic MIMO robust control.

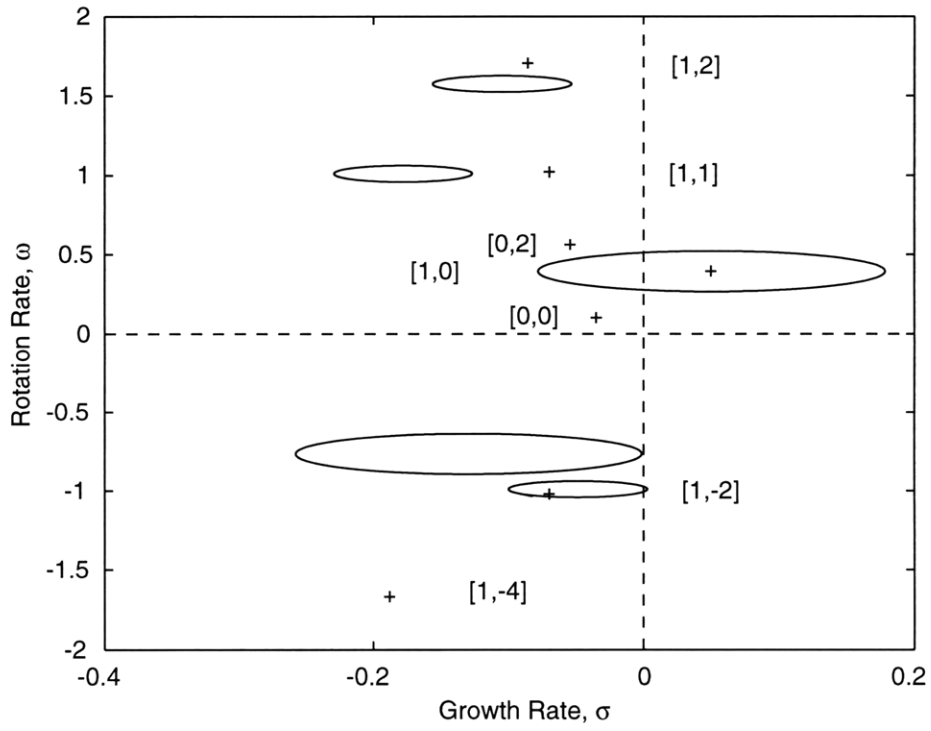

Figure 7-13: Identified coupled unstable dynamics with circumferential inlet distortion at $\dot{m}_{corr}^{tot} = 14.0$ kg/s and perturbation circles of H_∞ control law designed for radial inlet distortion.

The dominance of the first harmonic in the $[1,0]$ mode and the presence of a resonance in the $[1,1]$ mode in Figure 7-7 suggests that a robust controller which ignores coupling, and is designed for the first harmonic only, might yield improvement in performance. Fortunately, such a controller already existed at the time of these tests, because the frequencies associated with the $[1,0]$ mode for both circumferential and radial distortion are approximately the same (0.4 times rotor frequency). In fact, the eigenvalue location of the unstable $[1,0]$ mode used for design of the radial inlet distortion controller was almost identical to the identified eigenvalue location for this mode with circumferential inlet distortion. Figure 7-13 shows the identified eigenvalues with circumferential inlet distortion, together with circles indicating the range of eigenvalues which the first harmonic SISO H_∞ radial inlet distortion controller from Section 6.2.1 was designed to stabilize.

The $[1,0]$ mode perturbation circle includes the unstable pole associated with circumferential inlet distortion, indicating that the controller should be able to stabilize this mode. Although the $[1,1]$ mode with circumferential inlet distortion is more lightly damped than in the design model, the frequency is accurately captured by the design model. This proves to be sufficient for success of the controller, indicating that this pole remains stable for the mass flows of interest.

Based on these arguments the controller originally designed for radial distortion was tested experimentally and showed a large range extension. The stalling mass flow was reduced by 10.2% relative to steady blowing, resulting in a total reduction in stalling mass flow of 16.4%. This is indicated in Figure 7-9 with an $\times$. Of all the methods tested so far, this first harmonic SISO robust control law achieved the largest reduction in stalling mass flow, which is comparable to the reduction in stalling mass flow with radial inlet distortion shown in Figure 7-4. The MIMO controller based on the zeroth, first and second harmonic model, shown in Section 6.2.2 with features similar to the tested SISO controller but accounting for dynamic coupling, was then designed and was unfortunately never tested because of an internal object damage that destroyed the NASA Stage 35 blading.

7.3 Summary of Closed Loop Experimental Results

The closed loop results for both radial and circumferential inlet distortion are summarized in Table 7.1. The listed decrease in stalling mass flow (%) is relative to the distortion case without steady injection. The stall-margin is computed using Equation (3.1). In addition, the experimental results obtained by Weigl [33] for 100% speed and undistorted inlet flow are included in Table 7.1 for comparison[1].

[1]Again Equation (3.1) was used to compute the stall-margin with a working pressure ratio of 1.3 and a working mass flow of 20.6 kg/s, consistent with Figure 3-3.

Configuration	$\dot{m}_{\text{stall}}$ [kg/s]	% Decrease $\dot{m}_{\text{stall}}$	Stall-margin [%]
Radial Inlet Distortion (85% Speed)			
No Blowing	16.3	—	8.1
50% Blowing	14.7	9.7	24.1
1st harm. SISO robust control	13.48	17.2	30.0
Circumferential Inlet Distortion (85% Speed)			
No Blowing	15.7	—	10.9
50% Blowing	14.7	6.2	22.2
0th-1st harm. MIMO robust control	14.3	8.2	24.5
1st harm. constant gain control	13.6	13.0	27.8
0th-1st-2nd harm. const. gain control	13.3	15.2	29.6
1st harm. SISO robust control	13.1	16.4	30.6
Undistorted Inlet Flow 100% Speed (from [33])			
No Blowing	18.7	—	18.8
50% Blowing	17.9	4.3	27.0
0th-1st-2nd harm. SISO robust control	17.3	7.8	30.1

Table 7.1: Active control experimental results with inlet distortion.

Chapter 8

Conclusions and Summary

The experiments discussed in this research represent the first attempt at active rotating stall control in a transonic single-stage compressor with inlet distortion using an annular array of jet-injectors. Two different types of inlet distortion, a radial distortion and a more realistic circumferential distortion, have been investigated. Active control was conducted with both distortion types. The results and conclusions are summarized below.

8.1 Radial Inlet Distortion

Measurements of the radial inlet distortion profile showed that the flow is still circumferentially uniform but skewed towards the hub, resulting in a total pressure drop and thus in higher incidence and loading of the blades in the tip region. The peak pressure rise drops and the compressor stalls at higher mass flows. Steady state injection results in a range extension of 9.7% in stalling mass flow relative to the case with radial inlet distortion and no injection.

Measured compressor transfer functions revealed that the compressible stall dynamics with radial inlet distortion are still decoupled. The pre-stall dynamics were dominated by a Moore-Greitzer like mode in the first harmonic. This allowed the design of SISO control laws to stabilize the compressor. A first harmonic H_∞ robust controller achieved a reduction in stalling mass flow of 7.5% relative to steady blowing yielding a total reduction of 17.2%. This result reflects an improvement in stalling mass flow reduction compared to experiments with no inlet distortion ([32]).

The stall inception pattern with radial inlet distortion showed spikes or waves depending on whether the actuators were turned off or operated at steady blowing, altering the total pressure in the tip region. The experiments indicate that the simple model developed by Camp and Day [7] also holds in a single-stage transonic compressor.

8.2 Circumferential Inlet Distortion

The experiments presented here are the first time that coupled compressible stall dynamics were investigated and that a transonic compressor with circumferential inlet distortion was actively stabilized. The distortion magnitude was about one dynamic head, corresponding to DC(60)=0.61.

Forced response experiments revealed strong coupling between the harmonics of the pressure perturbations. Analysis showed that a single mode of the compression system determines its stability — this behavior is similar to that of low-speed compressors. Constant gain control achieved a large range extension. The dominance of an incompressible mode, together with fortuitous coupling between the harmonics, appears to change the stall dynamics in such a way that (unlike the undistorted flow case) constant gain feedback does not destabilize lightly damped compressible modes. Thus, although the details of the measured dynamics are strongly affected by compressibility, the control strategy applied here was the same as that used in low-speed, undistorted compressors. The maximum reduction in stalling mass flow with zeroth, first and second harmonic constant gain controllers was 9.0% relative to steady blowing, giving a total reduction in stalling mass flow of 15.2%.

In general, a MIMO control law is indicated when coupled multi-variable dynamics are present. In this experiment, however, the dominance of the first harmonic in the destabilizing mode suggested that a SISO H_∞ controller for the first harmonic might work well. This in fact proved to be the case: a controller originally designed for radial distortion achieved a total reduction in stalling mass flow of 16.4%, thus demonstrating robustness with respect to a change in inlet flow from radial to circumferential distortion. The performance of a MIMO H_∞ controller based on the zeroth and first harmonic model was also investigated and the results showed only little reduction in stalling mass flow (2% relative to the steady blowing case with distortion). Time did not permit further tuning of this controller and testing of another MIMO robust controller that was based on a zeroth, first and second harmonic model.

8.3 Future Work

These results show that active control of rotating stall in a high-speed compressor results in a significant increase in the stable operating range in the presence of inlet distortion. These results are very promising for future work and applications. Much work remains to be done, however. In particular, the dependence of the dynamics on nonlinear coupling between the compressor and a (typically unknown) inlet distortion add a degree of uncertainty which is addressed in our approach only to the extent that our control law is robust to modeling errors. More explicitly designing for, and subsequently testing against, unknown distortion scenarios is needed. It is also necessary to investigate and better understand the interplay between distortion and lightly damped compressible

dynamics. This interplay was beneficial in these experiments, but may not always be so. Finally, one would like to use as few actuators and as little mass flow as possible to achieve results like those presented here, and do so in a multistage high-speed compressor.

Appendix A

Mass Flow Correction with Inlet Distortion

Inlet distortion has a strong effect on the local flow field. The standard day mass flow correction must therefore account for the variation in local mass flow, total temperature and total pressure. The standard day corrected mass flow for a single stream is defined as

$$\dot{m}_{corr} = \frac{\sqrt{T_t/T_o}}{p_t/p_o} \cdot \dot{m} \ , \tag{A.1}$$

where T_o is the standard day temperature, T_t is the reference total temperature, p_o is the standard day pressure, p_t is the reference total pressure and $\dot{m}$ is the physical mass flow. With inlet distortion (both radial and circumferential) the flow through the compressor can be approximated by two major streams: an unspoiled stream and a spoiled stream. Using the estimated spoiled area to total area ratio ζ_{sp} (approximately the distortion screen area to total annulus area ratio) the mass flows for the spoiled and unspoiled streams can be written respectively as

$$\dot{m}_{sp} = \rho_{sp} \cdot v_{sp} \cdot \zeta_{sp} \cdot A \tag{A.2}$$

and

$$\dot{m}_{usp} = \rho_{usp} \cdot v_{usp} \cdot (1 - \zeta_{sp}) \cdot A \ , \tag{A.3}$$

where the product of density and axial velocity can be computed from the pressure and temperature measurements at station B (Figure 2-2) for the two streams as follows:

$$\rho_{sp} \cdot v_{sp} = \frac{p_{sp}}{R\, T_{sp}} \cdot \sqrt{\frac{2\,\gamma}{\gamma - 1}(T_t^{sp} - T_{sp})} \tag{A.4}$$

and

$$\rho_{usp} \cdot v_{usp} = \frac{p_{usp}}{R\,T_{usp}} \cdot \sqrt{\frac{2\,\gamma}{\gamma - 1}(T_t^{usp} - T_{usp})}\,. \tag{A.5}$$

The effective total annulus flow area A can be derived using the measured far upstream orifice mass flow $\dot{m}_{orf}$ and continuity

$$A = \frac{\dot{m}_{orf}}{\zeta_{sp} \cdot \rho_{sp} \cdot v_{sp} + (1 - \zeta_{sp}) \cdot \rho_{usp} \cdot v_{usp}}\,. \tag{A.6}$$

Combining Equations (A.2) and (A.3) with Equations (A.4) and (A.5) and Equation (A.6) yields for the spoiled and unspoiled sector mass flows

$$\dot{m}_{sp} = \frac{\zeta_{sp} \cdot \dot{m}_{orf} \cdot \frac{p_{sp}}{T_{sp}} \cdot \sqrt{T_t^{sp} - T_{sp}}}{\zeta_{sp} \cdot \frac{p_{sp}}{T_{sp}} \cdot \sqrt{T_t^{sp} - T_{sp}} \;+\; (1 - \zeta_{sp}) \cdot \frac{p_{usp}}{T_{usp}} \cdot \sqrt{T_t^{usp} - T_{usp}}}\,, \tag{A.7}$$

and

$$\dot{m}_{usp} = \frac{(1 - \zeta_{sp}) \cdot \dot{m}_{orf} \cdot \frac{p_{usp}}{T_{usp}} \cdot \sqrt{T_t^{usp} - T_{usp}}}{\zeta_{sp} \cdot \frac{p_{sp}}{T_{sp}} \cdot \sqrt{T_t^{sp} - T_{sp}} \;+\; (1 - \zeta_{sp}) \cdot \frac{p_{usp}}{T_{usp}} \cdot \sqrt{T_t^{usp} - T_{usp}}}\,. \tag{A.8}$$

The injector mass flow is measured by a separate venturi meter. Using Equation (A.1) for the injected mass flow $\dot{m}_{inj}$ and the two streams, the total standard day corrected mass flow through the compressor can be written as

$$\dot{m}_{corr}^{tot} = \frac{\sqrt{T_t^{inj}/T_o^{inj}}}{p_t^{inj}/p_o^{inj}} \cdot \dot{m}_{inj} + \frac{\sqrt{T_t^{sp}/T_o}}{p_t^{sp}/p_o} \cdot \dot{m}_{sp} + \frac{\sqrt{T_t^{usp}/T_o}}{p_t^{usp}/p_o} \cdot \dot{m}_{usp}\,. \tag{A.9}$$

The reference total temperature and total pressure for the injected mass flow are measured in the injector.

This standard day correction procedure is used to compute the total corrected mass flow through the compressor for both radial and circumferential inlet distortion. In the case of radial inlet distortion a radial survey at station B Figure 2-2 was conducted to obtain the temperature and pressure values in the spoiled (near tip) and unspoiled (near hub) streams.

Appendix B

Transfer Function Transformation

Assume a SISO transfer function $G(j\omega)$ going from a *complex* input $\widetilde{u}(j\omega)$ to a *complex* output $\widetilde{y}(j\omega)$. Remember that transfer functions with complex inputs and outputs are *not* symmetric about $\omega = 0$. Now the input and output signals can be split into their real and imaginary part respectively denoted by subscripts $_R$ and $_I$ and $G(j\omega)$ can be split into two transfer functions $G^r(j\omega)$ and $G^i(j\omega)$

$$\widetilde{y}_R(j\omega) + j \cdot \widetilde{y}_I(j\omega) = \left[G^r(j\omega) + j \cdot G^i(j\omega)\right] \left[\widetilde{u}_R(j\omega) + j \cdot \widetilde{u}_I(j\omega)\right] . \tag{B.1}$$

Note that $G^r(j\omega)$ and $G^i(j\omega)$ are still complex but relate a *real* input to a *real* output. Collecting terms on the right hand side yields

$$= \left\{G^r(j\omega)\widetilde{u}_R(j\omega) - G^i(j\omega)\widetilde{u}_I(j\omega)\right\} \; + \; j \cdot \left\{G^i(j\omega)\widetilde{u}_R(j\omega) + G^r(j\omega)\widetilde{u}_I(j\omega)\right\} \tag{B.2}$$

and the transfer functions can be written in matrix form as

$$\begin{bmatrix} \widetilde{y}_R(j\omega) \\ \widetilde{y}_I(j\omega) \end{bmatrix} = \begin{bmatrix} G^r(j\omega) & -G^i(j\omega) \\ G^i(j\omega) & G^r(j\omega) \end{bmatrix} \begin{bmatrix} \widetilde{u}_R(j\omega) \\ \widetilde{u}_I(j\omega) \end{bmatrix} . \tag{B.3}$$

The obtained result represents a 2 by 2 MIMO system with real input and output vectors. However $G^r(j\omega)$ and $G^i(j\omega)$ are *not* the real and imaginary parts of $G(j\omega)$ and have to be derived from $G(j\omega)$. To do this we take advantage of the fact that a transfer function $H(j\omega)$ with real inputs and outputs is symmetric about $\omega = 0$ yielding $|H(j\omega)| = |H(-j\omega)|$ and furthermore

$$H(-j\omega) = H^*(j\omega) \tag{B.4}$$

where the superscript * stands for the complex conjugate. Applying this feature to $G^r(j\omega)$ and

$G^i(j\omega)$ we can write

$$G(j\omega) = G^r(j\omega) + j \cdot G^i(j\omega) \tag{B.5}$$

$$G(-j\omega) = G^{r*}(j\omega) + j \cdot G^{i*}(j\omega) \; . \tag{B.6}$$

The next step is to construct the real and imaginary parts of $G^r(j\omega)$ and $G^i(j\omega)$ out of $G(j\omega)$ and $G(-j\omega)$. To do so the following trick is used: to eliminate the imaginary parts of $G^r(j\omega)$ and $G^i(j\omega)$ we add $G(j\omega)$ and $G(-j\omega)$ using Equations (B.5) and (B.6) yielding

$$G(j\omega) + G(-j\omega) = 2\,\mathrm{Re}\left\{G^r(j\omega)\right\} + j \cdot 2\,\mathrm{Re}\left\{G^i(j\omega)\right\} \; . \tag{B.7}$$

Comparing real and imaginary parts of the LHS to the ones on the RHS we obtain the real parts of $G^r(j\omega)$ and $G^i(j\omega)$:

$$\mathrm{Re}\left\{G^r(j\omega)\right\} = \frac{1}{2}\,\mathrm{Re}\left\{G(j\omega) + G(-j\omega)\right\} \tag{B.8}$$

$$\mathrm{Re}\left\{G^i(j\omega)\right\} = \frac{1}{2}\,\mathrm{Im}\left\{G(j\omega) + G(-j\omega)\right\} \tag{B.9}$$

The same thing can be done to obtain the imaginary parts by subtracting $G(j\omega)$ and $G(-j\omega)$ from each-other yielding

$$G(j\omega) - G(-j\omega) = j \cdot 2\,\mathrm{Im}\left\{G^r(j\omega)\right\} - 2\,\mathrm{Im}\left\{G^i(j\omega)\right\} \; . \tag{B.10}$$

The imaginary parts of $G^r(j\omega)$ and $G^i(j\omega)$ can be gained by comparing again the real and imaginary parts of the LHS to the ones on the RHS giving

$$\mathrm{Im}\left\{G^r(j\omega)\right\} = \frac{1}{2}\,\mathrm{Im}\left\{G(j\omega) - G(-j\omega)\right\} \tag{B.11}$$

$$\mathrm{Im}\left\{G^i(j\omega)\right\} = -\frac{1}{2}\,\mathrm{Re}\left\{G(j\omega) - G(-j\omega)\right\} \; . \tag{B.12}$$

The components $G_r(j\omega)$ and $G_i(j\omega)$ of the MIMO transfer function matrix Equation (B.3) with real input and output vectors are therefore given by the following transformation formulae:

$$G^r(j\omega) = \frac{1}{2}\,\mathrm{Re}\left\{G(j\omega) + G(-j\omega)\right\} + j \cdot \frac{1}{2}\,\mathrm{Im}\left\{G(j\omega) - G(-j\omega)\right\} \tag{B.13}$$

$$G^i j\omega) = \frac{1}{2} \operatorname{Im} \{G(j\omega) + G(-j\omega)\} - j \cdot \frac{1}{2} \operatorname{Re} \{G(j\omega) - G(-j\omega)\} \tag{B.14}$$

These transformation formulae are used to transform the measured transfer functions (ETFE's). The MIMO system with real input and output vectors is the input format for the system identification algorithm (FORSE).

Bibliography

[1] BERNDT, R., WEIGL, H., PADUANO, J., AND EPSTEIN, A. "Experimental Techniques for Actuation, Sensing, and Measurement of Rotating Stall Dynamics in High Speed Engines". In *Sensing, Actuation, and Control in Aeropropulsion* (Apr. 1995), J. D. Paduano, Ed., vol. 2492, SPIE.

[2] BERNDT, R. G. "Actuation for Rotating Stall Control of High Speed Compressors". Master's thesis, Department of Aeronautics and Astronautics, MIT, 1995.

[3] BERNSTEIN, HEISER, AND HEVENOR. "Compound Compressible Flow". *Journal of Applied Mechanics* (Sept. 1967), pp. 548–554.

[4] BONNAURE, L. "Modelling High Speed Multistage Compressor Stability". Master's thesis, Department of Aeronautics and Astronautics, MIT, 1991.

[5] BRIGHT, M., QAMMAR, H., AND WANG, L. "Investigation of Pre-Stall Mode and Pip Inception in High Speed Compressors Through the Use of Correlation Integral". In *ASME Gas Turbine and Aeroengine Congress and Exposition, Stockholm, Sweden, Paper 98-GT-365* (June 1998).

[6] BRIGHT, M., QAMMAR, H., WEIGL, H., AND PADUANO, J. "Stall Precursor Identification in High-Speed Compressor Stages Using Chaotic Time Series Analysis Methods". *ASME J. of Turbomachinary, Vol. 119* (July 1997), pp. 491–500.

[7] CAMP, T., AND DAY, I. "A Study of Spike and Modal Stall Phenomena in a Low-Speed Axial Compressor". In *ASME Gas Turbine and Aeroengine Congress and Exposition, Orlando, FL, Paper 97-GT-526* (June 1997).

[8] CUMPSTY, N. *Compressor Aerodynamics.* Addison-Wesley Publishing Company, 1989.

[9] DAY, I., AND FREEMAN, C. "The Unstable Behavior of Low and High-Speed Compressors". *ASME J. of Turbomachinary, Vol. 116* (Apr. 1993), pp. 194–201.

[10] EPSTEIN, A., WILLIAMS, J., AND GREITZER, E. "Active Suppression of Aerodynamics Instabilities in Turbomachines". *J. of Propulsion, Vol. 5*, No. 2 (March-April 1989), pp. 204–211.

[11] FEULNER, M., HENDRICKS, G., AND PADUANO, J. "Modeling for Control of Rotating Stall in High Speed Multi-Stage Axial Compressors". In *ASME Gas Turbine and Aeroengine Congress and Exposition, The Hague, The Netherlands, Paper 94-GT-292* (June 1994).

[12] GONG, Y. *A Computational Model for Rotating Stall and Inlet Distortions in Multistage Compressors.* PhD thesis, Department of Aeronautics and Astronautics, MIT, 1999.

[13] GREITZER, E., Aug. 1997. Personal communications.

[14] HAYNES, J., HENDRICKS, G., AND EPSTEIN, A. "Active Stabilization of Rotating Stall in a Three-Stage Axial Compressor". *ASME J. of Turbomachinary, Vol. 116* (1994), pp. 226–239.

[15] HENDRICKS, G., BONNAURE, L., LONGLEY, J., GREITZER, E., AND EPSTEIN, A. "Analysis of Rotating Stall Onset in High Speed Axial Flow Compressors". In *AIAA/SAE/ASME/ASEE 29th Joint Propulsion Conference, Paper AIAA-93-2233* (July 1993).

[16] HYNES, T., AND GREITZER, E. "A method for assessing Effects of Circumferential Flow Distortion on Compressor Stability". *ASME J. of Turbomachinary, Vol. 109* (July 1987), pp. 371–379.

[17] JACQUES, R. *On-line System Identification and Control Design for Flexible Structures.* PhD thesis, Department of Aeronautics and Astronautics, MIT, 1994.

[18] KOCH, C.-C. "Experimental Evaluation of Outer Case Blowing or Bleeding of a Single-Stage Axial Flow Compressor". Tech. Rep. CR-54592, NASA, 1970.

[19] KWAKERNAAK, H. "Robust Control and H_∞-Optimization: Tutorial Paper". *Automatica, Vol. 29, No. 3* (1993), pp. 255–273.

[20] LJUNG, L. *System Identification: Theory for the User.* Prentice-Hall, Inc., 1987.

[21] LONGLEY, J. "A Review of Nonsteady Flow Models for Compressor Stability". *ASME J. of Turbomachinary* (Apr. 1994), pp. 202–215.

[22] LONGLEY, J., AND GREITZER, E. "Inlet Distortion Effects in Aircraft Propulsion System Integration". *Steady and Transient Performance Prediction of Gas Turbine Engines, AGARD-LS-183* (May 1992), pp. 6-1 – 6-18.

[23] MOORE, F. "A Theory of Rotating Stall of Multistage Axial Compressors: Part I — Small Disturbances". *ASME J. of Engineering for Gas Turbines and Power, Vol. 106* (Apr. 1984), pp. 313–320.

[24] MOORE, F., AND GREITZER, E. "A Theory of Post-Stall Transients in Axial Compressors: Part I — Development of the Equations". *ASME J. of Engineering for Gas Turbines and Power, Vol. 108* (1986), pp. 68–76.

[25] PADUANO, J. *Active Control of Rotating Stall in Axial Compressors.* PhD thesis, Department of Aeronautics and Astronautics, MIT, Feb. 1992.

[26] PADUANO, J., EPSTEIN, A., VALAVANI, L., LONGLEY, J., GREITZER, E., AND GUENETTE, G. "Active Control of Rotating Stall in a Low-Speed Axial Compressor". *ASME J. of Turbomachinary, Vol. 115* (Jan. 1993), pp. 48–56.

[27] REID, L., AND MOORE, D. "Design and Overall Performance of Four Highly Loaded, High Speed Inlet Stages for and Advanced High Pressure Ratio Core Compressor". Tech. Rep. TP-1337, NASA, 1978.

[28] REID, L., AND MOORE, D. "Performance of Single-Stage Axial-Flow Transonic Compressor With Rotor and Stator Aspect Ratios of 1.19 and 1.26, Respectively, and With Design Pressure Ratio 1.82". Tech. Rep. TP-1338, NASA, 1978.

[29] SMITH, R. "Technical Notes and Correspondence: Eigenvalue Perturbation Models for Robust Control". *IEEE Transactions on Automatic Control, Vol. 40*, No. 6 (June 1995), pp. 1063–1066.

[30] VAN SCHALKWYK, C. *Active Control of Rotating Stall with Inlet Distortion.* PhD thesis, Department of Aeronautics and Astronautics, MIT, June 1996. Also available as Gas Turbine Lab Report #222.

[31] VAN SCHALKWYK, C., PADUANO, J., GREITZER, E., AND EPSTEIN, A. "Active Stabilization of Axial Compressors with Circumferential Inlet Distortion". In *ASME Gas Turbine and Aeroengine Congress and Exposition, Orlando, FL, Paper 97-GT-279* (June 1997).

[32] WEIGL, H., PADUANO, J., FRÉCHETTE, L., EPSTEIN, A., AND GREITZER, E. "Active Stabilization of Rotating Stall and Surge in a Transonic Single Stage Axial Compressor". In *ASME Gas Turbine and Aeroengine Congress and Exposition, Orlando, FL, Paper 97-GT-411* (June 1997).

[33] WEIGL, H. J. *Active Stabilization of Rotating Stall and Surge in a Transonic Single Stage Axial Compressor.* PhD thesis, Department of Aeronautics and Astronautics, MIT, May 1997.

[34] WILLIAMS, D. "Engine Compatibility". Tech. rep., Rolls-Royce PLC, May 1991.